The Effects of High Pressure on the Vibrational and Magnetic Properties of Iron-Based Materials

Thesis by

Alexander B. Papandrew

In Partial Fulfillment of the Requirements

for the Degree of

Doctor of Philosophy

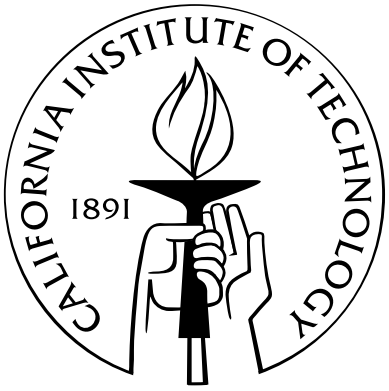

California Institute of Technology

Pasadena, California

2006

(Defended January 23, 2006)

Satius est supervacua scire quam nihil.

–Lucius Annaeus Seneca, *Epistulae Morales*

Acknowledgements

This document would never have been completed without the aid and guidance of my advisor, Brent Fultz. I learned invaluable lessons about the pursuit of science from Brent, and I hope to bear them out in the pages that follow.

A large fraction of the experimental data in this document was acquired at U.S. government facilities external to Caltech. It is impossible to list everyone who lent a hand or had a kind word at three in the morning, but a few people deserve special thanks. Wolfgang Sturhahn, Tom Toellner, Michael Hu, Paul Chow, and H. Peter Liermann of the Advanced Photon Source and Zema Chowdhuri of the NIST Center for Neutron Research helped to make my travels enjoyable and productive. The staff of the Carnegie Institute, notably Dave Mao, Rus Hemley, and Ron Cohen, were also instrumental in making this research possible.

I cannot offer enough praise to the colleagues with whom I shared many long nights of data acquisition. Alan Yue and Itzhak Halevy frequently astonished me with their skill and their tolerance for sleep deprivation. It was a great pleasure to have worked with them.

At Caltech, I was fortunate to share an office with Jason Graetz, who inspired me to find the confidence needed to reach the end of this long road. The other members of the Fultz group have similarly favored me with their support. In particular, I would like to acknowledge Channing Ahn, Jiao Lin, Olivier Delaire, Tabitha Swan-Wood, Ryan Monson, Max Kresch, Mike McKerns, Rebecca Stevens, and Matt Lucas for many helpful discussions.

Despite the vicissitudes of life in graduate school, I was lucky enough to retain the

constant support of several true friends. Nathan Lundblad, Ian Swanson, and Jason "Cup" Keith bettered me with their friendship. I would also like to recognize the past and present members of the Caltech Rugby Football Club for their dual commitments to victory and rambunctious endeavor, while faced with significant odds against both. I reserve my most profound thanks for Mary Devlin, who lent me her strength when mine was sorely lacking.

Finally, nothing I have accomplished would have been possible without the unconditional love and support of my parents, Deborah and Andrew, and my brother, Nick. Thank you.

Financial support for the the work in this thesis was provided by the California Institute of Technology, the Army Research Office, the Carnegie-DOE Alliance Center, and the National Science Foundation.

Abstract

Experimental methods are demonstrated for studying pressure-dependent material properties and solid phases unattainable at ambient pressure with high-pressure synchrotron nuclear resonance techniques.

Pressure presents an intriguing experimental parameter for investigating the problem of excess low-energy (<12 meV) vibrational modes in nanocrystalline materials. A satisfactory explanation for the origin of these modes has yet to be put forth, and until now, the volume dependence of the interatomic forces responsible for these modes had never been measured. The phonon density of states (DOS) of nanocrystalline ^{57}Fe was measured under pressures up to 28 gigapascals (2.8×10^5 atm) using the nuclear resonant inelastic x-ray scattering (NRIXS) technique. The nanocrystalline material exhibited an enhancement in its DOS at low energies by a factor of 2.2. This enhancement persisted throughout the entire pressure range, and was unaffected by the pressure-induced phase transformation (from bcc to hcp) at 13 GPa. At higher energies, the van Hove singularities observed in the samples were coincident in energy and remained so at all pressures, indicating that the forces conjugate to the normal coordinates of the nanocrystalline materials are similar to the interatomic potentials of bulk crystals. Subsequent neutron inelastic scattering measurments at ultra-low energies (2–18 μeV) also observed enhancement in the vibrational spectrum of the nanocrystalline material. A portion of this enhancement is attributed to novel microstructural modes, characterized by the cooperative dynamics of individual crystallites.

The high pressure, hcp (ϵ) phase of iron and its alloys is thought to comprise

much of the earth's core. The debate regarding the magnetic ground state of ϵ-Fe has continued for nearly half a century, and has recently been renewed by the discovery of superconductivity in the phase below 2 K. Though repeated Mössbauer effect measurements have failed to detect magnetic hyperfine fields in ϵ-Fe, recent density functional theory (DFT) investigations have reconciled the null experimental results by proposing a static antiferromagnetic structure with negligible hyperfine fields. The crux of this argument is the perfect cancellation of core electron polarization at the nucleus by an equally large and oppositely oriented conduction electron polarization. To test this hypothesis, an alloy of composition $Fe_{92}Ni_8$ was subjected to synchrotron Mössbauer spectrometry (SMS) at 20 GPa and 11 K. The addition of nickel was expected to disrupt the precise balance of core and conduction electron polarization in the alloy, and to result in a measurable hyperfine field in the presence of significant magnetic moments. Using full-potential DFT calculations with the generalized gradient approximation (GGA), this effect was verified for a Fe_7Ni_1 hcp supercell, which exhibited calculated hyperfine fields of nearly 70 kG. However, SMS measurements were unable to detect a hyperfine field. This disparity may be attributed to quantum spin fluctuations on the geometrically frustrated hcp lattice with periods much shorter than the lifetime of the nuclear excited state. Alternately, the result is evidence of a significant flaw in the handling of exchange coupling by the GGA exchange-correlation functional.

Contents

List of Figures

List of Tables

Chapter 1

Introduction

Pressure is often ignored in simplified treatments of condensed matter physics. This can be well reasoned, as pressures sufficient to abrogate this approach naturally occur only in environments such as Earth's interior and within distant celestial bodies. Nevertheless, the rich set of phenomena in the realm of high pressures provide copious modes of inquiry into the nature of solids. A list of the orders of magnitude of natural and man-made pressures is shown in Table 1.1.

In classical thermodynamics, pressure couples the volume of a system to its free energy. The relative stability of a phase is a predictive goal of materials science and is determined by the minima of the free energy surface. Moreover, pressure is a powerful tool for probing material properties that depend strongly on volume. The frequency

Table 1.1: Orders of magnitude of natural and man-made pressures

Pressure [bar]	
10^{-32}	Interstellar space
10^{-16}	Best laboratory vacuum
10^{-8}	Atmosphere 300 miles above Earth's surface
10^{-2}	Water vapor at triple point
10^{0}	Atmosphere at sea level
10^{3}	Bottom of Marianas trench
10^{6}	Center of Earth
10^{9}	Center of Sun
10^{32}	Center of neutron star

of lattice vibrations and the presence of magnetism are two such properties that are considered in this thesis.

The generation of high static pressures is approaching maturity as a scientific technique. The field was pioneered by Bridgman,* who used large hydraulic presses to generate pressures approaching 10 GPa. Today, an apparatus capable of reaching 500 GPa can fit in the palm of one's hand. Chapter 2 introduces the class of device that has enabled these advances: the diamond anvil cell (DAC).

Significant contributions have been made to condensed matter physics in recent years with DAC technology. Highlights include the discovery of superconductivity in both metallic iron and lithium [1], the finding that elemental osmium is less compressible than diamond [2], and the measurement of the complete vibrational spectrum of iron to pressures above 150 GPa [3]. It is also believed that the metallization of molecular hydrogen with static loading will soon be achieved (amorphous metallic hydrogen has already been formed by shock compression [4]).

Unfortunately, high pressure technology is still extremely limiting for the experimentalist. The restrictive geometry of high pressure cells and the attendant small sample volume defeat many experimental probes. However, there exists a collection of techniques well-suited for high-pressure studies of condensed matter. A large fraction of these methods rely on high energy x-rays from synchrotron sources. The capabilities and operation of modern synchrotron facilities are reviewed in section 3.1.

Several distinctly powerful applications of synchrotron x-rays can be utilized on elements that exhibit the *Mössbauer effect* [5] to provide data on high pressure systems that are inaccessible by any other technique. To wit, both the phonon spectrum and the hyperfine magnetic field distribution of the active species can be derived, in many cases simultaneously. As will be shown in chapter 3, the Mössbauer effect is a uniquely quantum mechanical phenomenon that is observed in specific isotopes of a small subset of the elements.

As luck would have it, the ^{57}Fe isotope of iron is among the Mössbauer isotopes.

*He won the Nobel Prize in 1946 for his discoveries in the field of high-pressure physics.

Iron is both an important structural material and a major component of the Earth's interior, and so understanding its high-pressure behavior is vital. However, there is also a great deal of science that also relates more generally to the properties of solids at high pressure than to iron, per se. Both approaches are indulged in this document.

Iron serves as an appropriate system for studying lattice vibrations in nanocrystalline metals. In the years following the synthesis of metallic crystals with grain diameters smaller than 50 nanometers, many investigators have found unusual features at low frequencies in the vibrational spectra of these materials. The elemental composition and the synthesis method of the crystals were found to have little effect on the nature of the vibrational anomalies. Rather, the bulk of the research into this problem has been concerned with the microstructure of the nanocrystalline material. Internal surfaces, pores and voids have been proposed as sources of atypical vibrations, in addition to several more exotic explanations. In chapter 4, experiments conducted with synchrotron techniques to investigate the influence of high pressure on the phonon density of states of nanocrystalline iron to a pressure of 28 GPa are described. To further investigate the role of the microstructure in low-frequency vibrations, inelastic neutron scattering was performed on a sample of nanocrystalline iron for neutron energy transfers in the range from 2 to 18 μeV at ambient pressure. These measurements indicate a strongly reduced role of surfaces and mesoscopic defects in the low-frequency vibrations of nanocrystalline materials and suggest the existence of novel "microstructural modes."

The second part of this thesis is concerned with the particular properties of iron metal rather than its archetypal behavior. Iron undergoes a solid-solid transformation from the body-centered cubic (α) phase to the hexagonal close-packed (ϵ) phase at a static pressure of 13 GPa. The properties of this hexagonal phase of iron have been a subject of great interest for decades, and one of the most contested topics is its magnetic ground state. The recent discovery of superconductivity in ϵ-Fe [1] has revived interest in the subject and spurred a new round of investigations into its magnetic behavior.

Computational techniques have played a key role in these new studies and have provided singular insights. Density functional theory (DFT) calculations of an antiferromagnetic ground state in ϵ-Fe [6] have shown that this state is more stable than the nonmagnetic phase while consistent with the experimental results. Interestingly, the compatibility of the proposed magnetic state with experiment requires a precise cancellation of the spin densities of the core and conduction electrons at the iron nuclei.

An integrated approach to understanding this putative antiferromagnetism in ϵ-Fe, utilizing both DFT calculations and direct experimental measurements, is described in chapter 6. The exact cancellation of electronic polarizations in the proposed phase presented a perfect case for dilute alloying with magnetic impurities, which have been shown to alter iron magnetic moments and spin populations in the bcc phase [7, 8]. Measurement and computation on real and virtual alloys, respectively, show that static antiferromagnetism in hcp iron is not adequate to explain the observed results.

In summary, the topics in this thesis have been made tractable by a remarkable confluence of diverse technologies. The popularization of the diamond anvil cell in concert with the unique capabilities of synchrotron facilities have enabled new insights into high pressure phenomena. Though the choice of iron as a subject material is both of practical and principal interest, future developments in technology are poised to extend the concepts explored here to other elemental and alloy systems.

Chapter 2

Methods of High Pressure Research

The role of pressure as the experimental variable in solid-state investigations has expanded significantly in the last half century due to the invention of the diamond anvil cell (DAC). Bridgman, correctly credited as the father of high-pressure physics, used apparatus that were large, unwieldy, and limited in attainable pressure. The development of the DAC at the National Bureau of Standards in 1959 opened the field to a wide range of new investigators.

2.1 The Diamond Anvil Cell

Pressure has the units of force per unit area. Naturally, investigators interested in extending the pressure range available to them have sought to increase the former while decreasing the latter.

The most common configuration for a pressure-generating device imposes compression uniaxially via opposed anvils. Early presses attempted to maximize the force applied through the use of hydraulic pistons driving conical carbide anvils with ground flats. The introduction of diamonds as anvils, with essentially the same principles at work, has changed the entire character of high pressure generation.

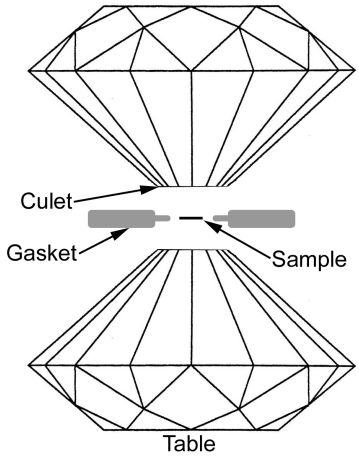

Figure 2.1: Exploded representation of the essential components of the diamond anvil cell.

2.1.1 Diamond Anvils

As the hardest material, and the second least compressible (osmium holds that distinction), diamond is extremely durable and difficult to deform, allowing diamond anvils to sustain high pressures before failure. Equally as important, it is transparent to electromagnetic radiation over a wide spectral range. This property allows probe beams to be transmitted directly through the anvils and facilitates sample observation. A popular gemstone, diamond can be cut and polished by well-established means. These attributes combine to produce a nearly ideal anvil material.

The portion of the diamond which contacts the sample, the *culet*, can be as small as 50 μm in diameter and is parallel to the *table*, the top of the diamond. Figure 2.1.1 illustrates the parts of the diamond and the axial-loading scheme. The anvil flat is usually parallel to the (1 0 0) or (1 1 0) plane. For reference, a culet of this size has an area of approximately 2000 μm^2, which for a modest force of 4 Newtons may produce a pressure ($P = F/A$) of 2 Gigapascals (GPa), or 20,000 atmospheres (1 atm = 101.2 kPa = 1.013 bar). Pressures as high as 100 GPa are routinely attained, and up to 560 GPa has been reached. [9]

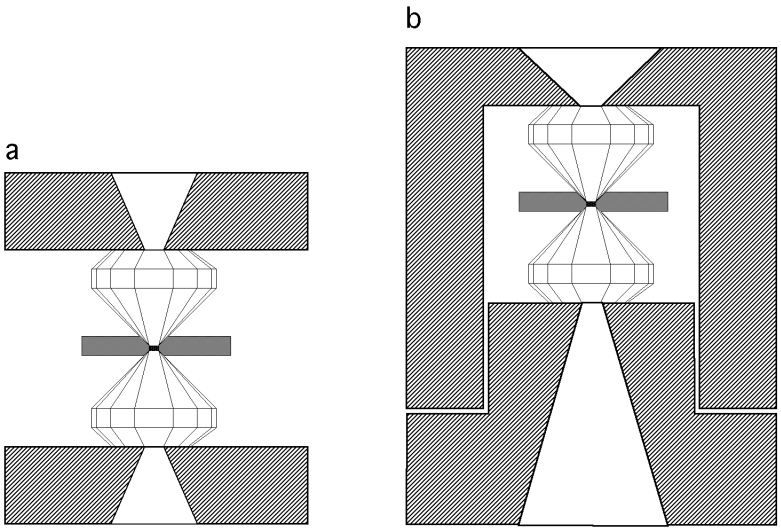

Figure 2.2: **a** The opposed plate cell; **b** The piston-cylinder cell.

2.1.2 DAC Variants

The opposed anvil design is uniform across the entire spectrum of DAC technology, but may be the only constant. A huge variety of cell designs have proliferated to satisfy the requirements of specialized experiments.

If our survey is confined only to the broadest of considerations, we can describe two categories of DAC. Named after their designers, the Mao-Bell [10] and Merrill-Bassett [11] cells are the dominant types of DAC currently in service. A diagram detailing the essential differences in these designs is shown in Figure 2.2. Also called the piston-cylinder cell, the two halves of the Mao-Bell cell mate within a very small tolerance, one fitting as a piston within the other. Four or six screws are used to decrease the anvil spacing and apply force on the sample. This design is very rigid and simple to align and can exert a high maximum pressure for exactly this reason. Its disadvantage is its closed geometry, which makes equatorial access to scattered radiation problematic. Newer piston-cylinder cells have partially solved this issue by cutting away some of the cylinder wall.

The Merrill-Bassett cell is commonly referred to as the opposed-plate cell. It is quite simple in design and very open in geometry, consisting of two similar plates which are retained by vertical rods. Three or six screws are used to generate pressure. The opposed-plate cell is limited in the maximum pressure it may generate as at higher pressures, the plates begin to flex along the anvil axis. This shortcoming is often ignored by investigators seeking an open sample geometry or an exceedingly compact size. Merrill-Bassett cells can be made very small and are often the only choice for work with some cryostats or with applied magnetic fields.

2.1.3 The Gasket

A key development in the overall utility of the diamond anvil cell has been the use of metal gaskets, which surround the sample and are compressed by the anvils, forming a sample chamber. Bridgman also used gaskets in his pioneering work, but these were aimed towards preventing the extrusion of his sample from between the anvil faces and for supporting the anvils themselves.

Bridgman's principle of massive support, as he named it, is still relevant. An unsupported conical anvil can support a compressive stress nK, where K is the yield stress of the anvil material. The value of n is unity for a cylinder and increases with the semi-cone angle, θ, to a value of 3 when $\theta = 90°$. When a deformable metal gasket is in place, it extrudes around the sloped faces of the anvil, providing further support to a diameter D, where D is greater than the culet diameter d. The maximum pressure in this case has been shown to be

$$P = 2K \ln\left(\frac{D}{d}\right) \tag{2.1.1}$$

Gaskets today still act to support the anvils significantly. More important, however, is the chamber that the gasket-anvil system creates. This chamber can retain a fluid pressure medium, which enables the pressure applied to the sample to be hydrostatic. This contrasts significantly with ungasketed operation, in which massive

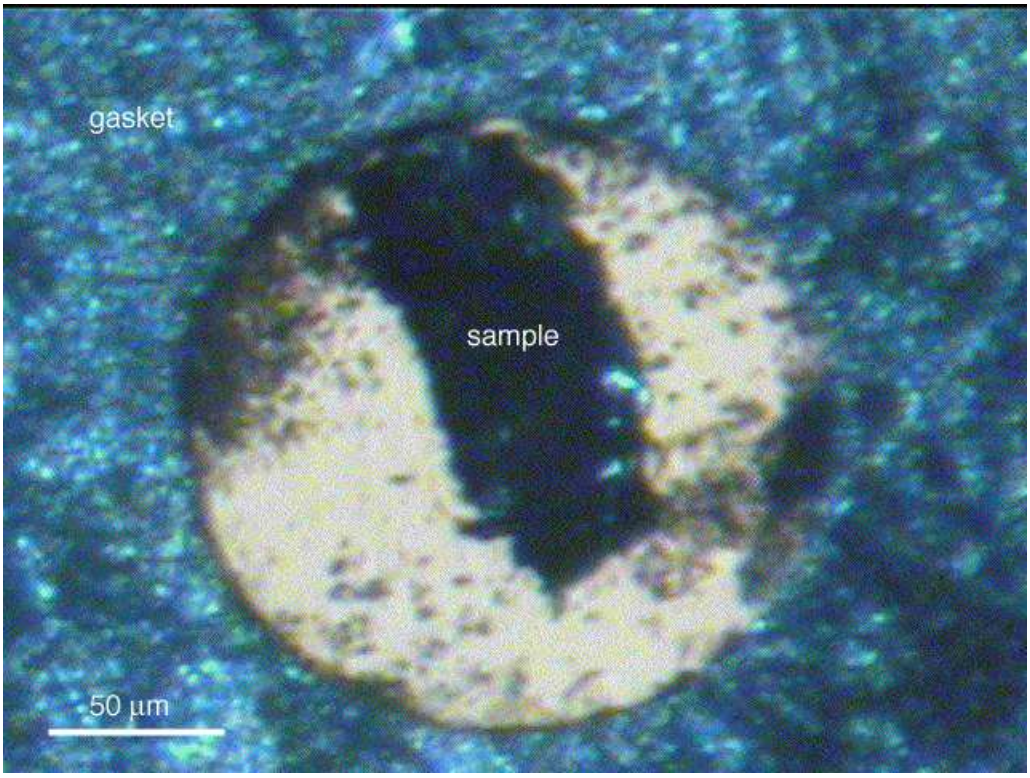

Figure 2.3: Optical micrograph of a sample of $Fe_{92}Ni_8$ in the sample chamber of a DAC. Axial view through the top diamond.

pressure (and thus, strain) gradients exist over the sample volume. Fluids such as silicone oil, methanol-ethanol, and cryogenic liquids such as Ar and Kr are used as pressure media. A view of the sample chamber is shown in Figure 2.3.

A gasket is typically cut from metal sheet with a thickness from 100 to 200 μm. An indentation is made in the gasket with the cell assembly. This deforms the gasket significantly, extruding material around the anvils and reducing the thickness of the central region. The heavy plastic deformation of the metal serves to provide massive support to the diamonds as well as strengthening the gasket itself against the extreme pressure it will face [12].

A hole must be made in the center of the indented region to create the sample chamber. As a rule of thumb, this hole must be less than half the diameter of the culet, which implies a requirement for high precision. Micro-drilling apparatus can be used to mechanically drill holes with $\sim$80 μm diameter. For smaller holes or for

difficult gasket materials, cutting by electrical discharge erosion is preferred.

A high yield stress is preferable for gasket materials. Stainless steel is often a good choice, but may be a problem for techniques which are sensitive to iron content. In these cases, materials such as rhenium or tantalum-tungsten are substituted. For experiments in which radiation must be transmitted through the gasket, beryllium may be used despite substantial restrictions related to the toxicity of its oxides.

2.1.4 Pressure Media

The key aspect of a pressure medium is the range over which it remains hydrostatic, that is, the range in which no shear stress is present. A perfect Newtonian fluid cannot support shear stress, and so is the ideal pressure medium.

However, under extreme pressures, any viable liquid solidifies. In some cases, a glassy vitreous phase is formed (silicone oil) or crystallization occurs (N_2, Ar, Kr). The common 4:1 methanol-ethanol mixture exhibits competition between vitrification and crystallization [13]. There is no simple way to get around this other than choosing a pressure medium with a high freezing pressure. For reference, argon solidifies at 1.2 GPa and 4:1 methnol-ethanol mixture freezes at 10.4 GPa. Helium was shown to freeze at 11.8 GPa but to remain hydrostatic to greater than 60 GPa [14].

2.2 Pressure Calibration Methods

Perphaps more than any other breakthrough, what has truly brought the DAC to the masses is the development of the ruby fluorescence pressure calibration technique at the National Bureau of Standards [15, 16, 17]. In this method, a laser is used to excite the R-lines of ruby ($Cr:Al_2O_3$). It so happens that the fluorescence wavelegth of these excitations shifts nearly linearly with pressure. The original correspondence was verified by the simultaneous measurement of R1 line position and x-ray diffraction from NaCl in a diamond anvil cell. The Decker equation of state [18, 19] was used to assess the pressure on NaCl from the derived lattice parameter. From this result, the

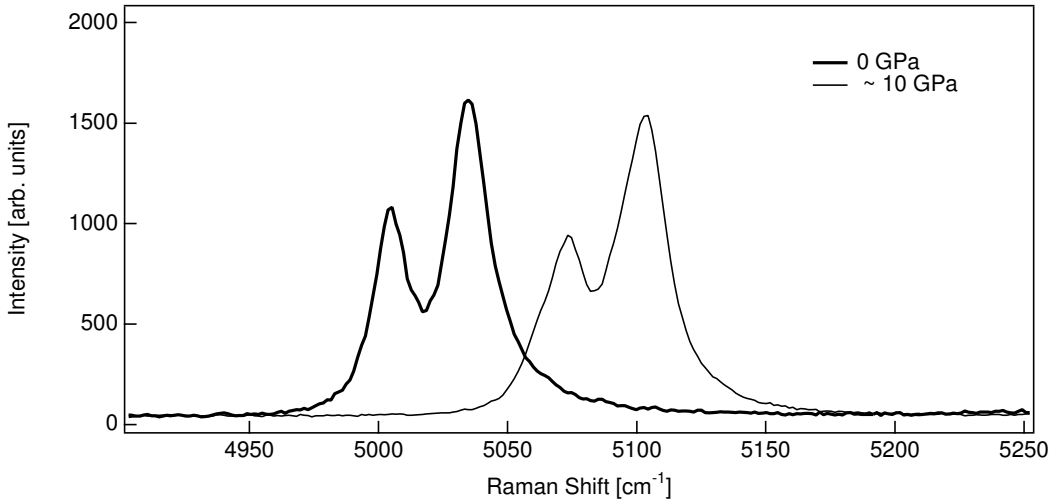

Figure 2.4: Ruby fluorescence measured in a diamond anvil cell at ambient pressure (bold line) and approximately 10 GPa (thin line) with an Ar-ion laser at 514.5 nm.

linear relation

$$P\,[kbar] = 2.746\,\Delta\lambda \tag{2.2.1}$$

was suggested, where $\Delta\lambda$ is the wavelength shift in Å referred to the R1 line position at 1 bar. This equation was later revised for pressures greater than 0.2 Mbar, to

$$P\,[GPa] = \frac{1904}{b}\left[\left(\frac{\lambda_0 + \Delta\lambda}{\lambda_0}\right)^b - 1\right]. \tag{2.2.2}$$

The parameter b takes the value of 5 for nonhydrostatic compression, and $b = 7.665$ for quasihydrostatic conditions [20]. An example of the use of the ruby scale is shown in Figure 2.4. These spectra were measured with an Ar ion laser at 514.5 nm. The wavelength shift in the figure indicates a pressure of 10 GPa in the compressed sample.

The semiempirical relations that define the ruby scale have been subject to continual refinement. For example, recent revisions to the scale have been made to cope with high temperature measurements on samples in laser-heated DACs. In x-ray diffraction measurements, it may be convenient to use an internal pressure standard such as NaCl [21].

2.3 Future Avenues for High Pressure Research

The future of high pressure research looks promising. High pressure science is still comparatively young, and many areas have yet to be explored. New technologies for pressure generation, simultaneous high P and T measurements, and the extension of existing characterization methods to the high pressure regime should add considerably to our understanding of matter in the years to come.

As discussed above, one of the key limitations of the current technology is the small sample size. Tiny sample volumes are incompatible to probes with low scattering cross-sections; namely, neutrons. Neutron scattering is the conventional way to obtain the phonon DOS of a material (see section 3.4 for a discussion of this topic). Inelastic neutron scattering can be applied to any system (not just Mössbauer isotopes) and returns either the entire phonon DOS (time-of-flight method) or the phonon dispersions (triple axis method) [22]. Moreover, neutron diffraction is an excellent means of determining crystal structures for which the positions of light elements are essential. Several new technologies are in development to cope with the limitation of small samples. The first is the construction of the Spallation Neutron Source (SNS) in Oak Ridge, Tennessee. The SNS will be the most powerful neutron source in the world, providing sufficient neutron flux for timely measurements at high pressure.

Another approach to the problem is being developed concurrently. Large single crystals of diamond are being grown from seeds via chemical vapor deposition, with prospects for multicarat anvils [23]. This plateau has already been reached with moissanite (SiC) anvils [24]. Moissanite, while attractive, is limited in strength and ultimate pressure.

Nonresonant x-ray inelastic scattering methods offer another alternative for high pressure studies, but must overcome multiple technical challenges. The inelastic x-ray scattering (IXS) [25] method relies on energy analysis by high-order reflections from highly perfect Si crystals. The momentum transfer, Q, of the coherent scat-

tering can be independently selected by choosing the scattering angle in the vertical scattering plane, and the energy transfer chosen by varying the temperature of the Si monochromator crystals. The high energy of the incident x-rays compared to phonon energies force the analyzer angles to be quite small, placing demanding geometrical constraints on the already cramped DAC. However, for materials highly absorbing of neutrons (H, Cd), IXS may emerge as an attractive means of measuring coherent phonon scattering at high pressures.

The combination of high pressure and high temperature is quickly becoming a core technique for the earth science community. Laser heated DACs [26] can reach several thousand degrees Kelvin, allowing greater insight into conditions near the Earth's center. The combination of high P and T is also attractive for the condensed matter physicist. The effects of the anharmonicity of the atomic potentials are of great importance in the context of materials thermodynamics; measurements of lattice vibrations in which the temperature and the lattice volume can be independently controlled would undoubtedly be of high impact.

Chapter 3

Nuclear Resonance Scattering

Nuclear resonance scattering (NRS) encompasses a host of experimental techniques related to the resonant absorption of x-rays and gamma rays by atomic nuclei. Many of these methods were conceived shortly after Mössbauer's work on recoilless emission [5], yet struggled to gain traction given the radiation sources available at the time. With the advent of powerful new synchrotron facilities, NRS studies have flourished.

Synchrotron radiation (SR) in general is an indispensable tool for experimental high-pressure physics. The high spectral flux and microradian divergence of undulator-derived x-ray beams are well suited for the challenges of experiments with pressure cells. High-pressure diffraction experiments with SR have enjoyed great success for decades.

The so-called "third generation" synchrotrons (APS,* ESRF,† SPRing-8‡) have been instrumental in the growth of NRS methods. Their characteristics are intimately tied to practical uses of NRS, and thus a brief survey of modern synchrotron facilities precedes the discussion of the theoretical concepts of NRS.

*Advanced Photon Source, Argonne, Illinois.
†European Synchrotron Radiation Facility, Grenoble, France.
‡Super Photon Ring 8 GeV, Harima, Japan.

3.1 Synchrotron Radiation Fundamentals

Early synchrotron operations were more concerned with producing high-energy particles than x-rays, and the byproduct x-rays radiated by the centripetal acceleration of the particles were considered a nuisance. Today the situation is reversed, and synchrotron sources are optimized for the production of extremely brilliant x-ray beams by the passage of electrons moving at close to the speed of light through tuned magnetic arrays. "Brilliance" is a measure of both photon flux and phase space density, and is typically expressed in units of $photons/s \cdot mrad^2 \cdot mm^2$ in a 0.1% bandwidth (*i.e.*, a bandwidth of 0.001 ω about frequency ω). State-of-the-art facilities produce beams 10^{11} times more brilliant than conventional x-ray tubes.

Though Lawrence's original cyclotron was a modest item, twenty-first century particle accelerators are gargantuan installations. The Advanced Photon Source in Argonne, Illinois, is the largest synchrotron in the United States. The circumference of the storage ring exceeds a kilometer. At the APS, electrons circulate in this evacuated storage ring, after acceleration by a linac and subsequently by a booster synchrotron. By the time they are "used," the electrons have energies of approximately 7 GeV. The electrons in the storage ring are confined to circulate in stable orbits called *buckets*. The relative occupation of these orbits by groups (*bunches*) of electrons creates a pulsed time structure in the emission of synchrotron radiation. At the APS, bunches typically carry 3 mA of current and furnish an x-ray pulse of 70 ps duration.

Early synchrotrons produced x-rays as a simple consequence of turning electron beams with bending magnets. Today, highly specialized magnetic arrays inserted in the beam are used to generate customized beam profiles. The configuration of these insertion devices greatly affects critical beam parameters such as angular divergence, peak brilliance, and polarization. Insertion devices are classified by the deflection parameter K, given by

$$K = 0.0934 \; \lambda_{ID} B_0$$

where λ_{ID} is the magnetic pole spacing in cm and B_0 is the peak magnetic field

in kG. Devices with $K \gg 1$ are called *wigglers*, while those with $K \approx 1$ are called *undulators*. High-pressure NRS studies are contingent on undulator insertion devices, which emit radiation in an exceedingly narrow cone biased along the axis of the device. Radiation from multiple alternating poles interferes coherently and produces sharp peaks at energies that depend on λ_{ID}. By adjusting λ_{ID}, the highest possible flux can be obtained at the desired experimental wavelength.

3.2 General Features of NRS

In any scattering process, multiple channels exist for the interaction of the incident wave and the scattering system. The incoherent inelastic channel of NRS is commonly exploited in the laboratory with radioactive sources and is known as Mössbauer spectrometry. As a complement, synchrotron NRS probes both coherent elastic and incoherent inelastic processes. Both methods possess unique isotopic selectivity that applies to a narrow range of elements. Fortuitously for metallurgists and earth scientists, iron, specifically the ^{57}Fe isotope, is one of these elements.

The isotopic selectivity of NRS is its defining characteristic, alternately acting as an advantage or a stumbling block. Nuclei suitable for NRS are often referred to as *Mössbauer isotopes* after Rudolf Mössbauer who identified the phenomenon of recoilless nuclear absorption in ^{191}Ir [5]. In a recoilless process, a photon may be absorbed by a bound nucleus without a change in the vibrational state of the host. The momentum of the photon, which must be conserved, is taken up by the entire crystal in which the nucleus is embedded. Quantum mechanics governs this process, establishing a probability of recoilless emission or absorption given by f_{LM}, the Lamb-Mössbauer factor. Only elements with appreciable values of f_{LM} are viable Mössbauer isotopes.

It is instructive to examine the expression for f_{LM} which applies to a single resonant atom in the simple harmonic oscillator potential. The atom is initially in an energy eigenstate of the harmonic potential, $|i\rangle = |n'\rangle$. Upon absorption of a photon

with wavevector k, there is a probability $P_{n' \to n''}$ that the nucleus will be in the state $|n''\rangle$. Since $|n'\rangle$ is not an eigenstate of the momentum operator, it behooves us to expand the initial state in plane waves characterized by their wavevector, k'.

$$|i\rangle = \sum_{k'} |k'\rangle\langle k'|i\rangle \tag{3.2.1}$$

After absorbing the photon, each basis wavefunction has its wavevector shifted by k, thereby conserving momentum.

$$|f\rangle = \sum_{k'} |k' + k\rangle\langle k'|n'\rangle \tag{3.2.2}$$

Conveniently, operating e^{ikx} on a plane wave will increment its wavevector by k, so

$$|f\rangle = \sum_{k'} e^{ikx}|k'\rangle\langle k'|n'\rangle \tag{3.2.3}$$

Using the closure property, equation 3.2.3 becomes

$$|f\rangle = e^{ikx}|i\rangle \tag{3.2.4}$$

The probability of the atom being in the energy eigenstate $|n''\rangle$ after absorbing the photon is given by the square of the expansion coefficient for the state $|f\rangle$:

$$P_{n' \to n''} = |\langle n''|e^{ikx}|n'\rangle|^2 \tag{3.2.5}$$

Recoilless processes are those with probability $P_{n' \to n'}$, that is, with no change in the vibrational eigenstate. The expression for f_{LM} in a harmonic potential is a familiar one; in discussions of diffraction it is known as the Debye-Waller factor.

$$f_{LM} = P_{n' \to n'} = e^{-k^2\langle x^2\rangle} \tag{3.2.6}$$

Here, $\langle x^2\rangle$ is the mean squared displacement of the the atom in the state $|n'\rangle$.

Table 3.1: Common NRS isotopes

Isotope	E_γ	Natural Abundance [%]	Γ [neV]
^{83}Kr	9.40	12.0	3.3
^{57}Fe	14.41	2.1	4.7
^{153}Eu	21.53	47.8	47.0
^{119}Sn	23.87	8.6	25.7

From the elementary (but broadly correct) expression for f_{LM}, it is clear that the recoilless absorption depends strongly on the photon energy and the average displacement of the atom in the solid. If only the ground state is considered, a tidy expression for f_{LM} may be derived:

$$f_{LM} = exp\left(\frac{-\hbar^2 k^2}{2M\hbar\omega}\right) \tag{3.2.7}$$

Recall that the ground state energy of the oscillator is $\frac{1}{2}\hbar\omega$. The quantity $\frac{\hbar^2 k^2}{2M}$ is precisely the increment to the kinetic energy imparted to a free atom which recoils on absorbing a photon; for that reason it is named the recoil energy, E_R. Thus,

$$f_{LM} = exp\left(\frac{-E_R}{\hbar\omega}\right) \tag{3.2.8}$$

It is now clear why only certain nuclei are suited for NRS studies. For systems with very high nuclear resonance energies, f_{LM} quickly approaches zero. A table of common Mössbauer isotopes to which synchrotron NRS can be applied appears in Table 3.1.

3.3 Elastic NRS

Nuclear resonant processes which transfer no energy to or from the radiation field are chiefly used as probes of hyperfine structure; that is, they are sensitive to perturbations of the nuclear energy level structure from interactions of the nucleus with the atomic electrons. These perturbations are infinitesimal compared with the magnitude

of E_0; for ^{57}Fe they are on the order of 10^{-7} eV ($E_0 = 14.4143$ keV). Nevertheless, due to recoilless emission these small shifts can be studied with ease.

3.3.1 The Hyperfine Interactions

There are three hyperfine interactions: the isomer shift, the electric quadrupole interaction, and the hyperfine magnetic field effect (also known as the nuclear Zeeman effect).

The isomer shift (or chemical shift) is an electrostatic effect that derives from the Coulomb interaction of electrons within the nuclear volume with the nuclear charge. This energy shift varies linearly with the electron density at the nucleus $\rho(0)$. The chemical environment of an active nucleus often changes significantly. The effect of the isomer shift is proportional to the difference of the squares of the radii of the ground and excited state, that is,

$$\Delta E = \alpha(R_e^2 - R_g^2)\rho(0) \tag{3.3.1}$$

where ΔE is the energy shift and R_e and R_g are the radii of the excited and ground state nuclei, respectively. The isomer shift has no effect on the recoilless absorption spectrum if the γ-ray source is the same material as the absorber. For this reason, isomer shifts are tabulated with reference to a standard, which for ^{57}Fe is the pure bcc phase.

The electric quadrupole effect is a consequence of the nonspherical charge distribution of the nucleus. Nuclei are prolate in shape, not perfectly spherical, and this asymmetry gives the nucleus an electric nuclear quadrupole moment. In the presence of an asymmetric electronic environment and thus an electric field gradient (EFG), the multiple possible orientations of the nucleus split the nuclear energy levels. A nucleus with spin I can be considered to have $(2I + 1)$ possible orientations with respect to an external axis such as the field gradient. For ^{57}Fe, the ground state has $I = \frac{1}{2}$ and the excited state has $I = \frac{3}{2}$. The ground state can assume spin values

$I_z = \pm\frac{1}{2}$ and the excited state has possible I_z values $\frac{1}{2}, -\frac{1}{2}, \frac{3}{2}, -\frac{3}{2}$. For the purposes of orienting an ellipsoid, states with $I_z = \pm\frac{1}{2}$ are indistinguishable and remain degenerate, as are states with $I_z = \pm\frac{3}{2}$. The remaining transitions admitted are from $I_z = \pm\frac{1}{2} \rightarrow I_z = \pm\frac{1}{2}$ and $I_z = \pm\frac{1}{2} \rightarrow I_z = \pm\frac{3}{2}$. When the Mössbauer isotope is in an environment with cubic symmetry, there is no EFG, and hence no level splitting. Chemical disorder is sufficient to disrupt this symmetry and induce a quadrupole energy splitting.

The hyperfine magnetic field (HMF) effect is due to the coupling of a magnetic field and the magnetic moment of the nucleus by the perturbation Hamiltonian

$$\mathcal{H}' = -\mu \cdot \mathbf{H}_{eff} \tag{3.3.2}$$

where $\mathbf{H}_{eff}$ is the effective magnetic field at the nucleus and μ is the nuclear magnetic moment. In the above expression the source of this effective field is not specified. In fact, the sources of the field in question are manifold.

In bcc iron, by far the largest contribution to the field is from the Fermi contact interaction. The contact field is a result of nonzero electron polarization at the nucleus due to a disparity in the population of spin-up and spin-down electrons. The expression for this contact field due to a single electron is

$$\mathbf{H}_{eff} = \frac{8\pi}{3} g_e \mu_B S \; |\psi(0)|^2 \tag{3.3.3}$$

Here, g_e is the gyromagnetic ratio of the electron, μ_B is the Bohr magneton, S is the electron spin ($\pm\frac{1}{2}$), and $\psi(0)$ is the electron wavefunction at the nucleus. As only s electrons have nonvanishing wavefunctions at the nucleus, they are the only participants in the generation of the contact portion of the effective field (this is not strictly true for heavier elements, for which relativistic effects distort the radial wavefunctions). The other electrons do participate, however, by acting to polarize the spin of the s electrons, such that even "paired" electrons in core levels can generate effective fields. The topics of spin polarization of s electrons and the resulting hyperfine fields

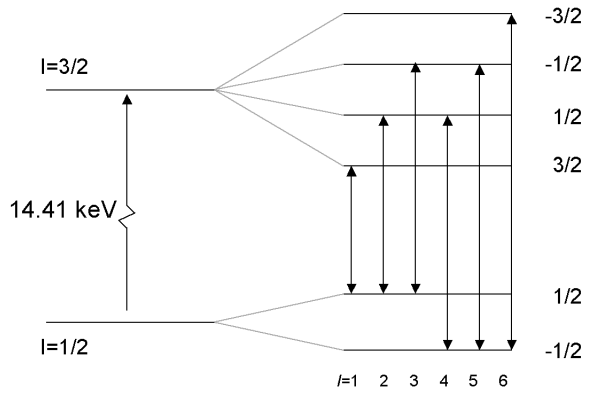

Figure 3.1: Nuclear energy levels of ^{57}Fe split by the hyperfine magnetic field.

are covered in more detail in chapters 5 and 6.

The other components of the hyperfine magnetic field can be labeled H_{mag}, H_{orb}, and H_{dip}, for the fields due to lattice magnetization, orbital magnetic moments, and classical dipole magnetic moments, respectively. These contributions are usually quite small in comparison to the contact field, but some irregular cases exist. H_{orb} can be very large in certain rare earth and actinide ions due to the $4f$ and $5f$ electrons, for example.

In the case of bcc ^{57}Fe the hyperfine magnetic field takes the value of –330 kG (–33 T), which reflects that the hyperfine field is oriented oppositely to the lattice magnetization. The presence of a HMF breaks the rotational symmetry of the nuclear environment completely, splitting the ground state into two levels and the excited state into four. However, the dipole selection rule $I_z = 0, \pm 1$ limits the total transitions to six. The level scheme of ^{57}Fe in the presence of a HMF is shown in Figure 3.1 along with the allowable transitions.

3.3.2 Synchrotron Mössbauer Spectrometry

A synchrotron flash with meV bandwidth will excite all of the hyperfine-split nuclear transitions in a sample simultaneously. After excitation at time zero, the nuclei decay and emit recoilless photons with slightly different frequencies. In an analogous

fashion to acoustic phenomena, the superposition of these waves creates beats. The time-resolved pattern of these quantum beats can be used to determine the nature of the hyperfine interactions in the scattering system.

The measurement of temporal beats is contingent on coherence in the scattered radiation. Of the primary channels available for the de-excitation of the nuclear state, radiative decay leads to coherence, while internal conversion does not. Atoms which eject an electron are distinguishable from the rest of the ensemble, and radiate conversion x-rays isotropically. In contrast, atoms which return to their initial state after emission of a photon are indistinguishable and radiate quanta which may interfere constructively.

The existence of coherent nuclear scattering implies the existence of a state in which a nuclear ensemble is collectively excited by a single resonant photon. The wavefunction for this state, the nuclear exciton, is a superpositon of states in which one atom is in the excited state while the rest are in the ground state. This wavefunction can be expressed

$$|\Psi(\mathbf{k}_0)\rangle = \frac{1}{\sqrt{N}} \sum_j e^{i\mathbf{k}_0 \cdot \mathbf{r}_j} |g\rangle |e_j\rangle \tag{3.3.4}$$

where k_0 is the wavevector of the resonant x-ray, and $|g\rangle|e_j\rangle$ indicates the nucleus at $\mathbf{r_j}$ is in the excited state $|e_j\rangle$ and all others are in the ground state $|g\rangle$.

In the nuclear exciton picture, the nuclear ensemble behaves like a macroscopic resonator with different properties from a single nucleus. Among these emergent properties are the phenomena of speed-up, dynamical beats, and quantum beats.

Dynamical (or propagation) beats and speed-up effects are seen in samples with effective thickness $T \gg 1$, where T is defined:

$$T = \sigma_0 \, f_{LM} \, N \tag{3.3.5}$$

Here, σ_0 is the resonant cross section and N is the areal density of active nuclei.

When the number of nuclear resonators is large, quanta may be exchanged extensively between nuclear excitation and the radiation field. Each upstream atom becomes a source of secondary radiation which drives the oscillation of downstream atoms. In this case, the nuclear exciton behaves as a driven oscillator and exhibits a mean lifetime reduced with reference to an isolated nucleus. This acceleration of the nuclear decay is aptly named "speed-up," and is loosely analogous to the phenomenon of stimulated emission.

A consequence of speed-up is the broadening of the nuclear resonance, due to the uncertainty relation. Multiple scattering in the wings of the resonance is especially efficient, and leads to the formation of a "double-hump" [27] frequency spectrum of the forward scattered radiation. The two peaks in this distribution may interfere to form propagation beats in the time spectrum. The time dependence of the transmitted amplitude is given by

$$A(t) = \delta(t) - \gamma e^{-t/2\tau_0} \frac{J_1(2\sqrt{\gamma t})}{\sqrt{\gamma t}} \tag{3.3.6}$$

where J_1 is the first-order Bessel function, τ_0 is the natural lifetime, and

$$\gamma = \frac{k_0 d f_0}{\tau_0}.$$

Here, k_0 is the magnitude of the incident photon wavevector, and f_0 is

$$f_0 = \frac{f_{LM}}{2k_0} \frac{2I_e + 1}{2I_g + 1} \frac{1}{1 + \alpha}$$

where I_e and I_g are the spins of the nuclear excited and ground states, respectively, and α is the internal conversion coefficient.

The phenomena discussed above can be observed in resonant media with a single resonance line; they are *intra*resonance effects. When multiple resonance lines are resolved, such as in the presence of an EFG or HMF, *inter*resonance effects are seen. These quantum beats are measured in concert with the dynamical beats, or for thin

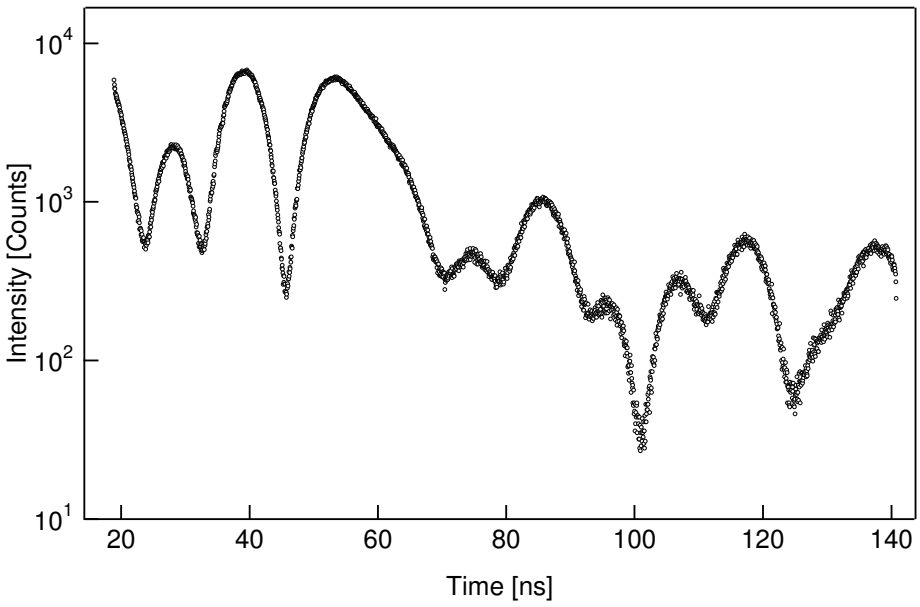

Figure 3.2: A synchrotron Mössbauer spectrum from a ferromagnetic $^{57}Fe_{48}Rh_{52}$ alloy measured at the APS. The time between synchrotron pulses was 153 ns.

magnetic samples, in their absence. The measurement and analysis of quantum beat patterns allows one to extract the number and nature of the hyperfine levels in a sample. The quadrupole splitting or hyperfine magnetic field is the goal, which in turn can be analyzed to get the electric field gradient or spin density at the nucleus. This analysis requires specialized software to fit the superimposed dynamical and quantum beat pattern. All the analyses of NFS spectra in this thesis were performed with the program CONUSS [28].

3.3.3 Radioactive-Source Mössbauer Spectrometry

Nuclear resonant scattering of synchrotron x-rays is a powerful technique, but by no means common. Most recoilless scattering experiments are performed with a radioactive source that emits resonant photons.

In the case of the ^{57}Fe absorber, ^{57}Co in a Pd or Rh matrix is used as a source. ^{57}Co decays by electron capture, to an excited state of ^{57}Fe, which subsequently emits the resonant γ-ray. The source is mounted on a mechanical velocity transducer which

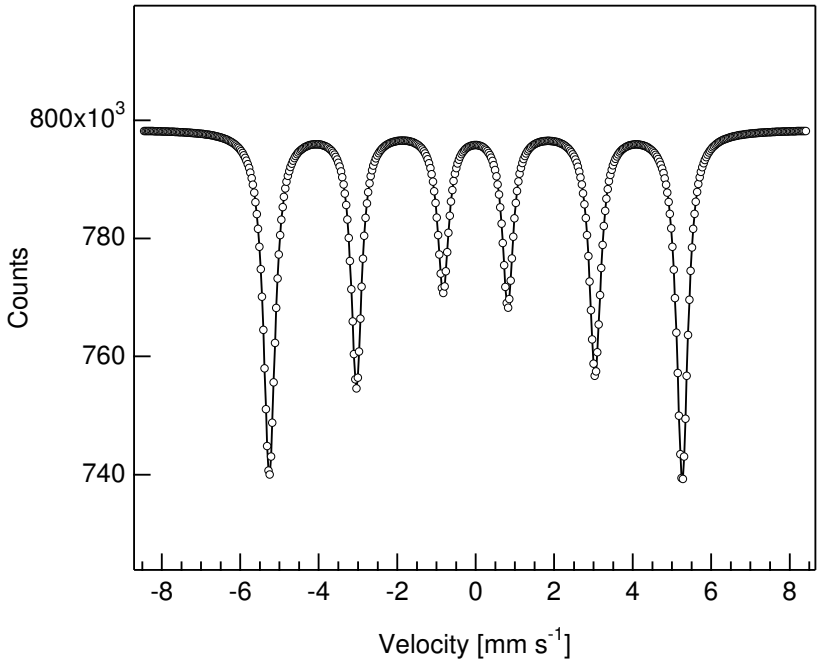

Figure 3.3: An example transmission Mössbauer spectrum from α-Fe.

shifts the energy of the γ-rays incident on the absorber via the Doppler effect. For energy splittings in the neV range, mm/s velocities are sufficient. Most experiments are configured in the transmission geometry, in which the number of resonant photons are counted with respect to the Doppler energy shift. At a resonance line, absorption is greatly increased, leading to the dip in counts which is characteristic of Mössbauer absorption spectrometry. This is necessarily an incoherent process, as the absorbed photons are reradiated into 4π and do not impinge on the detector.

Experiments with thick samples can also be performed in the backscattering geometry, in which the conversion electron associated with nuclear decay is detected. In contrast to transmission experiments, conversion electron Mössbauer spectra are characterized by peaks at the resonance energies.

Data from nuclear resonant scattering experiments with radioactive sources are undoubtedly easier to interpret than synchrotron time spectra. Absorption peaks can be fit using standard least-squares means, and their relative areas are tabulated for isotropic media.

Coherent Mössbauer scattering using radioactive sources has recently met with some success as well. Nuclear Bragg scattering has been isolated from disparate chemical environments in the Fe_3Al system. [29]

3.4 Nuclear Resonant Inelastic X-ray Scattering

Nuclear Resonant Inelastic X-ray Scattering (NRIXS) is the inelastic complement of SMS. The primary function of NRIXS is the measurement of the partial phonon density of states (PDOS) of the active nuclei in a sample. It differs fundamentally from other means of measuring the vibrational spectrum of a solid. In most inelastic scattering experiments, the initial energy of the probe is known and the final energy of the probe is measured; energy conservation demands that the deficit is the energy of the excitation being probed. In NRIXS experiments, the resonant nuclei in the sample *are* the analyzer, and simple counting of fluorescence photons is sufficient to determine the vibrational spectrum.

The "phonon-assisted Mössbauer effect," is an alternate term for NRIXS which describes the physics involved. A consequence of recoilless emission and absorption is an extremely sharp resonance (4.66 neV in ^{57}Fe). A photon which is detuned from the resonance energy may scatter inelastically, acquiring the appropriate energy to excite the nuclear transition. Since the transition energy is known, if the incident photon energy is known, it is simple to find the energy of the excitation from which the photon scattered. NRIXS experiments are a matter of detecting resonant events as a function of detuning from the nuclear resonance.

A simple model can be very useful in detailing the essential physics of NRIXS. First consider an Einstein solid with vibrational frequency ω_E, containing a nucleus with ground state $|g\rangle$ and excited state $|e\rangle$, separated by the energy E_0. A quantum state for this system can be specified by the state of the nucleus and a vibrational quantum number (i.e., the number of phonons in the system). For example, the state $|g\rangle|1\rangle$ indicates the nucleus is in the ground state and one phonon is present. This

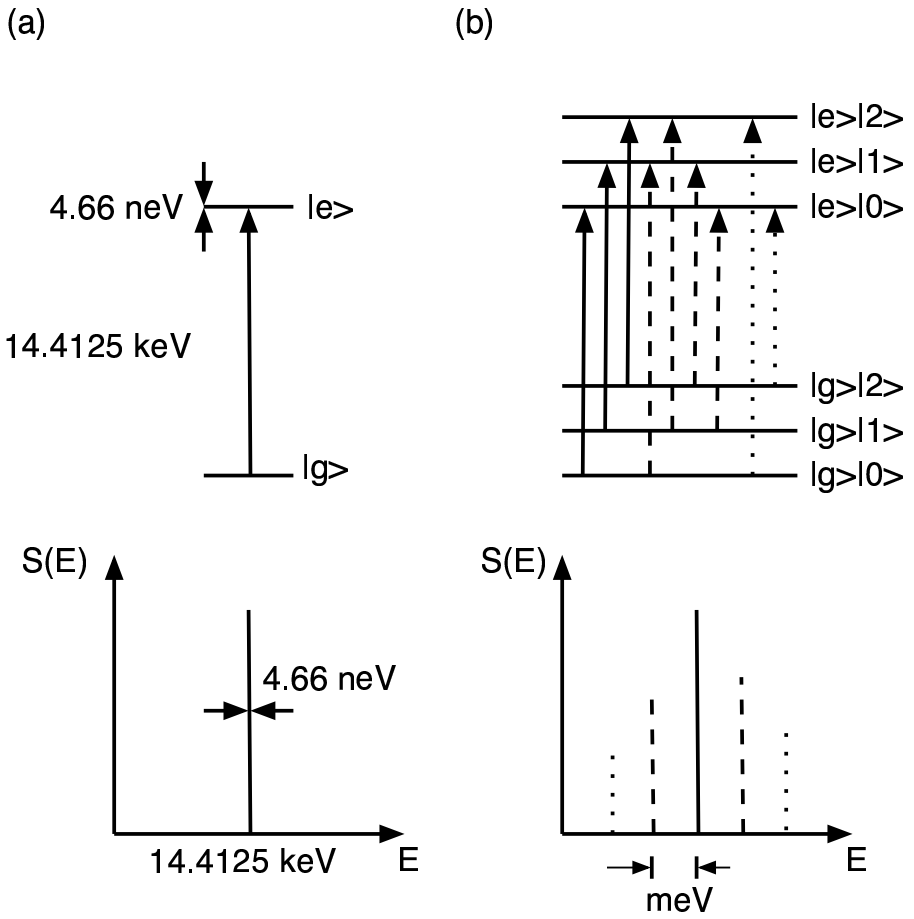

Figure 3.4: **a** Nuclear energy levels of a fixed ^{57}Fe nucleus; **b** Coupled energy levels for a ^{57}Fe nucleus in an Einstein solid. Adapted from [30].

level scheme is presented schematically in Figure 3.4. Properly tuned x-rays can cause transitions between the energy levels of the coupled system. An x-ray with energy $(E_0 + n\hbar\omega_E) = (E_0 + E)$ may excite the transition

$$|g\rangle|m\rangle \rightarrow |g\rangle|m+n\rangle \tag{3.4.1}$$

which corresponds to the creation of n phonons.

The nucleus, once excited, decays with a characteristic time τ. The decay to the ground state occurs by the emission of a photon of energy E_0, or by internal conversion, which produces an ejected core electron and accompanying K-shell fluorescence.

By counting only these products of nuclear de-excitation as a function of detuning E from the resonance energy E_0, the excitation probability density $S(E)$ can be found. Though $S(E)$ is trivial for the Einstein solid, these principles are readily extensible to real solids.

Values of τ are large for Mössbauer isotopes as a consequence of their narrow level width, since $\Delta t \simeq \hbar/\Delta E$. This is critical to practical applications of NRIXS. Away from the resonant energy, a synchrotron x-ray pulse leads to copious electronic scattering that overwhelms "phonon-assisted" scattering. However, the time scale for this scattering is typically nearly instantaneous ($< 10^{-12}$ s), while excited nuclei decay with the probability

$$P = \frac{1}{\tau}\, exp\left(\frac{-t}{\tau}\right) \tag{3.4.2}$$

For ^{57}Fe, $\tau = 141$ ns. Delayed events can be counted very efficiently by waiting for the initial burst of electronic scattering to subside.

The yield of delayed photons with respect to the detuning energy E, $I(E)$, is directly related to the excitation probability density $S(E)$. If the interatomic potential of the sample is assumed to be harmonic, the excitation probability density may be expanded in terms of n-phonon contributions. Figure 3.5 depicts the excitation spectrum of ^{57}Fe decomposed into $n = 0, 1, 2$ and $n \geq 3$ components.

$$S(E) = f_{LM}\left(\delta(E) + \sum_{n=1} S_n(E)\right) \tag{3.4.3}$$

Here f_{LM} is the Lamb-Mössbauer factor, the probability of recoilless scattering, so the term $f_{LM}\delta(E)$ describes elastic (0 phonon) scattering. The one-phonon term can be expressed

$$S_1(E) = \frac{E_R\ D(E)}{E(1 - e^{-\beta E})} \tag{3.4.4}$$

E_R is the recoil energy, $\beta = \frac{1}{k_B T}$, and $D(E)$ is the partial phonon density of states of

the active nuclei in the sample. Higher-order terms S_n are given by

$$S_n = \frac{1}{n f_{LM}} \int S_{n-1}(E') S_1(E - E') dE' \tag{3.4.5}$$

$S_1(E)$ and $D(E)$ are unknown *a priori*, and depend on each other. Iterative procedures are typically used to solve problems of this nature. However, $S_1(E)$ may be derived directly from equation (3.4.5) by the "Fourier-log method." Briefly, by applying a Fourier transform to equation (3.4.5), the convolutions become products, allowing

$$\frac{\tilde{S}_n}{f_{LM}} = \frac{1}{n!} \left(\frac{\tilde{S}_1}{f_{LM}} \right)^n \tag{3.4.6}$$

If this result is substituted into the transform of 3.4.3,

$$\tilde{S} = f_{LM} + \sum_{n=1} \tilde{S}_n = f_{LM} \frac{1}{n!} \sum_{n=0} \left(\frac{\tilde{S}_1}{f_{LM}} \right)^n \tag{3.4.7}$$

The form of 3.4.7 is a familiar one, and thus

$$\tilde{S} = f_{LM} \; exp \left(\frac{\tilde{S}_1}{f_{LM}} \right) \tag{3.4.8}$$

and applying the inverse transform gives an expression for $S_1(E)$:

$$S_1(E) = \mathcal{F}^{-1} \left[f_{LM} \; \ln \left(\frac{\tilde{S}}{f_{LM}} \right) \right] \tag{3.4.9}$$

Once $S_1(E)$ has been determined, it is a straightforward matter to calculate the phonon density of states. Using the principle of detailed balance for the scattering probability

$$S_1(-E) = e^{-\beta E} S_1(E) \tag{3.4.10}$$

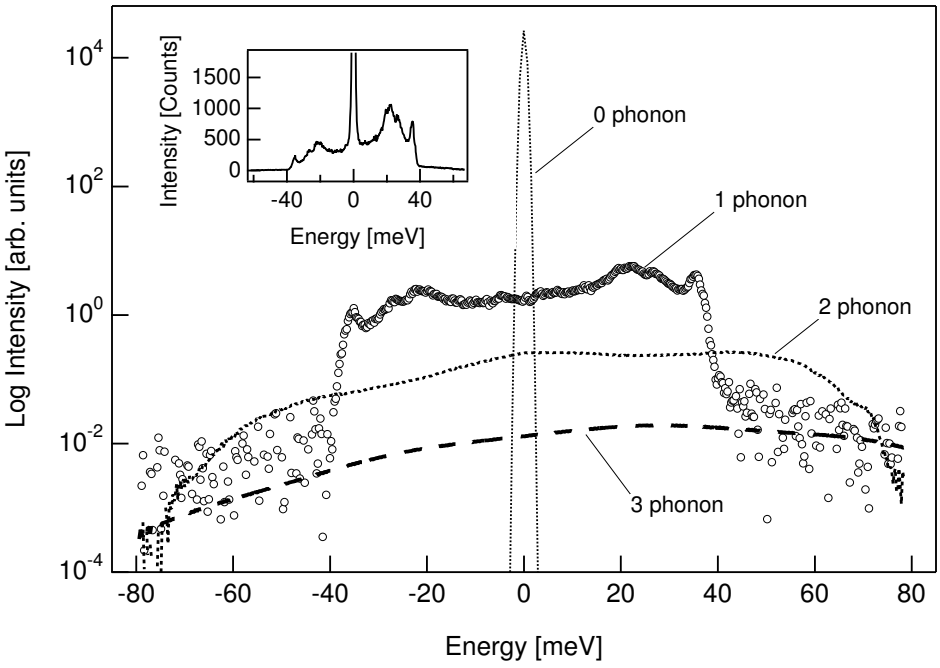

Figure 3.5: NRIXS spectrum from ^{57}Fe illustrating the multiphonon components. The spectrum is shown on a linear scale inset.

both wings of the excitation spectrum can be used to determine D(E).

$$D(E) = \frac{E}{E_R}\, tanh\left(\frac{\beta E}{2}\right)(S_1(E) + S_1(-E)) \tag{3.4.11}$$

3.4.1 Isotopic Selectivity of NRIXS and the Partial Phonon Density of States

An important feature of NRIXS is that it provides data on vibrations of only active nuclei in the sample. That is, the data can provide no more than the partial phonon density of states (PDOS) of the resonant species in the sample. Specifically, the PDOS for species X in a compound is given by

$$D^X(E) = \left\langle \sum_j \left|\sigma_j^X(\mathbf{q})\right|^2 \delta(E - E_j) \right\rangle \tag{3.4.12}$$

where σ_j^X is the polarization vector of an X atom for the j^{th} vibrational mode. The average $\langle\rangle$ is over all X atoms.

The isotopic selectivity of NRIXS is often a mixed blessing. Small amounts of corrosion or environmental contamination can usually be ignored. This contrasts with the case of inelastic neutron scattering (INS), which can be heavily influenced by trace amounts of hydrogen, for example. NRIXS-derived PDOS are invaluable in providing checks on neutron weight corrections for INS experiments involving species with notably different scattering strength. NRIXS has also been used successfully to isolate the vibrations of buried layers in heterostructures, and may be the only tool capable of this task.

The negative traits of the chemical sensitivity of NRIXS are exposed when the complete density of states of an alloy system is required. In ordered binary alloys, the PDOS may be inverted using a Born–von Karman model to iteratively arrive at the interatomic force constants. The derived force constants can then be used to generate a total DOS. Disordered systems, as is often the case, are inaccessible by this particular method.

3.5 Instrumentation for High-Pressure NRS

A highly brilliant x-ray beam is just the first requirement for the implementation of a synchrotron NRS beamline. A generic representation of such a system is shown in Figure 3.6. Let us follow the x-rays "downstream" and assess the function of each element of the beamline in turn.

The pole spacing of the undulator at the beamline is tuned, of course, to the resonance energy E_0. Though peaked at this energy, the x-ray spectrum is still broadband.

The first optical element the beam encounters is the premonochromator (PM) or high heat load monochromator. The enormous photon flux of the beam is not amenable to meV monochromatization in a single step, and the premonochromator

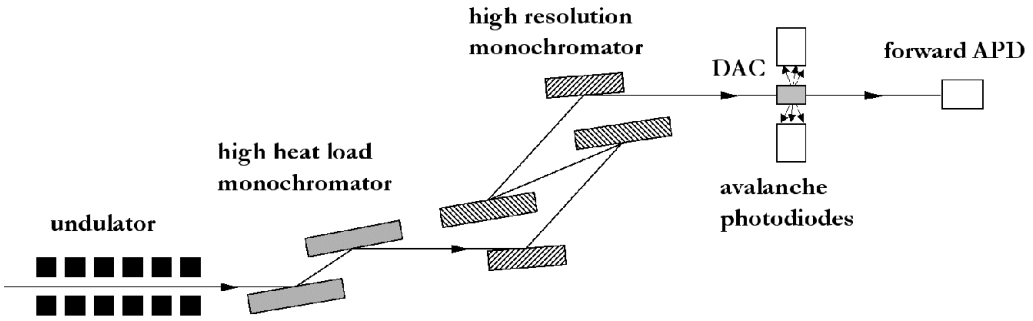

Figure 3.6: Schematic of an NRS beamline.

is the first of two. The PM filters the initial bandwidth to a few eV, usually from a symmetric low-order crystal reflection such as Si (1 1 1) or Diamond (1 1 1). These crystals are water-cooled to dissipate the massive heat created by the impingement of the x-ray beam. In the case of diamond, its relative transparence aids in this dissipation, in that much of the beam passes unhindered.

While the PM is a permanent installation at the NRS beamline and can be tuned for various E_0 values, the high resolution monochromator (HRM) is specific to each isotope. HRMs are exclusively constructed from Si crystals due to the high degree of perfection required. There may be as many as four asymmetric reflections from high-order planes. The 875 μeV ^{57}Fe monochromator at the APS utilizes four flexure-mounted Si crystals oriented for (4 0 0)(10 6 4) reflections.

At some beamlines, a final piece of beam optics is used to focus the beam to miniscule dimensions ideal for DAC work. Though not depicted in the diagram, Kirkpatrick-Baez (KB) mirrors can focus the beam to dimensions of 10×10 microns. The mirrors are thin pieces of sagitally-bent Si, one for each focusing axis.

The focused, monochromatic beam then impinges on the sample in the DAC, which itself is not a trivial matter. For SMS, a negligible solid angle is necessary for detecting the scattered radiation. However, NRIXS is inchoherent, and the delayed fluorescence is emitted into 4π. One would like to intercept the greatest solid angle

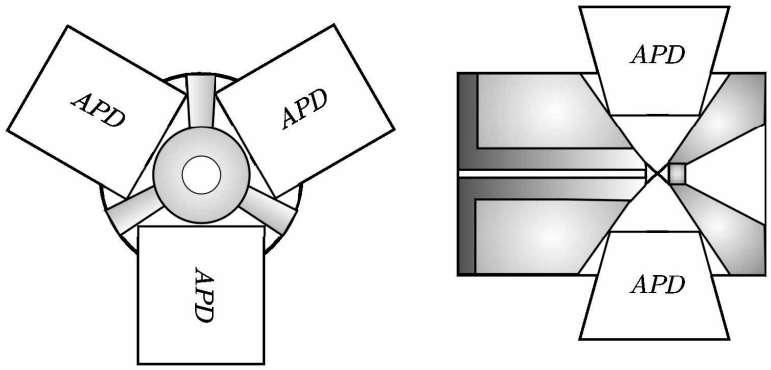

Figure 3.7: Cutaway views of the panoramic diamond anvil cell for NRIXS experiments. Adapted from [3]. Note the close approach of the avalanche photodiode detectors (APD).

possible to obtain the highest count rate, but most traditional DAC designs do not offer an easy approach. A special "panoramic" cell was developed by Mao [3] which features equatorial access to the sample (Figure 3.7). Beryllium gaskets must be used to transmit the 6.4 keV conversion x-rays. In contrast, heavy non-ferrous gasket materials such as Ta-W and Re are preferred for SMS to eliminate contaminants to the beat pattern. The detector configuration for NRS differs based on the particular method. For NRIXS, multiple detectors are situated as closely to the sample as possible to intercept the maximum solid angle, and a forward detector is placed far from the sample to measure the resolution function of the monochromator. SMS, as one would expect, requires only this forward detector. Detectors for NRS do not require energy resolution, as the time delay of the radiation ensures its nuclear resonant nature. Resolution of features in the DOS by NRIXS is set by the HRM; resolving the quantum beat patterns of SMS is contingent on the time resolution of the detector, which should be better than 1 ns. Additionally, detector noise must be negligible, since counting rates in high-pressure NRIXS are often near 1 Hz, even with enriched samples. These requirements turn out to be rather stringent, especially in light of the fact that any detector must endure the prompt x-ray pulse of approximately 10^8 Hz. The avalanche photodiode meets all of these requirements, and is the detector of choice for NRS.

Chapter 4

Vibrational Modes in Nanocrystalline Iron

4.1 Introduction

The term "nanostructured" is broadly applied to materials with features on the nanometer scale. Structural modulations in this range have been shown to impart unique, or at least distinct, properties to materials that possess them. Nanocrystalline materials are a subset of this greater class of nanostructured materials. The terminology in use varies, but here I will apply this definition to three-dimensional solids composed of nanometer-sized, randomly oriented single crystals which meet at grain boundaries. Polycrystals on this scale are sufficiently small that the interface volume fraction of the polycrystal approaches that of its purely crystalline environments. Assuming cubic grains of dimension L with boundary thickness δ, the volume fraction of boundaries (to first order in δ) is $3\delta/L$. Values of δ in real materials are on the order of 1 nm [31], so the interfacial volume fraction becomes significant at grain sizes lower than 100 nm. These plentiful interfacial zones do not possess the symmetry of the crystalline grain interiors, presenting significant challenges for the traditional methods of condensed matter physics that require strict periodicity. A simplified illustration of a nanocrystalline material is shown in Figure 4.1.

Nanocrystalline aggregates are not typically produced in the hermetic environments of ultra-high vacuum, but by more humble and messy means such as high-

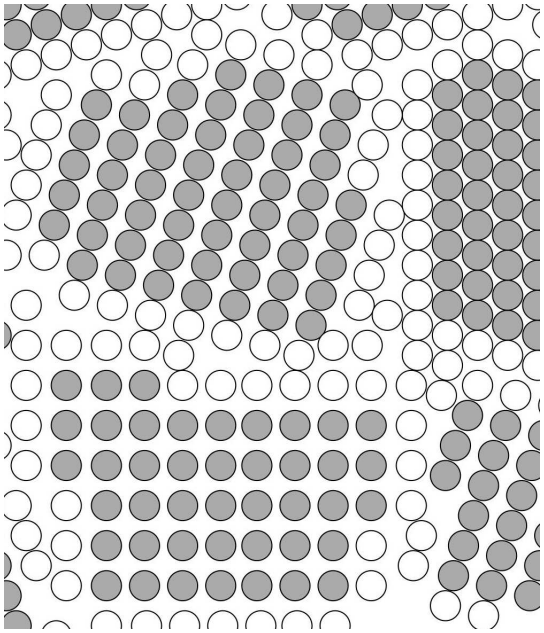

Figure 4.1: A simplified representation of a nanocrystalline material. The shaded circles represent atoms in the grain interiors and the unshaded atoms are grain boundary atoms.

energy ball milling [32] or inert gas consolidation [33]. It is not strictly possible to "design" these materials in the manner of some semiconductor nanostructures, though some control may be exerted over the mean grain size. Nevertheless, significant applications have already been found for these ultrafine polycrystals. Nanocrystalline metal nitrides are of great interest for ultrahard wear-resistant coatings [34], and nanocrystalline Si and Ge have demonstrated impressive reversible capacities for Li metal storage for battery applications [35].

4.1.1 Anomalous Phonons in Nanocrystalline Metals

Metallic nanocrystals have stimulated particularly intense attention since their synthesis became common in the 1990s. Though many audacious claims regarding the nature of these materials have been refuted (most notably the hypothesis of a "frozen gas" structure [36]), fundamental questions remain. One of the most confounding problems is the significant differences in the phonon spectra of nanocrystalline materials compared to their large-grained fellows.

The phonon density of states (DOS) of a solid can be described as a histogram of its normal mode frequencies. Mathematically, it can be defined

$$D(E) = \frac{1}{3N} \sum_{j}^{3N} \delta(E - E_j) \tag{4.1.1}$$

where the sum is over all modes j in the crystal with N atoms, and mode j has energy E_j. The phonon DOS is a fundamental thermodynamic quantity with primary influence on the heat capacity and vibrational entropy [37]; distortions in the spectrum are borne out in altered thermal properties and relative phase stability. Basic understanding of phonons in nanostructures may allow purposeful modification of these properties for applications such as thermal barriers or tribological coatings for which heat conduction and dissipation are important. Moreover, the ever-decreasing size of electronics and the concomitant increase in electron throughput in these structures demands detailed knowledge of heat dissipation and any anomalies specifically associated with nanostructures.

Neutron and x-ray inelastic scattering experiments have been used to identify significant distortions in the phonon DOS of nanocrystalline metals in several distinct systems [38,39,37,32,40,41,42]. The common characteristic of each DOS is an excess of vibrational modes at both of the extremes of the vibrational spectrum. Enhanced intensity above the high-energy cutoff of the bulk material has been attributed to phonon lifetime broadening caused by phonon interactions with grain boundaries [40, 39, 38] and recent measurements on iron have isolated a contribution from surface oxides [41].

The low-energy region of the vibrational spectrum of nanocrystals is less well understood. There is general agreement that nanostructured materials have dynamical degrees of freedom that do not exist in bulk crystals, and these degrees of freedom make a significant contribution to their vibrational spectra at thermal energies. The physical origin of these vibrational modes has been the subject of speculation and debate. Cooperative dynamics of the crystals themselves were suggested [43,39], as were

surface modes involving elastic discontinuities between nanocrystals. It has been suggested that nanocrystals could have novel two-dimensional vibrational modes owing to their large surface area. Some evidence for two-dimensional behavior has been provided by theory [44,45] and experiment [46], although most experimental work reports no linear component of the phonon DOS at low energies [37, 32, 40, 39, 38, 41]. Non-integral spatial dimensions of the low frequency modes have been suggested [47, 48], such as fractal modes or "fractons" [49].

High pressure studies offer an original avenue for increasing our understanding of this problem. The large interface volume fraction in nanocrystals presents an opportunity to probe the interatomic force constants of grain boundaries, which are directly related to the phonon frequencies. Gigapascal pressures significantly decrease the sample volume and shift the phonon frequencies to a degree that may be influenced by the nature of each mode (such as modes which are non-propagating or localized). Additionally, hydrostatic stress also drives the disappearance of pore and void defects. Any assumption that defects of this type are a source of atypical vibrations demands the reduction of this effect upon significant void collapse. A final effect of pressure application is the prospect of a structural phase transition to a phase with a different packing fraction and a related change in interface width. These ideas have motivated the work in section 4.2, which details results from measurement of the phonon DOS of nanocrystalline ^{57}Fe with the NRIXS technique (see section 3.4) to pressures up to 28 GPa.

A second path of inquiry rests on the inverse relationship between the phonon frequency ω and the phonon wavelength, λ. Vibrational excitations localized on small features (as has been proposed in the literature) have a maximum wavelength bounded by the size of that feature. By comparing the inelastic neutron scattering from a nanocrystalline solid to a coarse-grained one at extremely low energies, the role of surface vibrations and those localized on similar length scales can be assessed. Nanocrystalline iron was subjected to these measurements for energies from 2 to 18 μeV, the results of which are detailed in section 4.3.

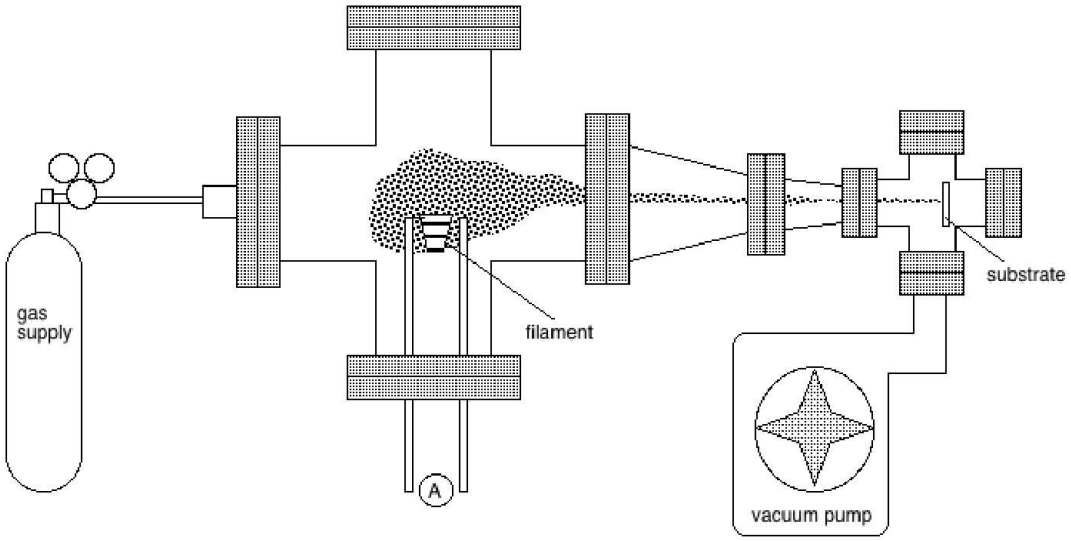

Figure 4.2: Schematic of chamber for ballistic gas consolidation of nanocrystalline metals.

4.2 Phonon Density of States of Nanocrystalline Iron at High Pressure[†]

4.2.1 Experimental

Nanocrystalline ^{57}Fe was prepared by the inert gas consolidation technique [33]. Approximately 30 mg of iron enriched to 95% in the ^{57}Fe isotope were evaporated by resistive heating in a gas stream of N_2 containing 10 vol% H_2 at a pressure of 2 Torr. Iron particles entrained in the gas flow impacted against a glass slide to form a thin film of ^{57}Fe of approximately 3 mg. The sample chamber was then sealed and transferred to an argon atmosphere where the iron film was coated with a thin layer of silicone oil to retard oxidation. A diagram of the sample chamber is shown in figure 4.2.

X-ray diffraction patterns were measured using Co Kα radiation to determine the crystal structure, grain size, and degree of oxidation of the nanocrystalline samples. Scanning and transmission electron microscopy were also performed on natural iron

[†]Originally published in *Phys. Rev. B* 69, 144301 (2004) [50]

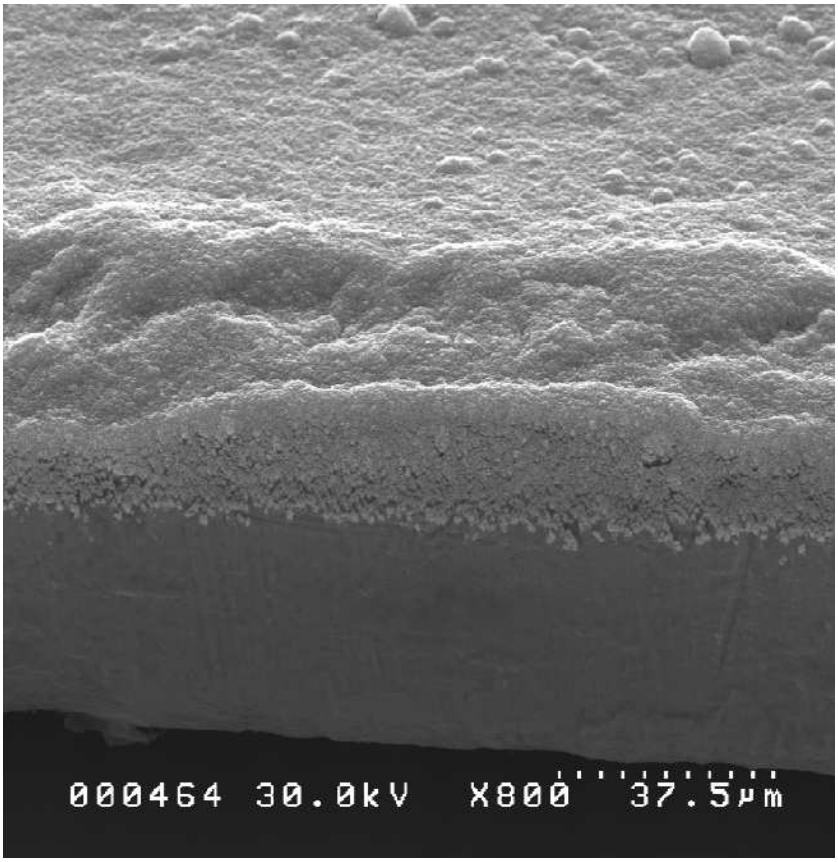

Figure 4.3: SEM micrograph of gas-consolidated nanocrystalline iron on copper sheet.

films deposited under identical conditions to establish morphology and to verify grain size. Representative SEM micrographs of nanocrystalline ^{57}Fe are shown in Figure 4.3, and bright-field/dark-field TEM micrographs are presented in Figure 4.4.

NRIXS was performed at the synchrotron beamline 3-ID of the Advanced Photon Source (APS). The x-ray beam from the undulators was monochromated to a final resolution of 1 meV (FWHM) by a silicon (4 0 0)(10 6 4) monochromator [51] after initial bandpass filtering by a water-cooled (111) diamond. The lineshape delivered by the monochromator was measured by an avalanche photodiode mounted in the forward beam. The tails of this instrument resolution function were negligible at values of ± 5 meV.

Samples of nanocrystalline and polycrystalline bulk ^{57}Fe were loaded into separate piston-cylinder type diamond anvil cells (DAC) optimized for use in NRIXS

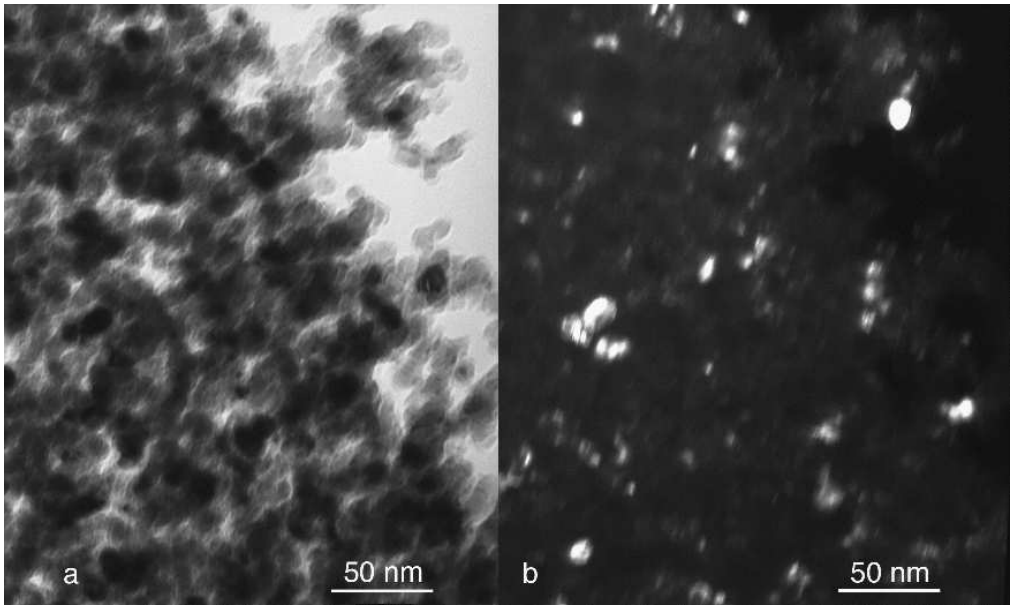

Figure 4.4: TEM **a** brightfield; **b** darkfield images of gas-consolidated iron on holey carbon.

experiments. The specific design of these cells and the experimental configuration are discussed in section 3.5. Diamonds with 500 μm culets were used, and silicone oil [52](Dow Corning DC-705) was employed as a pressure medium. Incoherent inelastic scattering spectra were collected by tuning the incident energy of the x-ray beam from the silicon monochromator in 0.25 meV steps and counting the delayed photons from nuclear de-excitations. Spectra were collected in a range of $\pm$80 meV around the Mössbauer resonance at a rate of one hour per scan. Typically 10 to 12 scans were performed and added together to yield a total incoherent scattering function $S(E)$. The procedure reviewed in section 3.4 was then applied to obtain the phonon DOS [53] of both samples at each pressure. The pressure on the sample was measured before and after each set of scans by the ruby fluorescence technique [15] to confirm pressure stability during the measurement. Synchrotron Mössbauer spectrometry (SMS) time spectra [54] were also measured at each pressure to monitor the crystalline phase of the sample, since the sensitivity of SMS to magnetic order allowed discrimination of the ferromagnetic bcc α phase from the nonmagnetic hcp ϵ phase [55].

4.2.2 Results

X-ray diffraction patterns of the ballistically consolidated films showed a bcc Fe structure with a small amount of oxide. The Scherrer equation for diffraction line broadening yielded an average particle size of 9 nm. Transmission electron microscopy (TEM) performed with a Philips EM420 instrument operated at 120 kV showed distinct individual crystallites and significant porosity, which can also be seen in Figure 4.4. The average grain size seen in dark-field images was consistent with the x-ray results. Films examined with scanning electron microscopy (SEM) had regular, mildly rough surfaces and a uniform morphology (see Figure 4.3) through their entire thickness. Stylus profilometry and SEM measured an average thickness of 20 microns.

The phonon densities of states of both nanocrystalline and coarse-grained ^{57}Fe are presented in Figure 4.5. All have been normalized to unity. The excess intensity in the nanocrystalline DOS below 20 meV is obvious, but quantifying this excess intensity is challenging. Many authors adopt an arbitrary standard; we sought a systematic procedure for identifying this region. At long wavelengths, a three-dimensional solid has a parabolic DOS of the form BE^2, following the well-known work of Debye. This parabola was assumed as a reasonable approximation of the "low-energy" part of the bulk iron DOS measured at ambient pressure. It was divided by the thermal correction factor $E[1 - \exp(-E/kT)]$ and then fit to the inelastic scattering spectrum $S(E)$ of the bulk sample at ambient pressure, using B as the only adjustable parameter. The limits of the fit were adjusted symmetrically until subsequent χ^2 values for the fit approached a constant value. This was taken to delimit the range of applicability of the Debye model for bulk iron, and consequently the appropriate range for discussion. The limit obtained was 12 meV. The results of this fit are shown in Figure 4.6. (Note that the calculated curve is close to a straight line. Fitting a straight line to a range of experimental data helps minimize problems with counting statistics.)

By integrating the DOS curves, we were able to determine the fraction of the modes present in the samples with energies less than 12 meV. The fractions of low-energy modes at each pressure are presented in Figure 4.7. Compared to bulk poly-

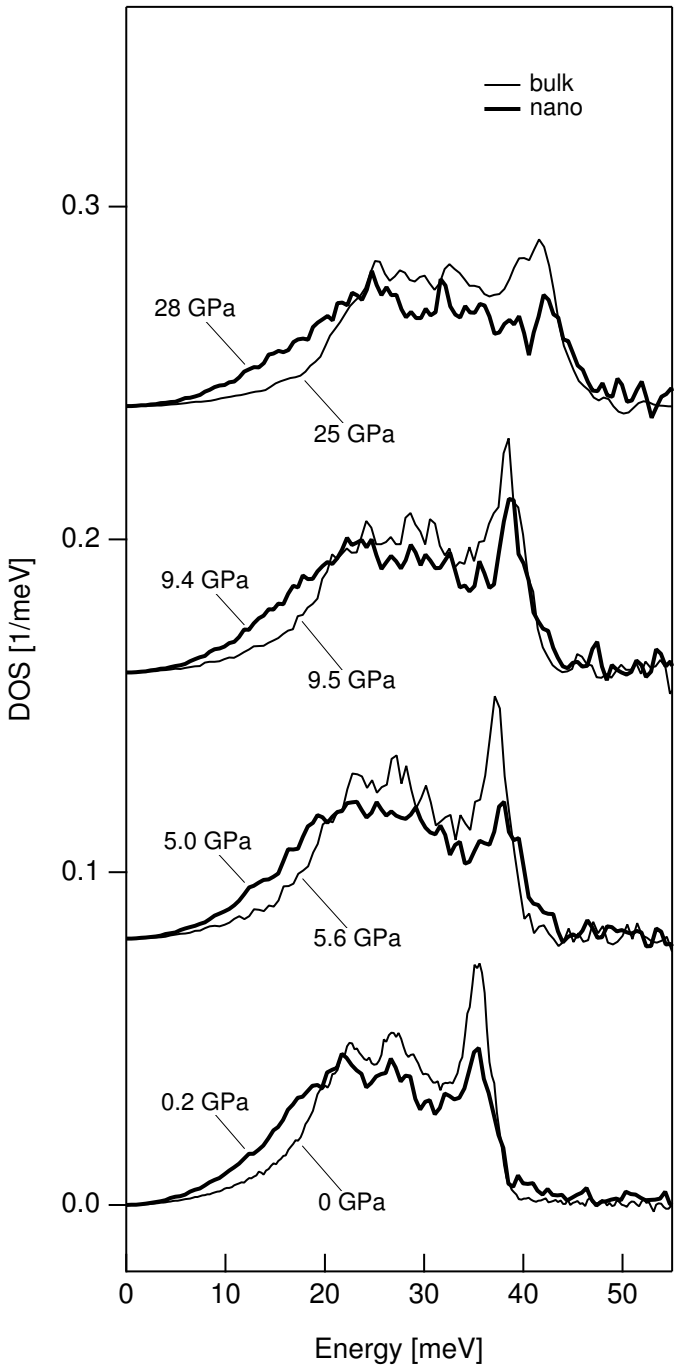

Figure 4.5: Phonon DOS of nanocrystalline (bold line) and coarse-grained (thin line) ^{57}Fe at pressures up to 28 GPa. The upper traces have been shifted vertically by 0.06, 0.12 and 0.18 meV^{-1} with respect to the data at ambient pressure. The samples at 25 and 28 GPa have completely transformed to the hexagonal close-packed phase.

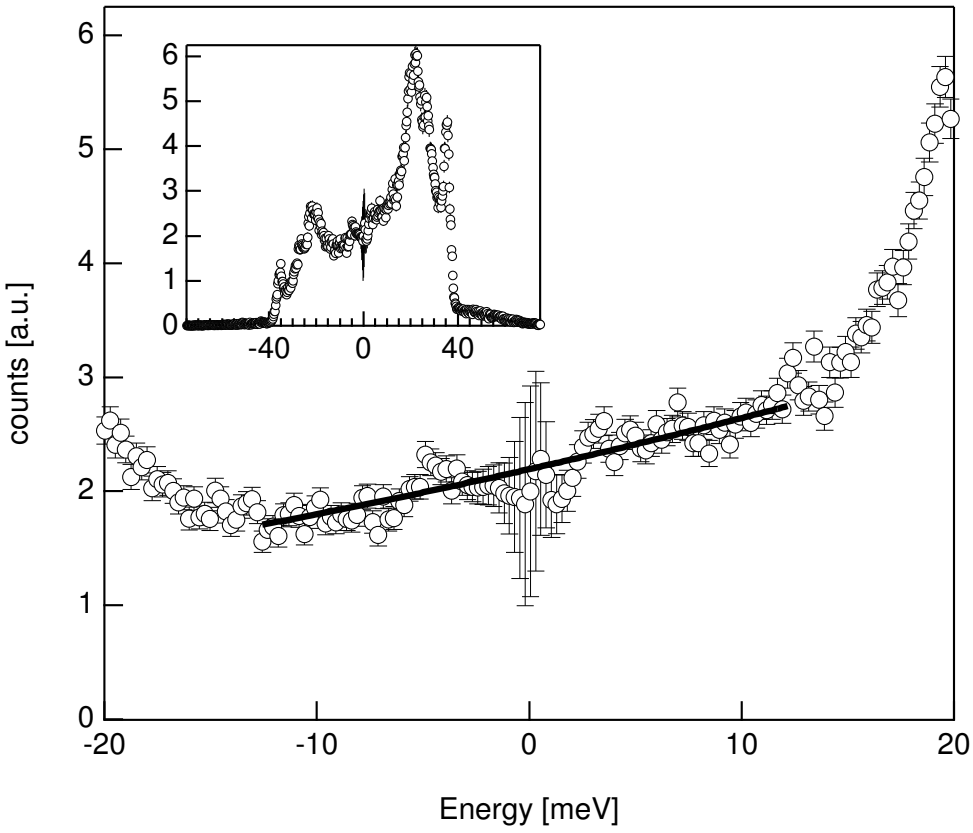

Figure 4.6: Curve fit for determination of the valid range for the Debye model in describing vibrational modes in ^{57}Fe. The function $BE/[1-\exp(-E/kT)]$ was fit to $S(E)$ with B as the only adjustable paramter. The entire energy range is inset.

crystalline iron in the same pressure range, the nanocrystalline sample exhibited a factor of 2.2 more modes in the low-energy region from 0 to 12 meV. This enhancement was approximately independent of pressure or even crystal structure. This ratio decreased to 1.7 after decompression.

As the pressure on the sample is increased, the entire DOS shifts towards higher energies. This can be seen most easily in the movement of the longitudinal peak near the high energy cutoff of the DOS. The pressure-induced phase transition of iron from the bcc to the hcp structure occurs in the region between 9 and 28 GPa, and NFS spectra confirmed that both the nanocrystalline and coarse-grained samples had transformed fully to the hcp phase at the final pressures measured.

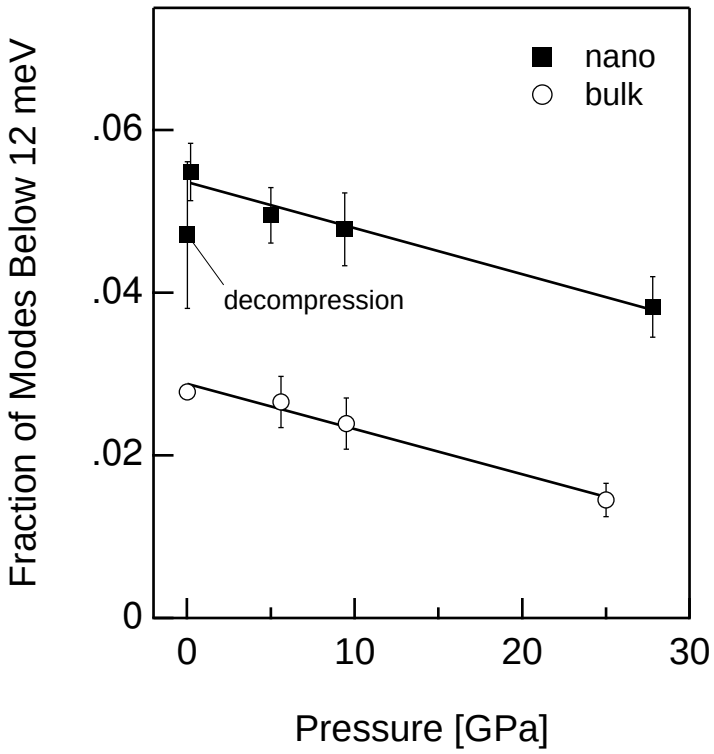

Figure 4.7: The fraction of the vibrational modes with energy less than 12 meV in each sample. The point marked "decompression" was measured subsequent to the decompression of the nanocrystalline sample from 28 GPa.

4.2.3 Discussion

4.2.3.1 High Energy Region

In Figure 4.5, a small enhancement is observable in the DOS of the nanocrystalline sample above the high energy cutoff of the DOS of the bulk sample. This has been adequately explained by the effects of lifetime broadening and the presence of iron oxides [41]. X-ray diffraction measurements on the nanocrystalline sample showed the presence of oxide, which is difficult to prevent completely in nanostructured materials owing to their large surface area. Upon the increase of pressure, the high energy enhancement is decreased, but not eliminated. This behavior is consistent with a constant population of oxide modes and a weakened effect of lifetime energy broadening as the nanoparticles are compressed. Compression brings individual grains in

the nanocrystal into more intimate contact, reducing the strength of elastic discontinuities and decreasing phonon scattering at grain boundaries. The slight sharpening of the longitudinal peak of the nanocrystalline sample at 9 GPa also supports this hypothesis.

Despite the differences observed in the DOS curves, the characteristic van Hove singularities appear at nearly the same energies in both the nanocrystalline and coarse-grained sample and remain in coincidence at all pressures. As zone-edge phenomena, the singularities are attributes of short-wavelength phonons excited in a periodic lattice [56]. The occurrence of these features at the same energies in both microstructures shows that a high grain boundary volume fraction does not distort significantly the vibrational modes inside crystalline regions. The commensurate tracking of the singularities with pressure is evidence that high grain boundary density has little effect on the interatomic potentials for iron atoms within crystalline environments.

4.2.3.2 Low Energy Region

The most obvious difference in the DOS curves of the nanocrystalline and the bulk sample at low energies is the number of modes, as all of the curves are essentially featureless to energies of ~ 20 meV. Figure 4.7 shows that the fractional enhancement in low-energy modes in nanocrystals remains essentially constant under pressure, even across the $\alpha \rightarrow \epsilon$ structural phase transition. These results imply that to a large degree, the fraction of grain boundaries, and not their particular structure, is a general source of the enhancement in the low-energy part of the spectrum. This assertion is reinforced by the observation of abundant low-energy modes in nanocrystals with fcc [37] and bcc [40] structures and those produced by ball milling [32].

When the nanocrystalline sample was decompressed from its ultimate pressure, Figure 4.7 shows that not all of the modes below 12 meV were recovered. This is possibly due to the structural change to the hcp phase at $\sim$12 GPa and back to the bcc phase on decompression. We expect a smaller fraction of the atoms at grain

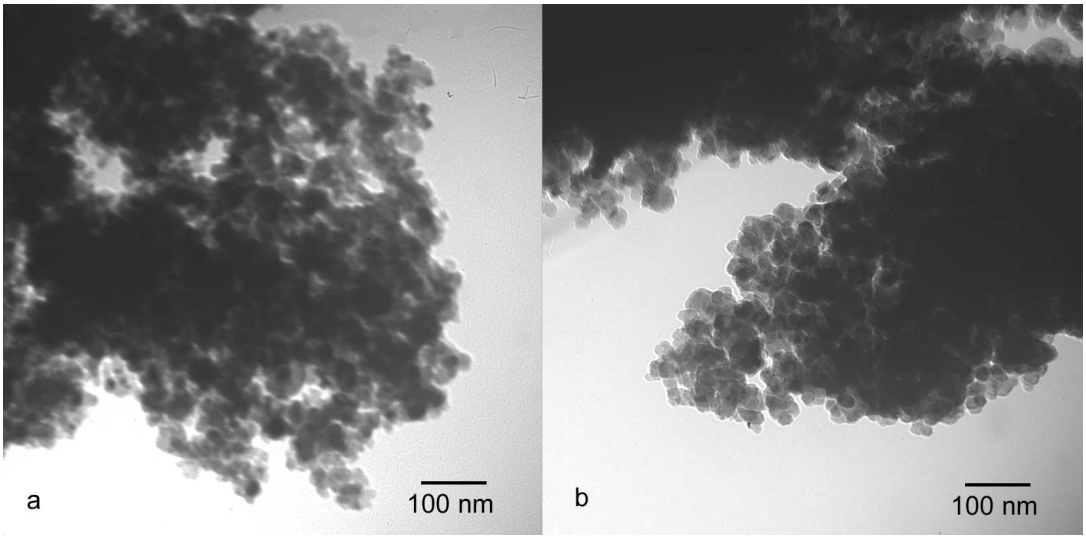

Figure 4.8: TEM micrograph of Gas-consolidated iron **a** before; **b** after compression to 16 GPa in a diamond anvil cell.

boundaries of a close-packed phase, and this effect may be hysteretic. TEM performed on gas-consolidated nanocrystalline ^{57}Fe that had been compressed to 16 GPa and subsequently decompressed is shown in Figure 4.8. The figure shows little change in the shapes and sizes of individual grains, which eliminates the possibility of a lowered fraction of surface area. However, the TEM results do not rule out some densification of grain boundary regions, which have widths on the order of 1 nm.

It is clear from the pressure dependence of the fraction of low energy modes below 12 meV that vibrations associated with the internal surfaces of voids in the nanocrystalline aggregate are not a significant factor in the enhancement of the low frequency DOS. The TEM (see Fig. 4.4) and SEM (Fig. 4.3) micrographs above show the evidence of pores in the gas-consolidated sample. Positron lifetime measurements on 6 nm diameter Fe nanoparticles [57] synthesized by gas consolidation exhibited spectral components with nanosecond order lifetimes, which the authors associated with positronium formation in void interiors. Compression of the samples to 4.5 GPa reduced the intensity of this component significantly. At a pressure of 28 GPa, significantly more compaction is expected. The constant deficit in modes shown in Figure 4.7 is only consistent with this behavior if void surfaces do not contribute

appreciably to the phonon DOS.

4.2.3.3 Spatial Dimension of Low-Energy Modes

The work by van Hove [56] showed that for low frequencies, the phonon DOS should be proportional to E^{d-1}, where d is the dimensionality of the system. The relevant dimensionality remains an unsettled issue for nanostructured materials.

It is incorrect to assume that the total DOS can be decomposed into a "grain boundary" partial DOS and a "grain interior" partial DOS. Especially problematic are systems in which the crystallite size approaches the grain boundary width. With a sound velocity of 3500 m/sec, a 10 meV phonon has a wavelength of 1.5 nm. In a spherical nanocrystal of 9 nm diameter, 70% of the atoms in the crystal are within this 1.5 nm distance of the grain boundary, and this fraction is even larger for crystals with anisotropic shapes. The dynamics of grain boundaries and crystal interiors are therefore coupled closely in a nanocrystalline material. A three-dimensional dynamics may therefore be expected in spite of the large fraction of internal surface in the nanostructure.

The primary support for assertions of reduced dimensionality in nanocrystals is based on several computational studies [47, 58, 59, 60], but few experimental investigations [48, 46]. Reference [46] details inelastic neutron scattering measurements from grain-boundary segregated H in nanocrystalline Pd. Experimental evidence for a linear contribution to the spectrum rested on the assumption that the projection on H atoms of the low-energy modes is the same as the projection on neighboring Pd atoms [46]. This is not justified when motions of adjacent Pd atoms are out-of-phase, for example.

The low-energy regions of our measured DOS curves were fit to a power law of the form AE^n, and the results presented in Figure 4.9. Averaging over all data, the value of n is found to be (2.02 ± 0.025) for the bulk control samples and (1.98 ± 0.015) for the nanocrystalline material. Both are nearly equal to the value of 2 for three-dimensional vibrational dynamics. The exponent for the data from the

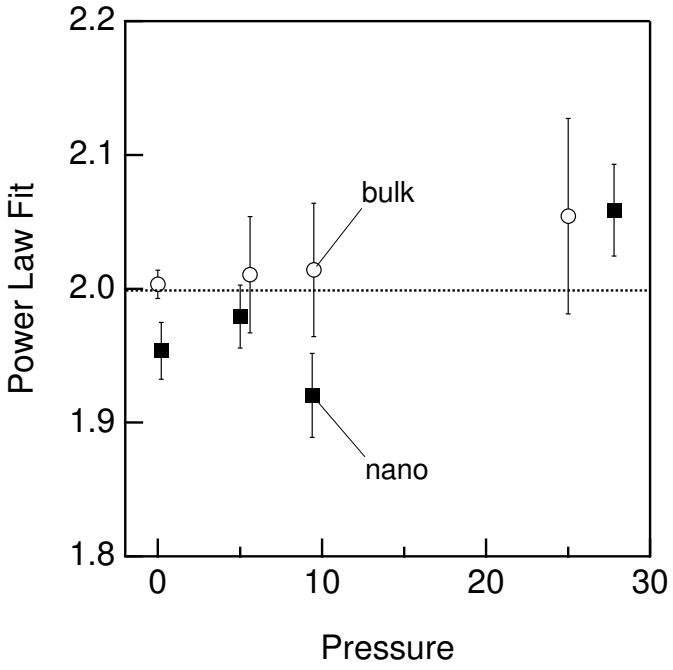

Figure 4.9: Results of fitting a power law to the phonon DOS curves up to 12 meV.

nanocrystalline bcc α phase alone is (1.95 $\pm$ 0.015), admitting a possible small effect of lower dimensionality. Pressure has little effect on the exponent n, which is not surprising, since n is so close to 2 at ambient pressure.

4.2.4 Conclusions

NRIXS measurements of the phonon DOS of gas-consolidated iron nanocrystals established a constant enhancement of the DOS below 12 meV to a pressure of 28 GPa. Once decompressed, the nanocrystalline sample exhibited fewer excess low-frequency modes which may be indicative of structural hysteresis in the grain boundaries. The pressure dependence of the force constants of the nanocrystalline sample was identical to the control sample, as judged by the fraction of modes below 12 meV and the position of the van Hove singularities throughout the pressure range. Finally, mesoscopic defects, namely internal voids, have been shown to have no effect on the overall phonon DOS in nanocrystalline metals.

4.3 Enhancement of Phonon Modes in Nanocrystalline Iron at Micro-eV Energies[†]

4.3.1 Experimental

Nanocrystalline iron powders were synthesized by mechanical attrition in a Union Process 01-HD mixer/mill by Nanomat, Inc. Approximately 100 g of Fe powder of 99.9% purity were placed in hardened steel vials with steel balls in an argon atmosphere, and were milled for 36 hours with a ball-to-powder weight ratio of 20:1. Ball milling produces nanocrystalline microstructures by the creation of dislocation networks which coalesce into high-angle grain boundaries upon further milling [62]. A control sample was produced by annealing the nanocrystalline powder at 550 °C.

Prompt-gamma activation analyses of hydrogen concentrations were performed at the NIST Center for Neutron Research on both nanocrystalline and control samples. The sample of nanocrystalline Fe contained 0.19 ± 0.02 at% hydrogen, similar to the control sample concentration of 0.16 ± 0.02 at%.

Inelastic neutron scattering experiments were performed at the high-flux backscattering spectrometer (HFBS) [63] located at the NIST Center for Neutron Research in Gaithersburg, Maryland. The instrument was operated with an energy resolution of 0.95 μeV (as measured with a vanadium standard) and a dynamic range of ± 18 μeV, both determined by a Si (1 1 1) monochromator mounted on a Doppler drive. The final energy of the scattered neutrons was fixed at 2.08 meV. The detector array provided access to 16 Q values from 0.25 to 1.75 Å^{-1}. The nanocrystalline and control samples, each massing approximately 20 g, were placed in thin-walled annular aluminum cans for the measurement. Measurements were made at both room temperature and 10 K with the use of a closed-cycle refrigerator.

Room temperature data were acquired over the course of seven measurements spanning two hours, for a total collection time of 14 hours. Spectra acquired at 10

[†]Originally published in *Phys. Rev. Lett.* 93, 205501 (2004) [61]

K were assembled from five two-hour measurements. Multiple measurements were performed and summed due to the sequential energy selection of the HFBS Doppler monochromator [63] (hardware or software faults in long measurements would result in the acquisition of only partial spectra). The difference in collection time combined with the expected depression in phonon scattering at low temperatures accounts for the difference in overall intensity of the datasets.

The spectra were corrected by subtracting the scattering from the empty aluminum can and for the mass of the samples. A multiphonon correction was not applied, since this phenomenon is insignificant at low values of Q. The data sets were reduced with the DAVE [64] software, available from the NIST Center for Neutron Research.

Inelastic neutron scattering measurements in the meV range were also performed on the same samples with the PHAROS time-of-flight spectrometer instrument at the Los Alamos Neutron Science Center at Los Alamos National Laboratory. The data were normalized by the masses of the samples and were corrected for multiphonon scattering by an iterative procedure described elsewhere [65].

4.3.2 Results

X-ray diffraction data from the as-milled and control samples were analyzed by the ΔQ vs Q method. The average grain size was 10 nm for the as-milled sample and 35 nm for the annealed sample.

The total scattering function $S(E)$ acquired from the HFBS instrument can be seen in figure 4.10. As mentioned in section 4.3.1, this is virtually equivalent to $S_1(E)$ in the μeV regime. The one-phonon scattering is proportional to the phonon DOS and is given by

$$D(E) \propto E\ [1 - exp(-E/kT)]S(E) \tag{4.3.1}$$

The reduction in scattering at 10 K is a simple fact of a reduced phonon population as determined by the Bose-Einstein distribution.

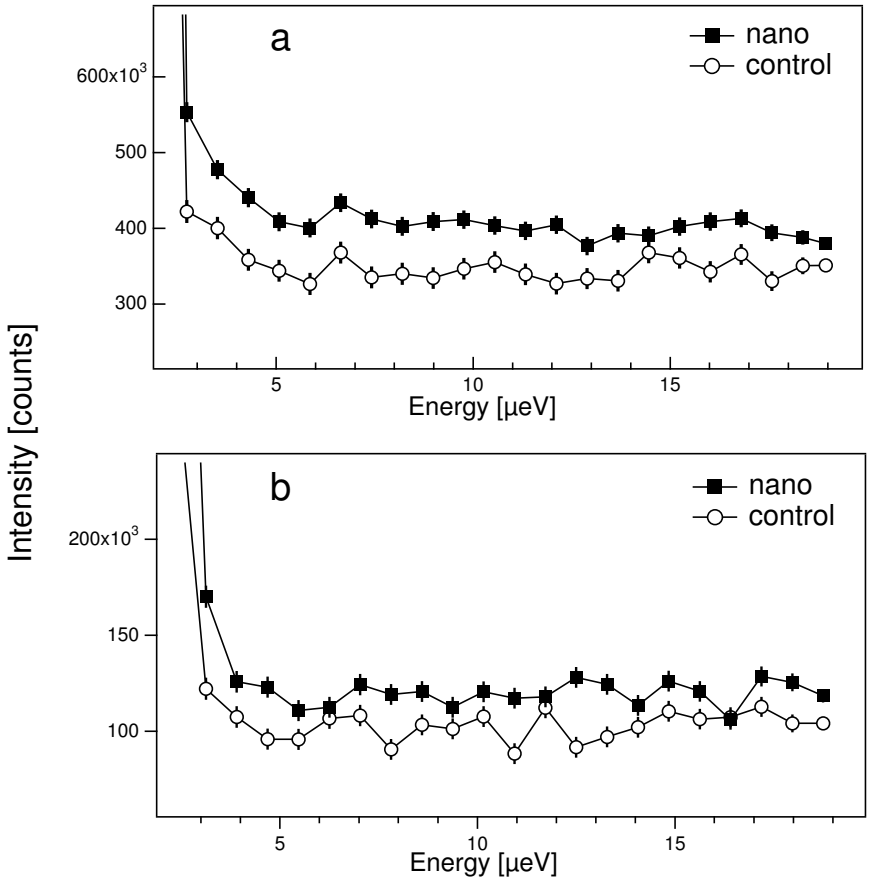

Figure 4.10: Momentum integrated inelastic scattering from nanocrystalline (nano) and coarse-grained (control) iron from the High Flux Backscattering Spectrometer at **a** 293 K; and **b** 10 K.

The momentum integrated single phonon scattering function $S_1(E)$ from the PHAROS spectrometer is shown in figure 4.11.

Over the range from 2 to 18 μeV, the nanocrystalline sample exhibited an enhancement in scattering intensity by a factor of 1.2 ± 0.05 compared to the control sample. Similar analysis of the PHAROS data from 4 to 50 meV yielded an enhancement factor of 1.3 ± 0.05.

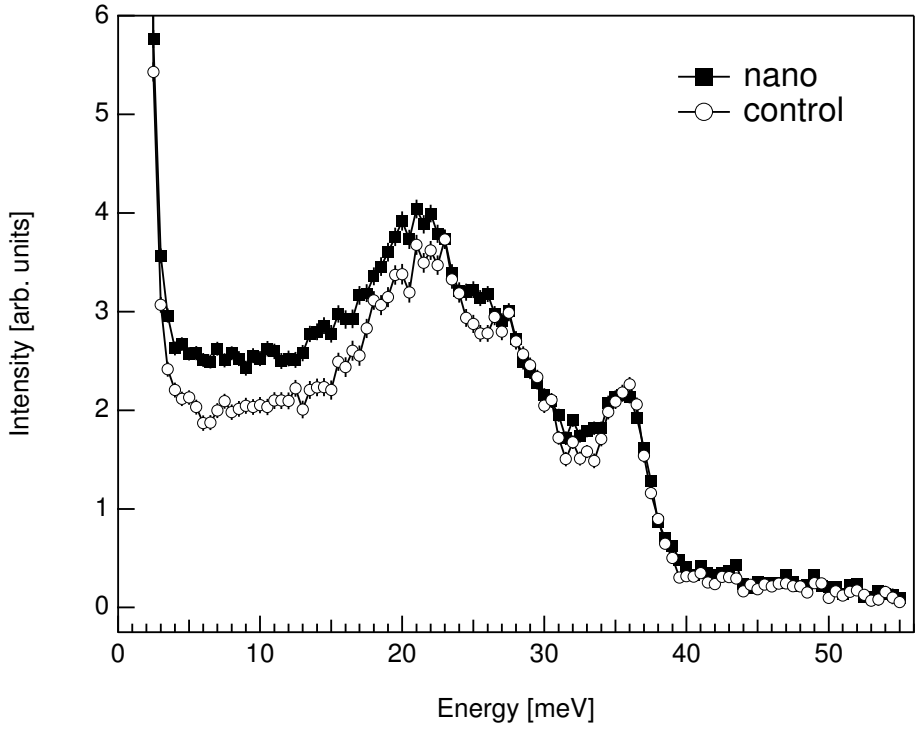

Figure 4.11: Momentum integrated single-phonon inelastic neutron scattering function $S_1(E)$ of nanocrystalline (nano) and coarse-grained (control) iron. Acquired with the PHAROS time-of-flight spectrometer at LANSCE, Los Alamos National Laboratory.

4.3.3 Discussion

Excitations localized on small-scale features (within a single particle, or on its surface) must have a low-energy cutoff that corresponds to the size of the feature. A dispersionless vibrational mode has a low energy cutoff given by $E_L = 2\pi\hbar c/\lambda_L$, with c the sound velocity and λ_L the size of the particle. For a crystallite size of 10 nm and a Debye sound velocity of 3000 m/s, the lowest excitation energy an isolated nanoparticle can support is in the vicinity of 1 meV. Vibrations with micro-eV energies must be extended over multiple crystallites.

In the absence of surface modes, cooperative dynamics of many nanocrystallites may be a source of the enhancement in $S(E)$ between 2 and 18 μeV. These modes can be characterized as (large) independent crystallite masses coupled by forces at grain boundaries. However, it is difficult to envision this phenomenon accounting wholly

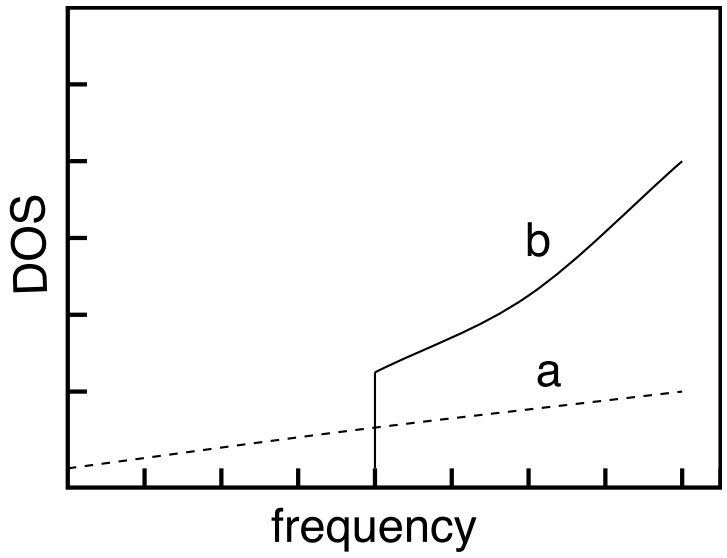

Figure 4.12: The frequency dependence of the DOS of **a** "microstructural" modes; **b** modes confined to a single nanocrystal. Modes of type **b** have a cutoff frequency ω_c which depends on the crystal size. Microstructural modes extend throughout the crystal and have no cutoff.

for the observed anomalies. A cube-shaped Fe nanocrystal with 10 nm sides will contain approximately 10^5 atoms and 3×10^5 vibrational modes. An array of N of these rigid cubes would have $3N$ "microstructural" modes, but 3×10^5 N conventional modes. Unexpectedly weak forces between grains may allow for this high density of microstructural modes at micro-eV energies. This hypothesis is supported by the scaling of the $S(E)$ enhancement at micro-eV energies with decreasing grain size described in [61]. Samples of Ni_3Fe with 6 nm grains exhibited an increase of 40% compared to a 20% effect for the 12 nm iron nanocrystals.

The relatively greater enhancement of the inelastic scattering in the meV range (Figure 4.11) is a function of the cutoff frequency for localized excitations. In the meV range, we must still allow for surface modes, though Figure 4.9 shows little evidence for vibrations incommensurate with three-dimensional dynamics. A model DOS with a long wavelength cutoff at frequency ω_c is shown schematically in Figure 4.12.

4.4 Conclusions

Inelastic neutron scattering measurements on nanocrystalline ball-milled iron in both the μeV and meV range established enhancements of the DOS compared to a large-grained control sample. The enhancement was relatively larger at meV energies, however, indicative of a cutoff wavelength for some sources of the anomalies. Excess modes up to 20 μeV are partly the result of microstructural modes, which involve the concerted motion of many crystallites against each other.

4.5 Future Work

The problem of low-energy vibrations in nanocrystalline materials has eluded a simple explanation for some time. The high degree of disorder in nanocrystalline environments presents challenges for experiments, calculations, and the interpretation of the results.

Perhaps the definitive experimental measurement of grain-boundary dynamics in nanocrystals would be conducted with the NRIXS technique. If we recall the review in chapter 3, NRIXS provides us with the *partial* phonon DOS of the resonant species (here, ^{57}Fe) given by

$$D^{Fe}(E) = \left\langle \sum_j \left|\sigma_j^{Fe}(\mathbf{q})\right|^2 \delta(E - E_j) \right\rangle \tag{4.5.1}$$

where σ_j^{Fe} is the polarization vector of an ^{57}Fe atom for the jth vibrational mode. The average $\langle\rangle$ is over all ^{57}Fe atoms.

If it were possible to segregate ^{57}Fe at the grain boundaries of a non-resonant nanocrystalline aggregate, the partial DOS of the iron atoms would be a grain boundary partial DOS. A schematic representation of this structural arrangement is shown in Figure 4.13 below.

There are several alloy systems that may be viable candidates for such an ex-

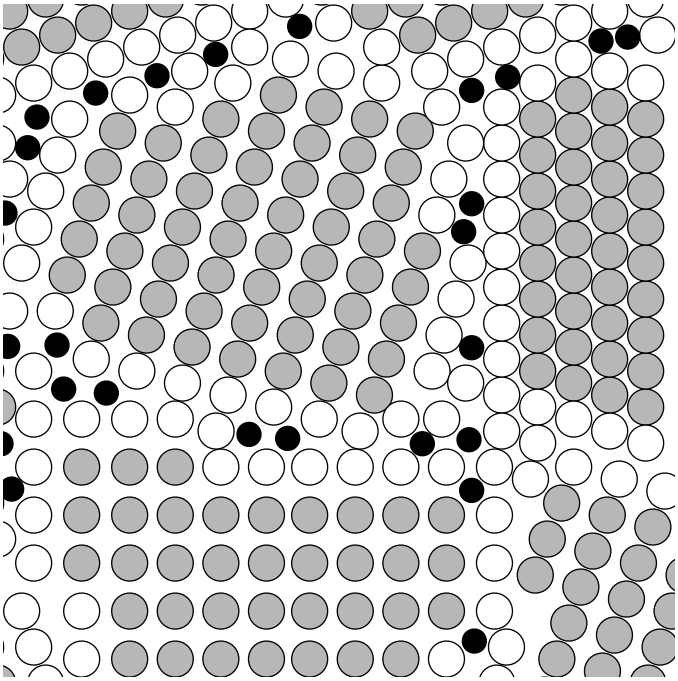

Figure 4.13: A schematic of resonant ^{57}Fe atoms (black) segregated at the grain boundaries (white) of a nanocrystalline phase of a non-resonant species (gray).

periment, but each is fraught with imposing experimental challenges. From a thermodynamic standpoint, ensuring ^{57}Fe migration to grain boundaries is difficult; the high temperatures needed to induce diffusion are also conducive to grain growth and the destruction of the nanocrystalline structure. The second key issue relies on the verification of the positions of the resonant atoms.

The systems which appear most promising at this time are the hexagonal close-packed third and fourth column elements Ti, Zr, and Y. Iron is an interstitial impurity in these systems, leading to some volume dilatation of the elemental unit cell. Iron migration to disordered environments and out of the crystal cell could be observed by conventional x-ray diffraction measurements.

Some investigators have demonstrated limited success in grain boundary segregation of Fe in nanocrystalline Y produced by inert gas consolidation [66, 67]. Unfortunately, yttrium is highly reactive, and nanocrystalline yttrium produced by gas consolidation burns quickly upon exposure to air. Attempts have been made to passivate the exposed surface of Y-Fe consolidated films by evaporating thin films of Al

metal on top of the nanoparticles, but Fe-doped Y_2O_3 nevertheless resulted. It is possible that a UHV environment followed by some passivation procedure would be necessary to properly ensure metallic Y with Fe inclusions.

Iron has also been shown to diffuse to surfaces and grain boundaries in Zr at temperatures of approximately 600° C [68]. Attempts to produce Zr-based nanocrystals with inert gas consolidation were unsuccessful, due to the high melting point and low vapor pressure of Zr (2125 K and 1.26×10^{-5} torr at 1852° C, respectively). Other physical vapor deposition methods such as evaporation or pulsed-laser deposition may be viable means of forming Zr-based nanocrystals.

Chapter 5

Density Functional Theory and High-Pressure Investigations

Density functional theory (DFT) is so profoundly useful due to the generality of its precepts. It is a true *ab initio* method which requires no parameters other than the crystal lattice and basis for the solid under investigation.

Computational approaches are often crucial to a balanced understanding of high-pressure experiments. The strenuous limits imposed by the DAC defeat many common techniques, and DFT is often able to bridge the conceptual gulf that is left.

5.1 Essential Aspects of DFT

Under the Born-Oppenheimer approximation, we are permitted to treat separately the electron potential due to the nuclei and due to the electrons themselves. Let the potential due to the nuclei be $\hat{V}_{ext}$; all electron-electron interactions (classical Coulomb potential, exchange-correlation potential) we denote $\hat{V}$. With these assumptions, the many-body Hamiltonian is:

$$\hat{H} = \hat{T} + \hat{V} + \hat{V}_{ext} \tag{5.1.1}$$

with $\hat{T}$ the electron kinetic energy operator.

The core of density functional theory is owed to Hohenberg and Kohn [69], who showed that the external potential $\hat{V}_{ext}$ exhibits a one-to-one correspondence with the

ground state electron density, ρ. It is intuitive to students of quantum mechanics that V_{ext} determines ρ; density functional theory exists because the converse is also true. The consequences of that statement are far reaching, because given the external potential V_{ext}, the Hamiltonian H itself is uniquely determined. That is, the Hamiltonian, and thus the ground state total energy, is a *functional* of the ground state electron density. The ground state energy of the system may then be expressed (with the notation $f[x]$ indicating that f is a functional of x):

$$E_{V_{ext}}[\rho] = \langle\Psi|\hat{T} + \hat{V}|\Psi\rangle + \langle\Psi|\hat{V_{ext}}|\Psi\rangle \tag{5.1.2}$$

$$= F_{HK}[\rho] + \int \rho(\vec{r}\,)V_{ext}(\vec{r}\,)d\vec{r} \tag{5.1.3}$$

where F_{HK} is the Hohenberg-Kohn functional. Of course, the form of F_{HK} is not known explicitly. DFT is made a practical tool by the Kohn-Sham (KS) equations [70]. By further decomposing the Hohenberg-Kohn functional, the KS equations allow the energy functional to be written:

$$E_{V_{ext}}[\rho] = T_0[\rho] + V_{ext}[\rho] + V_{Coul}[\rho] + V_{xc}[\rho] \tag{5.1.4}$$

where T_0 is the kinetic energy functional for a *non-interacting* electron gas, V_{Coul} is the classical Coulomb potential, and V_{xc} is the (unknown) exchange-correlation functional. Couched in this way, the ground state energy of the inhomogenous interacting electron gas can be obtained by solving the wave equation for a single-particle Hamiltonian. That is, there exists a set of single-particle wavefunctions such that

$$\hat{H}_{KS}\phi_i = \epsilon_i\phi_i \tag{5.1.5}$$

where $\hat{H}_{KS}$ is the KS Hamiltonian, and the *exact* ground state electron density of the

N-electron system is given by

$$\rho(\vec{r}\,) = \sum_{i}^{N} \phi_i(\vec{r}\,)^* \phi_i(\vec{r}\,) \tag{5.1.6}$$

The set of $\{\phi_i\}$ does not represent actual electron wavefunctions here, nor are the $\{\epsilon_i\}$ single-electron energies; rather they are the eigenfunctions and eigenvalues, respectively, of the Kohn-Sham Hamiltonian.

5.2 Exchange-Correlation Potentials

The Kohn-Sham equations are not useful without explicit definition of an exchange-correlation functional $V_{xc}[\rho]$. The accuracy and precision of DFT calculations are influenced greatly by the functional that is chosen. A brief introduction to the varieties of approximation follows.

5.2.1 The Local Density Approximation (LDA)

This functional operates under the assumption that the inhomogenous electron gas can be divided into differential elements of constant density, and that these elements contribute to the exchange-correlation energy identically to a homogenous electron gas of that density. That is,

$$V_{xc}^{LDA}[\rho] = \int \rho(\vec{r}\,)\epsilon_{xc}\left(\rho(\vec{r}\,)\right) d\vec{r} \tag{5.2.1}$$

where $\epsilon_{xc}\left(\rho(\vec{r}\,)\right)$ is a function which is known numerically for the homogeneous electron gas. It can be extended to spin-polarized systems by separately accounting for spin-up and spin-down densities, in which case it is referred to as the local *spin* density approximation (LSDA):

$$V_{xc}^{LSDA}[\rho_\uparrow, \rho_\downarrow] = \int \rho(\vec{r}\,)\epsilon_{xc}\left(\rho_\uparrow(\vec{r}\,), \rho_\downarrow(\vec{r}\,)\right) d\vec{r} \tag{5.2.2}$$

The LDA and LSDA functionals have been shown to be successful in systems with slowly varying density. However, a notable failure of the LSDA functionals was exposed by results which found the nonmagnetic and antiferromagnetic fcc phases of iron to be more stable than the ferromagnetic bcc phase [71]. This inadequacy, along with others, prompted the development of functionals which accounted for neighboring density elements, i.e., density gradients.

5.2.2 The Generalized Gradient Approximation (GGA)

Many forms of GGA functionals exist, since the incorporation of the density gradient term is not explicitly stipulated (as opposed to the LDA, where ϵ_{xc} is well-defined). The functional in the GGA scheme takes the form

$$V_{xc}^{GGA}[\rho_\uparrow, \rho_\downarrow] = \int f\left(\rho_\uparrow(\vec{r}\,), \rho_\downarrow(\vec{r}\,), \nabla\rho_\uparrow(\vec{r}\,), \nabla\rho_\downarrow(\vec{r}\,)\right) d\vec{r} \tag{5.2.3}$$

where f is not uniquely defined. In comparison with LSDA, GGA functionals more accurately determine total energies and structural energy differences, as well as softening and expanding bonds [72]. Care must also be taken in applying GGA, because there are cases where the LDA solutions are overcorrected, leading to underbinding. Examples of this can be seen in noble gas dimers and N_2 molecular crystals, for which GGA predicts no binding [73].

5.3 Solving the Kohn-Sham Equations

What has been ignored above is that the electron density is an unknown in addition to the eigenfunctions of the KS Hamiltonian. In fact, the density depends on the solutions ϕ_m according to equation (5.1.6). This is then a self-consistency problem, in which the solution determines the equation to be solved. An initial guess of the density is made, and the KS equations are solved, after which the density is recomputed with the $\{\phi_m\}$. This density is used to repeat the cycle until the density arrived at

converges on the input density.

The process of solving the self-consistent KS equations is essentially reduced to finding the correct coefficients to express the single-particle wavefunctions in terms of the chosen basis.

$$\hat{H}_{KS}\phi_m(\vec{r}\,) = \epsilon_m\phi_m(\vec{r}\,) \tag{5.3.1}$$

$$\phi_m = \sum_{p=1}^{P} c_p\phi_p^b \tag{5.3.2}$$

where the basis functions $\{\phi_p^b\}$ may be any orthonormal set. Plane waves are employed in some capacity in most popular codes applied to condensed matter, due to obvious connections with Bloch's theorem. In the interstitial regions between nuclei, valence electrons tend to behave similarly to free electrons, making the plane wave basis an efficient choice. It is in the electronic core, where the wave function may be both steep and oscillatory, that the choice of basis varies most.

5.4 Basis Functions for DFT

Basis sets, similarly to exchange-correlation functionals, are an area of current development in DFT. An exhaustive catalogue of basis sets, and the theory behind them is beyond the scope of this thesis. Instead, what follows is an outline of the fundamental principles which are shared among basis sets currently in use.

5.4.1 Pseudopotential Methods

For many applications of *ab initio* codes, core electron energies and excitations are unimportant. This is true for many systems in which chemical bonding is of primary interest, or in simulations of lattice vibrations, to give two examples. The pseudopotential (PP) in question is the combined interaction potential of the nuclear attraction mediated by the electronic screening of the core.

The key advantage of the PP method is the computing efficiency it offers. By

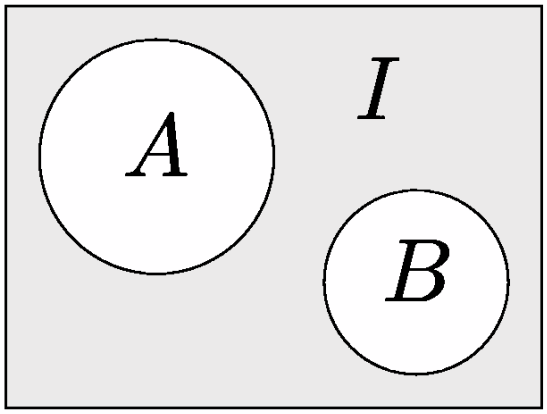

Figure 5.1: Schematic representation of the muffin-tin scheme for full-potential plane wave bases. A and B represent atomic spheres for inequivalent atoms, and the shaded area I is the interstitial region.

truncating the plane wave basis at a k value insufficient to accurately describe the potential near the nucleus, few plane waves are needed. Its disadvantages, of course, are the lack of insight provided into the behavior of the core electrons. For the subject of this thesis, in which core spin polarization and high pressures (which may cause core relaxation) are vitally important, pseudopotential codes do not suffice.

5.4.2 Full-Potential Plane Wave Methods

The steep potential near the nucleus is no small impediment to the use of a pure plane-wave basis in the absence of a psuedopotential. So-called full-potential methods cope with this through the adoption of a combined basis set predicated on the subdivision of the unit cell into multiple atomic spheres and an interstitial region. Physical intuition suggests that even in solids, electrons close to the nucleus have wavefunctions which are atomic in nature; similarly electrons far from the nucleus move in a much weaker potential and are more or less free. This scheme is illustrated in Figure 5.1. In the region I in Figure 5.1, the plane waves take a familiar form:

$$\phi_{\vec{K}}^{\vec{k}}(\vec{r}\,) = \frac{1}{\sqrt{V}} e^{i(\vec{k}+\vec{K})\cdot\vec{r}} \tag{5.4.1}$$

where $\vec{k}$ is a wavevector in the Brillouin zone, $\vec{K}$ is a reciprocal lattice vector, and V is the volume of the unit cell. Within the muffin-tin sphere, however, there are several choices that can be made. The WIEN2K code, which was used for the work presented in this thesis, offers combined linearized augmented plane wave (LAPW) plus local orbital (LO) and augmented plane wave (APW) plus LO bases.

As their names would suggest, the LAPW+LO and APW+LO method share some salient features. In the interstitial region, plane waves of the form given in equation (5.4.1) are the basis functions. Within the atomic sphere, the APW basis function has the form:

$$\phi^{\vec{k}}_{\vec{K}}(\vec{r}, E) = \sum_{l,m} A^{\vec{K}+\vec{k}}_{lm} u_l(r, E_l) Y^l_m(\hat{r}\ ) \tag{5.4.2}$$

here, the u_l are solutions to the radial part of the Schrödinger equation for a free atom, and Y^l_m are the spherical harmonics. The A_{lm} are determined to enforce continuity with the plane waves at all points on the surface of the atomic sphere. To cope with the problem of accurately determining the parameter E, (to wit, the eigenenergy of the searched eigenstate), *local orbitals* (LO) are added to the basis. These orbitals have zero value in the interstital region, but within the atomic sphere α have the form:

$$\phi^{lm}_{\alpha}(\vec{r}\ ) = \left(A^{\alpha}_{lm} u^{\alpha}_l(r, E_l) + B^{\alpha}_{lm} \dot{u}^{\alpha}_l(r, E_l)\right) Y^l_m(\hat{r}\ ) \tag{5.4.3}$$

A^{α}_{lm} and B^{α}_{lm} are required for normalization and enforcement of zero value for the LO at the muffin-tin boundary. The $\dot{u}^{\alpha}_l(r, E_l)$ is the energy derivative of the radial function described above.

The LAPW+LO method differs from APW+LO in the use of the radial functions within the atomic sphere. The difficulty of using a basis function which depends on a value of E that is yet to be determined is ameliorated by linearizing $u^{\alpha}_l(r, E_l)$ by means of a Taylor expansion. As before, the LAPW has the form of equation (5.4.1) in the interstitial region. Within the muffin tin, the expansion of u^{α}_l is done about

E_0:

$$u_l^\alpha(r,E) = u_l^\alpha(r,E_0) + (E_0 - E)\ \dot{u}_l^\alpha(r,E_0) + \ldots \tag{5.4.4}$$

Again, the notation $\dot{u}$ indicates the first energy derivative. The muffin-tin form of the LAPW is then

$$\phi_{\vec{K}}^{\vec{k}}(\vec{r},E) = \sum_{l,m}\left(A_{lm}^{\vec{K}+\vec{k}}u_l(r,E_0) + B_{lm}^{\vec{K}+\vec{k}}\dot{u}_l(r,E_0)\right)Y_m^l(\hat{r}\ ) \tag{5.4.5}$$

and similarly to the APW+LO method, $A_{lm}^{\vec{K}+\vec{k}}$ and $B_{lm}^{\vec{K}+\vec{k}}$ are found to enforce the necessary continuity conditions at the boundary of the atomic sphere.

Local orbitals in LAPW+LO are similar to those discussed for APW+LO above, with the addition of a second linearized u_l^α at the energy E_2. The addition of a second parameter permits the treatment of wavefunctions of different character but the same l value, such as those in the so-called *semi-core* region.

5.5 DFT and Equations of State

One of the great uses for DFT in the study of high pressures can be found in the thermodynamic relationship between the internal energy and pressure. If the internal energy is parameterized by entropy and volume (and the conjugate variables pressure and temperature), it is elementary to write:

$$dE = TdS - PdV \tag{5.5.1}$$

and partial differentiation with respect to V gives us

$$P = -\left(\frac{\partial E}{\partial V}\right)_S \tag{5.5.2}$$

DFT very simply allows E to be obtained at multiple values of V, the unit cell volume. In the context of high pressures, this allows the introduction of isothermal

equations of state (EOS). With an adequate number of $E(V)$ points, fitting the data to an EOS provides at the very least the theoretical bulk modulus and zero-pressure volume. Moreover, the mapping of energy to pressure is essential when comparing the stability of two phases under pressure. The Murnaghan equation [74], though seldom used today, illustrates the simple relations between pressure, volume, and energy:

$$P = \frac{K_0}{K_0'}\left[\left(\frac{V_0}{V}\right)^{K_0'} - 1\right] \tag{5.5.3}$$

Here, K_0 is the zero-pressure bulk modulus, K_0' is its pressure derivative, and V_0 is the zero pressure volume. Simple integration is sufficient to connect this EOS to our DFT results.

$$E = \int \frac{K_0}{K_0'}\left[\left(\frac{V_0}{V}\right)^{K_0'} - 1\right] dV \tag{5.5.4}$$

$$E = V\frac{K_0}{K_0'}\left[\frac{1}{K_0' - 1}\left(\frac{V_0}{V}\right)^{K_0'} + 1\right] + E_0 \tag{5.5.5}$$

E_0 here is the zero-pressure internal energy.

It should be noted that this and other equations of state are necessarily isothermal, or when applied to DFT results, athermal.

5.6 Computing HMF with DFT

The hyperfine magnetic field was introduced in chapter 3 for a single electron. In a solid, with the help of the language of DFT, the contact field can be defined using the *spin density* at the nucleus, $M(0)$:

$$M(0) = [\rho_\uparrow(0) - \rho_\downarrow(0)] \tag{5.6.1}$$

the expression for the contact field becomes:

$$\mathbf{H}_{eff} = \frac{8\pi}{3}\mu_B M(0) \tag{5.6.2}$$

Another modification that must be made to our model is the inclusion of relativistic effects. Core level electrons may possess mean-square velocities that are an appreciable fraction of the speed of light. As a rule of thumb, an electron in a $1s$ orbital has mean-square velocity Z a.u. ($c = 137$ a.u.) [75]. Relativity tends to contract core orbitals due the increase of the electron effective mass in these states. The effects of relativity are extremely important for the calculation of hyperfine fields, generated close to the nuclei where relativistic effects are most pronounced. The contact field may be corrected by averaging the spin density over a sphere with a diameter given by the Thomson radius $r_T = \frac{Ze^2}{mc^2}$ [76], which is much larger than the size of the nucleus. The expression for the contact field becomes:

$$\mathbf{H}_{eff} = \frac{8\pi}{3}\mu_B \int_0^\infty \left[\rho_\uparrow(r) - \rho_\downarrow(r)\right] \delta_T(r) dr \tag{5.6.3}$$

$$\delta_T(r) = \frac{1}{4\pi r^2} \frac{r_T/2}{(r + r_T/2)^2} \tag{5.6.4}$$

5.7 Conclusions and Further Reading

As understanding of condensed matter at high pressures grows, the systems explored under these conditions have become increasingly complex. Computational tools have been indispensable in providing more complete understanding of the mechanisms of high-pressure property shifts. Moreover, of all the extant tools, DFT may be the most powerful.

The theory and practice of density functional theory are far richer than can be conveyed in this thesis. Many excellent works have been published on the subject, allowing any sufficiently interested party access to the utility of DFT. An extensive introduction to DFT, including discussions of basis sets, is provided in reference [77]. Another helpful work is reference [75].

Chapter 6

Antiferromagnetism in HCP Iron

6.1 Introduction

The high-pressure, hexagonal close-packed (ϵ) phase of iron has been a subject of intense experimental and computational interest since its discovery in 1956 [78]. This attention may be partly attributed to the fact that ϵ phase iron and its alloys are thought to comprise a large fraction of the earth's core. However, in addition to the obvious efforts pertaining to the elastic and seismic properties of ϵ-iron, an equally extensive body of work has been accumulated regarding the magnetic ground state of the phase.

Early Mössbauer effect measurements on hcp iron [79] observed a single absorption line rather than the six-line pattern characteristic of ferromagnetic bcc iron (see Figure 3.3.3) at temperatures as low as 30 mK [80]. These results were interpreted as evidence of an absence of magnetic order in the ϵ phase. Later measurements at 4.5 K and under applied fields up to 7 T [81] similarly detected only small hyperfine fields which increased linearly with applied field, again implying paramagnetism.

Despite these direct experimental results, the possibility of antiferromagnetic ordering in hcp iron was suggested by Mössbauer and neutron diffraction measurements on coherent precipitates of fcc Fe in Cu [82] as well as Mössbauer measurements on hexagonal Fe-based alloys dilute in Mn [83], and Ru and Os [84, 85]. Based on these results, Wohlfarth postulated that ϵ-Fe may be superconducting at low tempera-

tures [86]. Recently, Shimizu et al. [87] have shown this to be true for temperatures lower than 2 K.

The discovery of superconductivity in hcp iron has spurred new interest in the magnetic behavior of the phase [88], especially in light of recent work on the ferromagnetic superconductors $ZrZn_2$ [89] and UGe_2 [90]. The presence of magnetism was determined to be a prerequisite for superconductivity in these materials, prompting a reexamination of magnetism in ϵ-Fe. Key entries in this discussion have been furnished by Steinle-Neumann, Cohen, et al. via DFT calculations [6, 91, 92]. These investigators identified a static antiferromagnetic structure for hcp iron (hereafter referred to as the *afmII* structure) which exhibits a fortuitous cancellation of a large core electron polarization by an equally large itinerant electron polarization, resulting in a net HMF of nearly zero. This hypothesis very neatly explains the null results of the Mössbauer measurements, but sustains the possibility of antiferromagnetism in ϵ-iron. The *afmII* spin structure is depicted in schematic in Figure 6.1.

This chapter describes a test of the idea that ϵ-iron is antiferromagnetic, yet exhibits no hyperfine field owing to the negligible net spin density at its nuclei. If indeed such a fine balance between core and conduction electron polarization exists, it is expected that localized magnetic perturbations would disrupt it, producing measurable hyperfine magnetic fields. Local perturbations can be introduced by alloying; HMF shifts at ^{57}Fe atoms caused by neighboring solute atoms have been studied for many years by Mössbauer [93, 7, 94, 95] and NMR spectrometry [96, 97] measurements on Fe-rich bcc alloys.

A particularly attractive impurity in this context is nickel. Nickel solutes have been shown to increase magnetic moments at neighboring Fe atoms, leading to a concomitant increase in core electron polarizations [94, 95]. The altered magnetic moment at the solute site also causes a redistribution of spin density of the conduction electrons. The resultant hyperfine magnetic fields at iron atoms with nickel neighbors in these alloys exhibit shifts of tens of kG with respect to pure iron. Mössbauer spectroscopy techniques are able to resolve HMF values of approximately 10 kG, and

smaller effects can be detected from the broadening of spectral lines. section 6.2 below addresses the systematics of hyperfine magnetic field effects due to magnetic impurities in iron. The remainder of this chapter is concerned with the extension of these principles to the ϵ-Fe system with a combined computational and experimental approach.

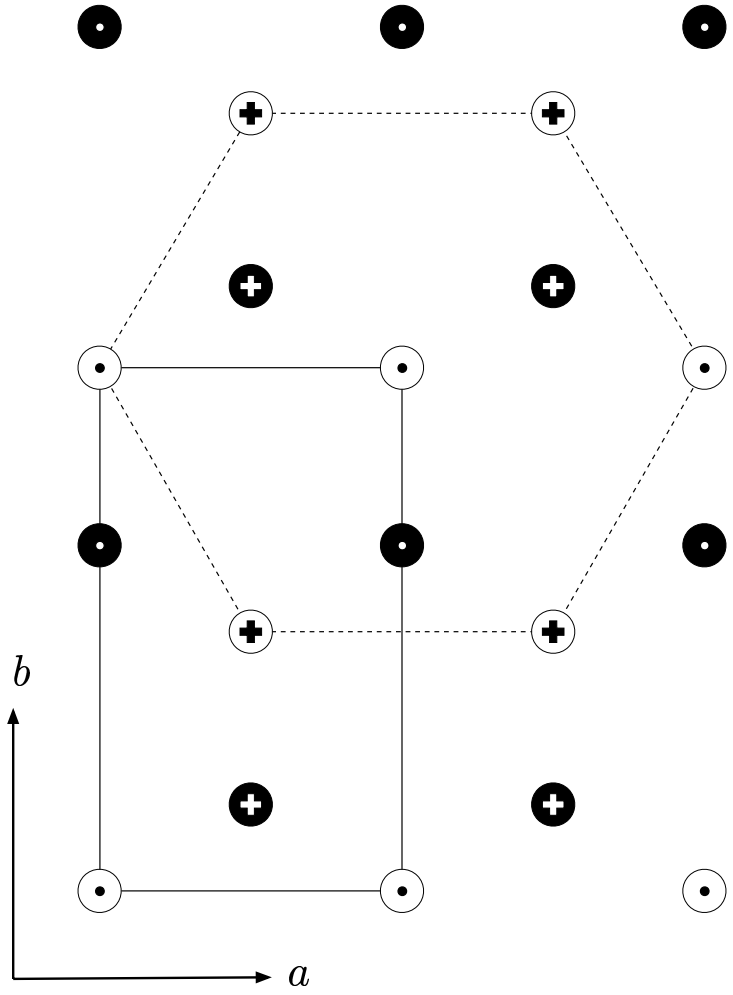

Figure 6.1: The spin structure for the *afmII* structure in pure hexagonal iron. The unit cell is orthorhombic (*Pmma* space group) and is shown in solid black lines. Dotted lines indicate the hexagonal cell for reference. Black circles represent atoms at z=$\frac{1}{4}$ and white circles are atoms at z=$\frac{3}{4}$. Crosses indicate spin down and dots indicate spin up. Adapted from [6].

6.2 Hyperfine Field Perturbations in Iron

As discussed in chapter 3, the hyperfine magnetic field results from the sum of several contributions. These contributions may be written, in order of decreasing magnitude,

$$H_{tot} = H_{core} + H_{cond} + H_{orb} + H_{mag} + H_{dip} \tag{6.2.1}$$

Here the Fermi contact term has been broken into two separate terms, H_{core} and H_{cond}, which refer to the field from the spin polarization of the core and conduction electrons, respectively. In bcc iron, the total HMF is –330 kG;* the largest portion of this field is due to the contact interaction.

In this thesis I will restrict my concern to the changes that are induced in the various HMF components by alloying and the relative magnitude of those changes. Here my aim is not to provide an exhaustive treatment of the mechanisms of ^{57}Fe HMF perturbations due to impurities, but rather to account more specifically for the relevant mechanisms for a magnetic impurity (Ni) in iron. A complete discussion of the relevant interactions for many binary and ternary iron alloys can be found in [98].

In the dilute limit, the classical terms H_{orb}, H_{mag}, and H_{dip} are largely unaffected by the addition of solute atoms. The orbital term H_{orb} derives particularly from electrons local to a given atom and as such is minimally impacted by alloying. Impurities do break the cubic symmetry of the bcc lattice and allow the existence of a magnetic dipole moment, though H_{dip} remains negligible in comparison to the contact term and is averaged out in a random solution. The lattice magnetization H_{mag} is also generally insensitive to alloying in the dilute case, and moreover in a polycrystal, averages to zero in the absence of an applied field.

In contrast to the effects of alloying on the classical magnetic interactions, solutes can significantly alter H_{core} and H_{cond}. From the definition of the contact interaction in equation (5.6.2), we see that it is the *spatial distribution* of electron spins about

*The negative sign reflects that the spin density at the nucleus, and thus the HMF, has the sense of the *minority* spins and is oriented oppositely to the lattice magnetization. See text for details.

the nucleus that is important in determining the hyperfine field. This is a subtle, yet critical point, as even in the relativistic case, only the spin-paired s electrons have significant density at the nucleus. In magnetic systems, the symmetry of spin-up and spin-down s wavefunctions is broken by exchange coupling to the unpaired magnetic d electrons. In the Hartree-Fock formalism, the exchange energy for a many-electron system [99] is given by

$$E_{xc} = -\frac{1}{2}\sum_{i\neq j}\int \psi_i^*(\vec{r}_i)\psi_j^*(\vec{r}_j)\frac{e^2}{|\vec{r}_i - \vec{r}_j|}\psi_i(\vec{r}_j)\psi_j(\vec{r}_i)\; d\vec{r}_i\; d\vec{r}_j \tag{6.2.2}$$

for each pair of electrons i and j of the same spin. The energy E_{xc} is a correction to the Coulomb repulsion term that is applied only to electrons of like spin. In that sense, it may be thought of as an attractive potential. The exchange interaction is responsible for band magnetism itself, as the energetic benefit of filling spin-up bands preferentially outstrips the kinetic energy penalty of doing so. Similarly, it is exchange coupling between d and s electrons that explains the negative sign of the native α-Fe hyperfine field. Core s electrons are concentrated closer to the nucleus than the unpaired $3d$ electrons, which exert an attractive force on the $s\uparrow$ electrons. This results in a hyperfine magnetic field generated by a net spin-down density at the nucleus. The hyperfine field is thus oppositely oriented to the lattice magnetization.

Our concern, then, is the specific manner by which s electron wavefunctions are redistributed about ^{57}Fe atoms in the vicinity of a solute atom. It has been shown that the contact field due to core polarization exhibits a linear response to the magnetic moment of the ^{57}Fe sites [94], which for iron is primarily due to the unpaired $3d$ electrons. When Ni is added to bcc Fe, the excess d electrons it contributes are added to the magnetic d band and increase the magnetic moment of neighboring Fe atoms. These augmented local moments pull core $s\uparrow$ electrons further from the nucleus, enhancing the disparity of $s\downarrow$ electrons and increasing the magnitude of the ^{57}Fe HMF.

The effect of the impurity on the conduction $4s$ electrons due to the moment local

to the Fe site can be understood with similar reasoning. The $4s$ electron density tends to be concentrated further from the nucleus than the more closely bound $3d$ electrons, and so the effect of more unpaired $d\uparrow$ electrons is to draw the $4s\uparrow$ electrons closer to the nucleus, for a net positive (parallel to the lattice magnetization) contribution to the ^{57}Fe HMF.

A secondary effect of Ni solvation that must be taken into account is the substitution of an iron magnetic moment by a nickel moment in the lattice. Itinerant electrons are more significantly influenced by exchange coupling to moments at neighboring atoms than closely bound core electrons, which are primarily affected by the local moment. An impurity site with a smaller local moment than the Fe atom for which it is substituted (as is the case with Ni) exerts a lesser exchange coupling to the itinerant $4s\uparrow$ electrons, for a net lowering of the conduction electron polarization at the ^{57}Fe site. However, since Ni retains a moment of almost half that of Fe in solution and the first bcc coordination shell contains 8 atoms, the overall effect due to the moment substitution is small. Impurities such as Si that do not contribute unpaired d electrons to the Fe d-band and that have no magnetic moment do influence the HMF significantly through this mechanism [93].

Empirical relations have been developed to parameterize the HMF contributions from individual solute atoms in the nearest neighbor shells of a ^{57}Fe atom. The underpinning assumption of these rules is that of a dilute solution, for which the additivity of individual HMF changes holds. The common expression is given by:

$$H^{tot}(\{n_j\}) = H_0 + \sum_{j=1}^{J} n_j \; \Delta H_j^X \tag{6.2.3}$$

where the number of atoms in nearest neighbor shell j is n_j and the effect on the total HMF from a single inpurity of type X in the j^{th} shell is ΔH_j^X. For nickel solutes in bcc iron, $\Delta H_1^{Ni} = -7$ kG and $\Delta H_2^{Ni} = -7$ kG [98]. The negative values for the ΔH_j^X indicate that Ni impurities increase the magnitude of the hyperfine magnetic field in α-Fe.

6.3 Experiment and Results

6.3.1 DFT Calculations on Ni Impurities in BCC Fe

While very little is known about the effects of magnetic solutes in ϵ-Fe, the systematics in α-Fe are well established. To evaluate the accuracy of DFT in computing hyperfine fields in magnetic substitutional alloys, calculations were performed for a supercell comprised of 54 atoms, based on a $3 \times 3 \times 3$ repetition of the bcc unit cell. The Fe atom at the origin of the coordinate system was replaced with an Ni atom, for a total composition of $Fe_{53}Ni$.

The WIEN2K software package [100] was used with a combined LAPW/APW+LO basis set and the GGA exchange-correlation potential of Perdew, *et al.* [72]. The experimental Fe lattice parameter of 2.869 Å was adopted for the primitive unit of the supercell, for a total lattice parameter of 8.606 Å. A muffin-tin radius R_{MT} of 2.2 bohr (1.164 Å) was chosen for both Fe and Ni atomic spheres, and the product $R_{MT}K_{max}$ was set to 8.0. The $1s$, $2s$, $2p$, and $3s$ orbitals were treated as core states, and the $4s$, $3p$, and $3d$ orbitals were taken to be the valence states. The LAPW basis was employed except for $3p$, $3d$, and $4s$ states, for which the APW+LO basis was chosen. An additional local orbital was also adopted for the $3p$ states. Using a $12 \times 12 \times 12$ special k-point mesh yielded 1728 total k-points and 56 k-points in the irreducible wedge of the first Brillouin zone. All calculations were performed with spin polarization, meaning that the densities of spin-up and spin-down electrons were calculated separately.

Initially the positions of the atoms in the supercell were relaxed using the built-in PORT option, a reverse-communication trust-region Quasi-Newton method from the Fortran PORT library [101]. A force convergence tolerance of 1.0 mRy/bohr was applied to self-consistency, after which forces in the supercell were lower than 1.3 mRy/bohr. Subsequently the calculations were again iterated to self-consistency with the optimal lattice coordinates and converged to 0.04 mRy and a charge distance[†]

[†]The charge distance for the n^{th} iteration is defined as $\int |\rho_n - \rho_{n-1}|\, dr$.

Table 6.1: Hyperfine magnetic fields and magnetic moments at ^{57}Fe in pure bcc Fe and in a bcc $Fe_{53}Ni_1$ supercell

Atom	B_{val} [kG]	B_{core} [kG]	B_{tot} [kG]	μ [μ_B]
pure Fe	-44	-287	-331	2.2
Fe 1nn	-5	-311	-316	2.49
Fe 2nn	-20	-288	-308	2.32
Fe 3nn	-32	-287	-319	2.31
Fe 4nn	-25	-289	-314	2.32
Fe 5nn	-32	-290	-322	2.33

of 1×10^{-5} electrons. The hyperfine magnetic fields and magnetic moments from this computation are presented in Table 6.1, along with the accepted computational results for α-Fe. Mössbauer effect experiments are unable to separate the respective core and conduction polarization contributions to the hyperfine field; however, the accepted value for the total hyperfine field in α-Fe is indeed –330 kG, and it is accepted that the majority of the HMF originates from B_{core}.

The calculated HMF results for $Fe_{53}Ni_1$ do not agree with the experimental parameters given in section 6.2. Referenced to pure α-Fe only iron atoms in the first nearest neighbor shell of the impurity nickel atom exhibit a significantly perturbed B_{core}. Moreover, it appears that the exchange effect of nickel on nearby conduction electrons is overestimated relative to effects on the core electrons, which results in a globally lower absolute value of B_{tot}. The iron local moment is appreciably increased at the each iron site; this renders the higher values of B_{tot} all the more surprising.

6.3.2 DFT Calculations on Antiferromagnetic HCP Fe-Ni

A calculational supercell was constructed based on the *afmII* ϵ-Fe structure (see Figure 6.1) based on a $2 \times 2 \times 1$ repetition of the *afmII* ϵ-Fe unit cell [6]. Due to the inequivalence of the spin-up and spin-down atoms, the crystal system of the *afmII* structure is othorhombic, with space group *Pmma*. To preserve the *Pmma* symmetry, Ni atoms replaced Fe atoms at fractional coordinates $(\frac{1}{12}, \frac{1}{2}, \frac{3}{4})$ and $(\frac{11}{12}, \frac{1}{2}, \frac{1}{4})$ in the 16 atom supercell for a net composition of Fe_7Ni_1. This structure is shown in

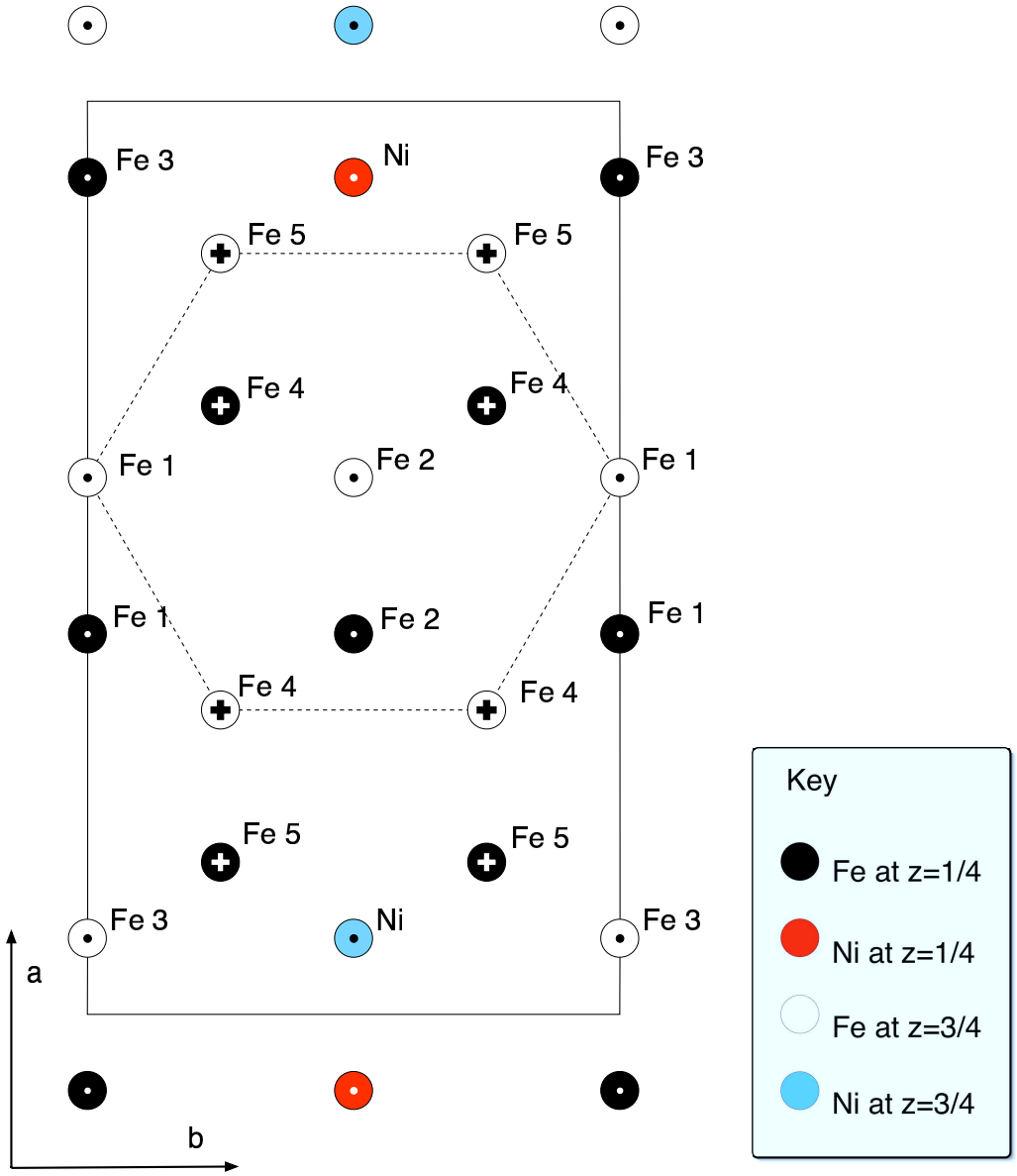

Figure 6.2: The Fe_7Ni_1 supercell with the *afmII* spin structure. Crosses denote a spin orientation pointing into the page, while circles indicate spin pointing out of the page.

schematic in Figure 6.2. WIEN2K calculations were again initialized with the combined LAPW/APW+LO basis and the GGA functional of Perdew *et al.* Initial lattice parameters for the supercell were scaled from extrapolated zero-pressure experimental values for ϵ-Fe; the c/a ratio of the unit cell was fixed at 1.6, the experimentally derived value [102]. R_{MT} was set to 2.0 bohr for both Fe and Ni, and $R_{MT}K_{max}$ was

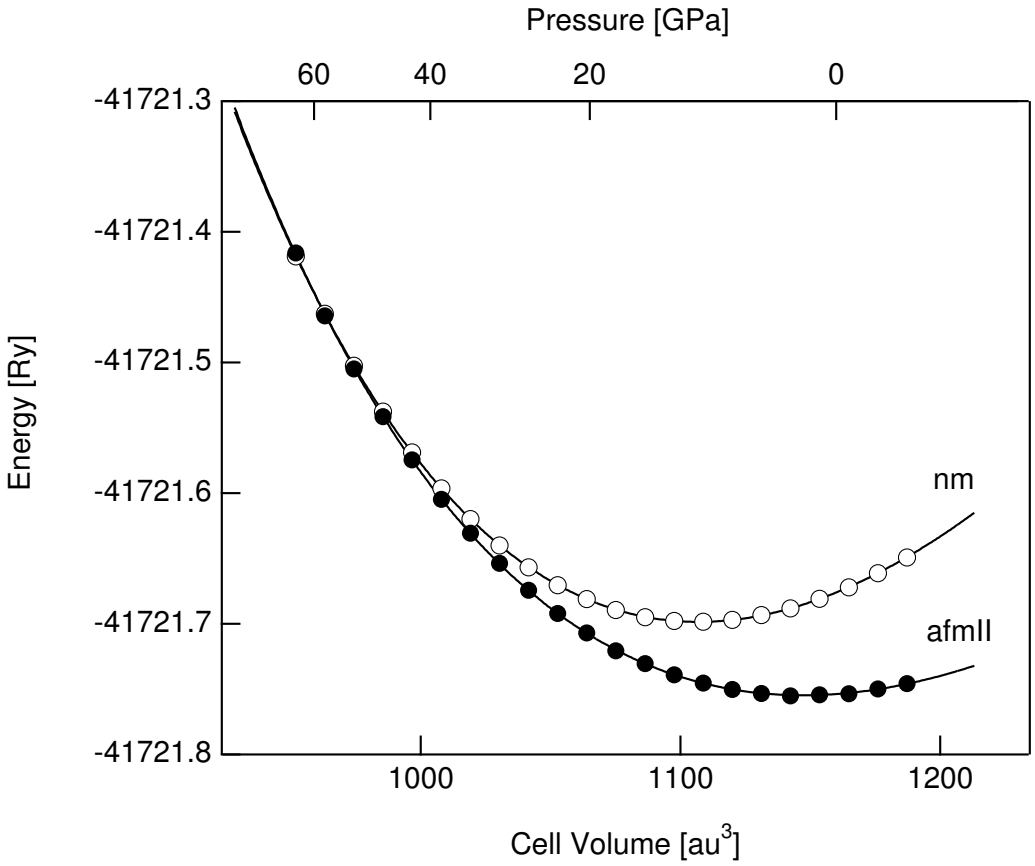

Figure 6.3: Total energy as a function of volume for the *afmII* structure and the corresponding nonmagnetic case. Solid lines are fits to the second order Birch-Murnaghan equation of state. The pressure scale on the upper axis applies only to the *afmII* curve, as the two structures have different bulk moduli.

set to 8.0. Calculations with a $R_{MT}K_{max}$ value of 9.0 returned similar HMF results and an energy difference of less than 2 ppm at a volume of 70 bohr^3/atom. Given the negligible disparity $R_{MT}K_{max} = 8.0$ was deemed sufficiently accurate. Core and valence orbitals were defined identically to the α-Fe case above. The special k-point mesh was of dimensions $11 \times 8 \times 5$ with a resultant 500 total k-points and 72 k-points in the irreducible wedge of the Brillouin zone.

Nuclear positions in the unit cell were relaxed separately for the spin-polarized case and the nonmagnetic case with the PORT method, yielding forces less than 2.5 mRy/bohr. Spin-polarized total energy calculations were performed for the *afmII*

Table 6.2: HMF at ^{57}Fe in ϵ-phase *afmII* Fe_7Ni_1[a] and ϵ-phase *afmII* Fe[b]

Atom	B_{val} [kG]	B_{core} [kG]	B_{tot} [kG]
pure Fe	89	-85	4
Fe 1 in Fe_7Ni_1	133	-108	25
Fe 2 in Fe_7Ni_1	117	-107	10
Fe 3 in Fe_7Ni_1	130	-91	39
Fe 4 in Fe_7Ni_1	-85	109	24
Fe 5 in Fe_7Ni_1	-102	168	66

[a] ϵ-phase *afmII* Fe_7Ni_1 at primitive cell volume 66.06 au^3
[b] ϵ-phase *afmII* Fe at primitive cell volume 65 au^3

structure and converged to 0.01 mRy in energy and a charge distance of 1×10^{-4}. Unpolarized calculations were also converged for the nonmagnetic structure to similar criteria. Total energies were computed for a range of cell volumes and the resulting energy-volume curves fitted to the second order Birch-Murnaghan equation of state [74]. A comparison of the total energy of the antiferromagnetic state compared to the nonmagnetic state as function of cell volume is shown in Figure 6.3.

The calculations on the *Pmma* Fe_7Ni_1 supercell showed that the *afmII* structure is more stable than its nonmagnetic counterpart up to a pressure of nearly 50 GPa at 0 K. The total energy difference between the two states at their zero-pressure volumes was 3.51 mRy per atom, and the difference was 2.8 mRy at 20 GPa. Hyperfine magnetic field values were calculated for the antiferromagnetic structure and are tabulated in Table 6.2 for comparison to the calculated values for pure ϵ-Fe.

The trends in B_{core} and B_{cond} which are seen in section 6.3.1 for a bcc Fe-Ni alloy continue for the hcp phase. Lattice sites with the spin-up local moment (Fe1, Fe2, Fe3) exhibit a considerable positive change in valence polarization and a negative change in core polarization. For the lattice sites with the minority local moment (spin-down), the effect is reversed, but the overall HMF change has the same sign as for the spin-up sites. This reversal of sign is a simple consequence of the inverted local moment at the spin-down sites Fe4 and Fe5 in the antiferromagnetic structure. No parameters ΔH_j^{Ni} (see section 6.2) are known for ϵ-Fe; the only comparison available

is a direct experimental measurement of the alloy HMF.

6.3.3 Sample Preparation

For comparison to the computational results, an alloy of nominal composition $Fe_{92}Ni_8$ was made by arc-melting iron of 99.99% purity and nickel of 99.98% purity in an argon atmosphere. No mass loss was detected, and electron microprobe measurements established an actual composition of $Fe_{0.929}Ni_{0.071}$. Approximately 20 percent of the mass of the iron in the sample was composed of the ^{57}Fe isotope. The resulting ingot was then rolled to a thickness of 50 μm. Cu Kα x-ray diffraction from the rolled foil indicated a uniform bcc structure with (2 0 0) texture and a lattice parameter almost identical to that of pure bcc iron.

6.3.4 High Pressure X-ray Diffraction

High pressure energy dispersive x-ray diffraction (EDXRD) was performed[‡] at beamline X-17C of the National Synchrotron Light Source to identify the pressure of the $\alpha \rightarrow \epsilon$ phase transition. A liquid nitrogen-cooled Ge detector was positioned at a fixed $2\theta = 11.996^\circ$ to measure the diffracted intensity. The sample was loaded in a Merrill-Bassett DAC of the TAU design [103] with diamonds having 500 μm culets, silicone oil as the pressure medium, and 301 stainless steel as a gasket material. EDXRD patterns were recorded in the range from 0 to 24 GPa. The ruby fluorescence technique was used for pressure determination. The diffraction patterns established that the $\alpha \rightarrow \epsilon$ phase transition occurred at approximately 10 GPa, and no bcc diffraction peaks were detected at pressures higher than 14 GPa. Selected EDXRD patterns are shown in Figure 6.4. The α phase (1 1 0) peak is clearly visible at 9.5 GPa, but disappears at 10.1 GPa and coincides with the appearance of the ϵ (1 0 0) and (1 0 1) peaks. The ϵ (2 0 0) peak is weak and is a result of texturing in the sample loaded in the DAC.

[‡]Measurements conducted by I. Halevy.

6.3.5 Synchrotron Mössbauer Spectrometry

Synchrotron Mössbauer spectrometry (SMS) experiments were performed at beamline 16 ID-D of HPCAT at the Advanced Photon Source. A symmetric piston-cylinder type diamond anvil cell was employed with diamonds of 500 μm culet diameter, a rhenium gasket, and silicone oil pressure medium. Subsequent to the application of 20.8 GPa as measured by ruby fluorescence, the DAC was installed in the cold head of a Cryo-Industries ^{4}He flow cryostat mounted on the positioning stage of 16 ID-D. Synchrotron Mössbauer spectroscopy measurements were made by counting the delayed, coherent products of nuclear de-excitation as a function of time. The synchrotron ring was operated in top-up singlet mode with 153 ns bunch separation. The silicon high-resolution monochromator delivered 2 meV bandwidth. Spectra

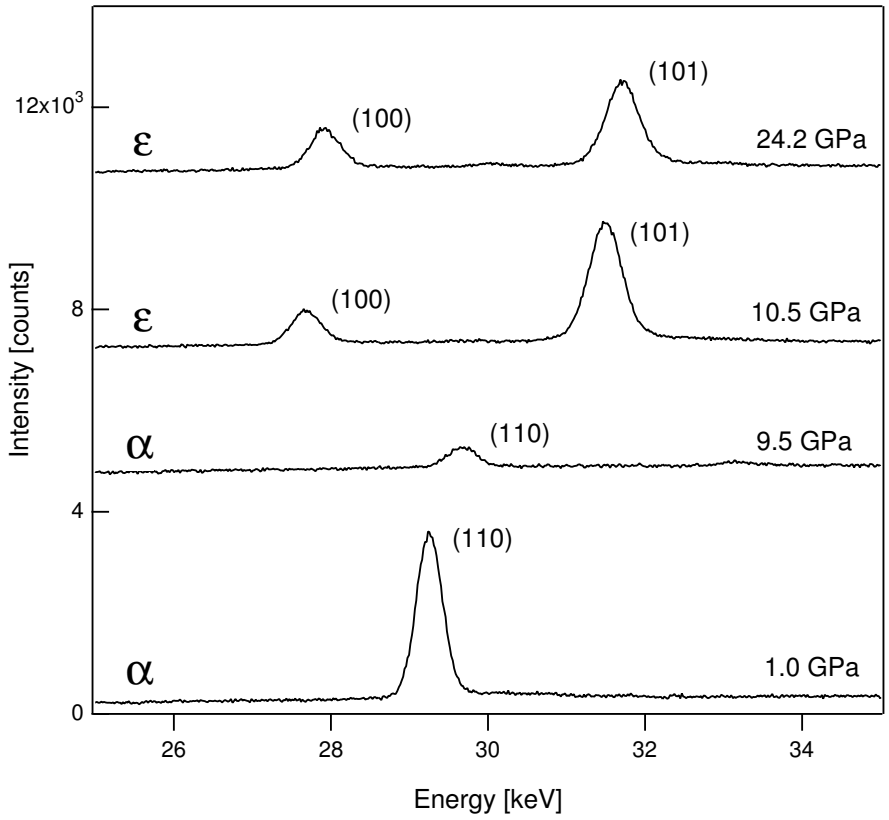

Figure 6.4: Energy-dispersive x-ray diffraction from $Fe_{92}Ni_8$ from 1 to 24 GPa. The alloy transforms from the α phase to the ϵ phase between 9 and 10 GPa.

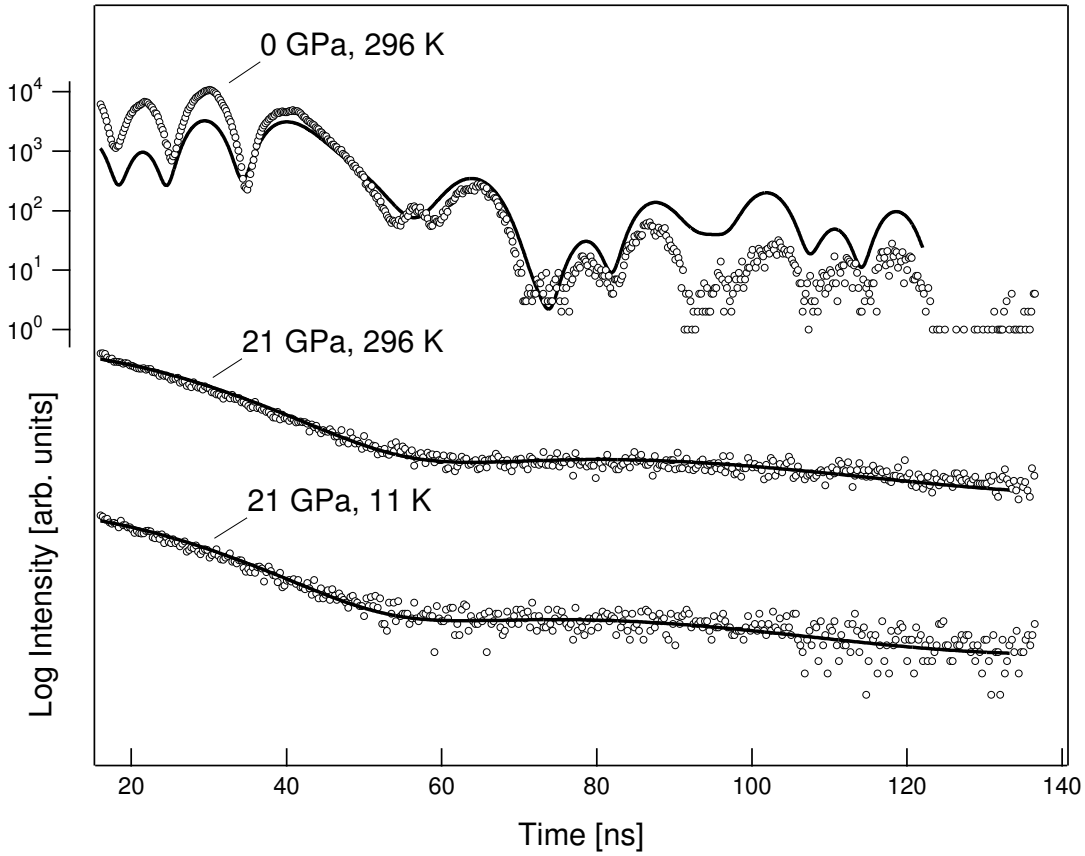

Figure 6.5: SMS spectra from $Fe_{92}Ni_8$ at various temperatures and pressures. The numerical scale applies only to the topmost curve, and is provided as a reference. Solid lines are theoretical fits to the data. At 0 GPa and 296 K, the sample is bcc. At 21 GPa, it is hcp.

were recorded at ambient temperature (296 K) and at 11 K. Temperature within the cryostat was monitored by a pair of diodes, located at the capillary orifice and at the sample, respectively. SMS measurements were also made on an isolated sample of the foil at ambient temperature and pressure to provide an experimental control.

The SMS spectrum from the sample at ambient pressure and temperature shows the quantum beats expected from the ferromagnetic α phase superimposed on a dynamical beat pattern resulting from the large effective thickness of the sample. The time spectra from the pressurized sample exhibit only dynamical beats at both 296 K and 11 K. Using the fitting routines in the program CONUSS [28], theoretical curves were fit to the measured data. These results can be seen in Figure 6.5, and

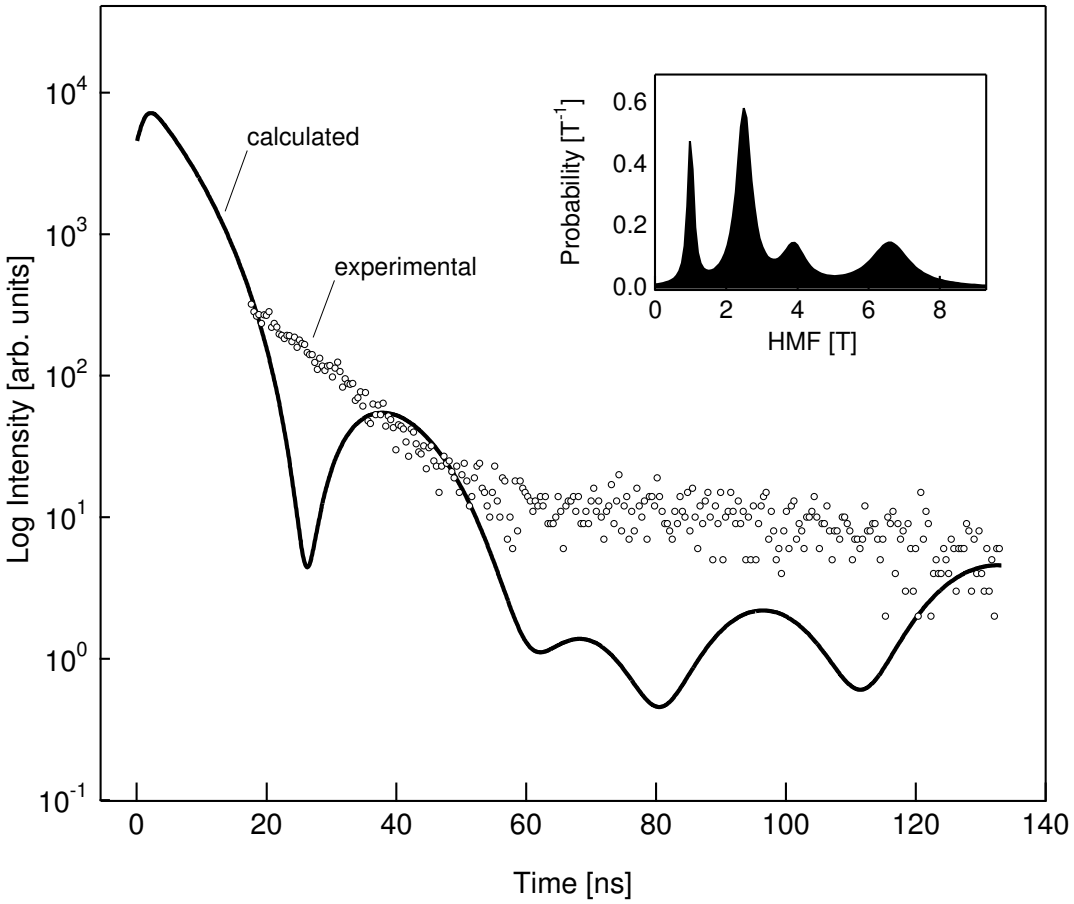

Figure 6.6: Experimental data from hcp $Fe_{92}Ni_8$ at 11 K and a simulated SMS spectrum generated with CONUSS based on DFT calculations of HMF in Fe_7Ni_1. The HMF distribution for the simulated spectrum is inset.

CONUSS input files can be found in Appendix B. The best fits to the ϵ-phase data were obtained when the hyperfine magnetic field parameter was set to zero. The hyperfine magnetic field distribution of the Fe_7Ni_1 supercell presented in Table 6.2 was also input to CONUSS to generate the expected SMS spectrum for *afmII* Fe_7Ni_1 at 20 GPa. The results are compared to the experimental SMS spectrum in Figure 6.6 below. The presence of the calculated HMF introduces substantial modulation in the SMS spectrum which is not present in the experimental data.

6.4 Discussion

The nature of the experimental problem and the manner in which the intial *afmII* results dovetail with experiment render it difficult to find the fault which causes these experiments and calculations to disagree. Direct evidence of the *afmII* structure in ϵ-Fe is impossible to obtain with the present means, due to its lack of a measurable HMF. A definitive study could be made with polarized neutron diffraction, but current DAC technology prohibits this, and ϵ-Fe cannot be quenched to ambient pressure. The means left to investigators are thus indirect, their interpretation clouded by multiple uncertainties.

One possible explanation of the lack of an observed HMF would be if the Néel temperature for the antiferromagnetic transition, T_N, is below the measurement temperature of 11 K; The DFT methods employed are 0 K only. Recent calculations by R. Cohen identified an upper bound on T_N using a multiscale approach for pure Fe. A tight-binding model was fit to LAPW calculations within the GGA [92] for 93 different magnetic configurations and moments for 4 and 64 atom supercells. Parameters of an extended Heisenberg model [104] were fit to the total energies, and classical Monte Carlo (MC) simulations were performed on a 512 atom hcp supercell. Values of T_N = 200 K at V = 70 bohr^3/atom, 45 K at V = 65 bohr^3/atom and 0 K (only very small moments are present) at V = 60 bohr^3/atom were found. The corresponding pressures for the theoretical equation of state are 0, 21, and 55 GPa, somewhat higher than the experimental volumes. The diffraction data (see section 6.3.4) from the $Fe_{92}Ni_8$ alloy return a volume of 70.85 bohr^3 at 19 GPa ($a = 2.468$ Å, $c = 3.977$ Å). The MC results suggest strongly that the measurement temperature of 11 K should be below T_N.

This leaves three apparent possible explanations of the results. The first is that the GGA functional is overestimating the exchange coupling in hcp-Fe. The errors could not be too large, because the transition pressure from magnetic bcc to hcp is well-predicted by the GGA [105]. We find that a 20% decrease in the effective Stoner

exchange parameter I[§] from the fitted value of 1.0746 eV/μ_B to 0.90 gives a drop in moment from 1.077 μ_B per atom to 0.053 at V = 70 bohr^3. An overestimate of the exchange coupling by 20% by the GGA does not seem unreasonable. The current GGA functional also systematically underestimates the magnitude of the contact interaction from core electrons [107, 108, 109], which is evident from the response of B_{core} to a nickel impurity in bcc $Fe_{53}Ni$ (Table 6.1). However, larger core polarization in the Fe_7Ni_1 cell would lead to a larger net HMF (Table 6.2) so this is unlikely.

Alternatively, quantum spin fluctuations [110], proposed as a mechanism for superconductivity [87] in ϵ-iron below 2 K may be faster than the Mössbauer lifetime, inhibiting detection of a hyperfine field. The hcp lattice is geometrically frustrated, meaning that it is impossible for local moments at lattice sites to have only neighbors of the opposite spin. Frustration creates a highly degenerate ground state that is extremely sensitive to small fluctuations (namely, those implied by the uncertainty principle) and possesses "residual" entropy even at 0 K. Fluctuations play an important role in the physics of many frustrated antiferromagnets, such as those with the pyrochlore [111] or gadolinium-gallium-garnet [112] structures. Spin fluctuation rates in the GHz range have been identified in these materials and cannot be discounted for the *afmII* or any other AFM spin structure for ϵ-Fe, though the MC results quoted above make it unlikely that geometrical frustration would inhibit ordering below 11K.

A third possibility is that a disordered Fe-Ni alloy behaves differently from the ordered Fe_7Ni_1 supercell, resulting in cancellation of the HMF in the chemically disordered state. For many material properties, it is not possible to reproduce the behavior of the disordered state with a conventional ordered supercell. Elastic [113] and vibrational [114] properties, for example, exhibit considerable variation between ordered and disordered structures with the same chemical composition. However, the hyperfine magnetic field is a fundamentally local property; transmission ^{57}Fe Mössbauer spectra of alloys can be fit satisfactorily using parameters for only first and second

[§]The Stoner parameter may be expressed as $I = \int \gamma^2(\vec{r})|K(\vec{r})|d\vec{r}$, where γ is a function of the electronic density of states at the Fermi level and K is a functional of the exchange-correlation potential. See [106].

Table 6.3: Summary of nickel concentrations and associated HMF for atoms in the Fe_7Ni_1 supercell with different local symmetry

Atom	Ni 1nn	Ni 2nn	at %	B_{tot} [kG]
Fe 1 in Fe_7Ni_1	0	0	12.5	25
Fe 2 in Fe_7Ni_1	0	2	12.5	10
Fe 3 in Fe_7Ni_1	2	4	12.5	39
Fe 4 in Fe_7Ni_1	1	0	25	24
Fe 5 in Fe_7Ni_1	3	0	25	66

neighbor shells [94].

With this assumption in hand, compromises regarding the size of the supercell unit and its symmetry were made in the interest of computational efficiency. In the Fe_7Ni_1 supercell, a consequence is that Ni impurities have two Ni first nearest neighbors while the relatively high-symmetry *Pmma* space group (shared by the pure Fe *afmII* structure) is retained. Nonetheless, the fraction of ^{57}Fe atoms in *Pmma* Fe_7Ni_1 with n_j nickel first neighbors is comparable to that number for the random $Fe_{92}Ni_8$ solid solution.

For a random solid solution, one can assign a binomial probability for finding n_j solute atoms in nearest neighbor shell j with a number of sites N_j for a given lattice. This probability is given by:

$$P(N_j, n_j, c_{Ni}) \equiv \frac{N_j!}{(N_j - n_j)!\ n_j!}\ (c_{Ni})^{n_j}\ (1 - c_{Ni})^{N_j - n_j} \tag{6.4.1}$$

for the nominal nickel concentration $c_{Ni} = 0.08$, and given that the first nearest neighbor shell of the hcp lattice has $N_j = 12$, the probability of a given ^{57}Fe atom having 0, 1, 2, or 3 Ni first neighbors is 0.37, 0.38, 0.18, and 0.05, respectively. The calculational supercell contains 16 atoms labeled according to Figure 6.2, each with a different multiplicity. Table 6.3 summarizes the local environments of these atoms and the hyperfine field at their nuclei. Compared to the set of probabilities for the random solution, the supercell has an fraction of ^{57}Fe atoms with 0, 1, 2, or 3 Ni first neighbors of 0.28, 0.28, 0.14, and 0.28. The largest disparity between the Fe_7Ni_1

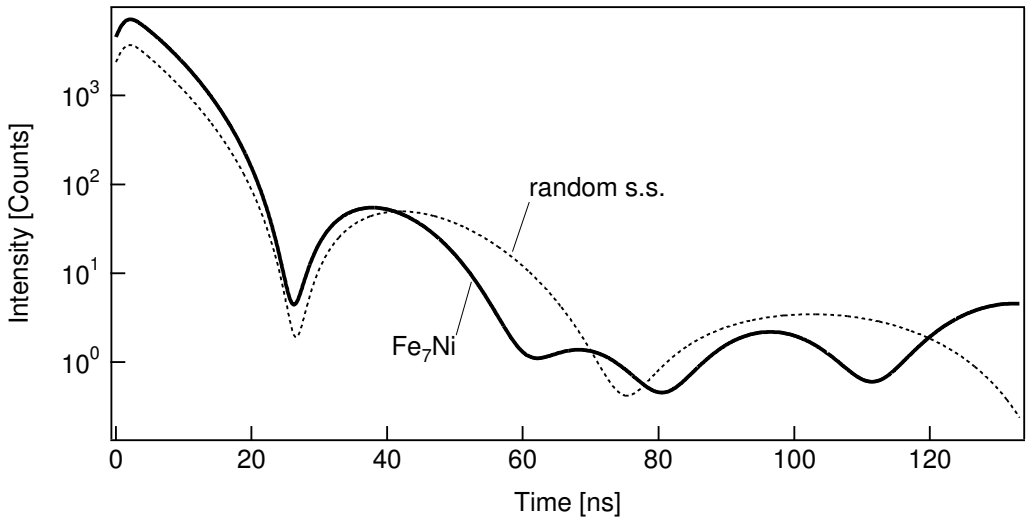

Figure 6.7: Comparison of SMS spectra generated by CONUSS for the hyperfine field distirbution given by Fe_7Ni_1 and by assigning the distribution based on an assumption of a random solid solution. See text for details.

structure and the solid solutions lies in the fraction of ^{57}Fe atoms with 3 Ni first nearest neighbors. The supercell has too many atoms with this environment, 28% compared to only 5% for the solution. To investigate the effect of this inconsistency on the expected SMS spectrum, CONUSS was used to simulate a second spectrum, with hyperfine fields still determined by the DFT calculations but with the distribution given by the binomial probabilities above. The resultant curve is compared to the original simulated spectrum in Figure 6.7 below. This spectrum is still significantly different from the experimentally measured results. The effect of a reduced average hyperfine field manifests in an apparent increase in quantum beat period, consistent with the lowered average frequency of the coherently emitted radiation.

6.5 Conclusions

A complete explanation and description of magnetism in ϵ-iron remains to be found. Though this is a very old problem, recent experimental and computational contributions have made it new again.

The argument for antiferromagnetic ordering in ϵ-Fe is compelling. Much better

agreement is found between theory for AFM ϵ-iron and experiment for the equation of state and elasticity than for non-magnetic iron [6]. In addition, the observed Raman mode is split [115], and the splitting is consistent with magnetic splitting for the *afmII* structure [6]. Nevertheless, the SMS experiment shows clearly that Fe-Ni has no static moments, in disagreement with my DFT calculations for an ordered supercell.

The case for fluctuating moments in ϵ-Fe is bolstered by the exotic superconductivity of the phase [88], and recent work linking it to itinerant magnetism [90, 89] and spin fluctuations [110, 116] in metals. However, it is also evident from my HMF calculations for α-Fe that significant flaws exist in the existing exchange-correlation functional regarding the contact hyperfine field. The extension of these shortcomings to the *afmII* calculations would certainly cast significant doubt on the veracity of the DFT results.

The ambiguities addressed here are symptomatic of the resistance to both theoretical and experimental understanding that ϵ-Fe has shown for nearly half a century. It is apparent that both of these modes of inquiry must be improved before that understanding is complete.

6.6 Future Work

It may be possible to gain information about the presence of quantum spin fluctuations in ϵ-Fe with the synchrotron x-ray emission spectroscopy (XES) technique [117] at a suitable third-generation source. The enhanced local moments calculated for the Ni-doped *afmII* structure may be detectable by XES given the much shorter timescale for electronic x-ray scattering ($\sim$ps) compared to ^{57}Fe nuclear resonant scattering (141 ns). Briefly, in the XES process synchrotron x-rays excite core holes in the sample material and the characteristic emission spectrum from the decay of these holes is subsequently measured. In the transition metals, the spectral profile of the Kβ ($3p \rightarrow 1s$) emission line is almost totally due to exchange coupling of the $3p$ electrons and the local moment, which manifests as a splitting of the Kβ line

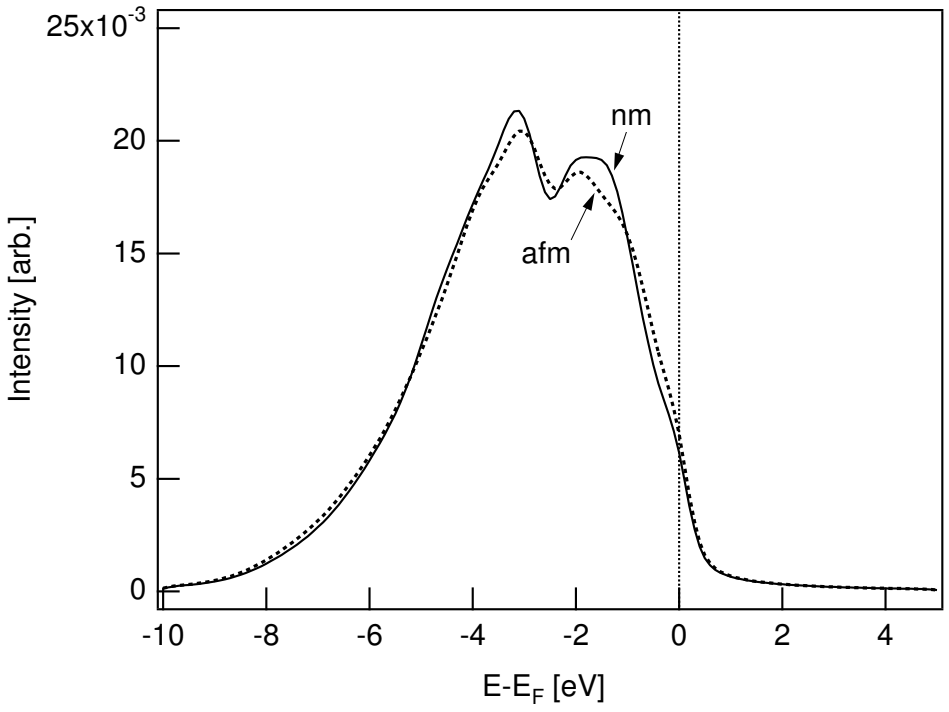

Figure 6.8: Simulated XES spectrum from the Fe5 environment in the Fe_7Ni_1 supercell for *afmII* and nonmagnetic states.

into high-spin and low-spin components. In the presence of local moments the $K\beta$ peak exhibits a displaced "satellite" peak. XES has previously been used to probe pressure induced transitions in FeS [118], FeO [119], and even the $\alpha \rightarrow \epsilon$ transition in pure Fe [117]. The measurements of Rueff, *et al.* on ϵ-Fe were conducted at ambient temperature, most probably ruling out the possibility of detecting a magnetic phase based on the estimates above. A proper XES measurement on a hcp Fe-Ni alloy would represent a significant experimental challenge. In order to freeze the putative fluctuations as completely as possible, a cryogenic environment would be needed, considerably limiting the solid angle accessible to the x-ray detector. The WIEN2K package offers some utilities for modeling XES spectra, but these are less than comprehensive. Using the XSPEC program, I was able to obtain the core transition probability for electrons relative to the Fermi level, which is shown in Figure 6.8. All the information necessary to derive the Kβ spectrum is present in the electron density, but programming remains to be done if this information is to be extracted.

A simulated emission spectrum would likely be a prerequisite for the allocation of time at a synchrotron beamline for this proposed work.

There certainly exists room for refinement of the computational methods employed in this chapter. Some of the inadequacies of the Fe_7Ni_1 cell can be addressed by increasing the size of the cell and varying the positions of impurity atoms. Application of special quasirandom structures (SQS) [120, 121] with related cluster-expansion based packages such as ATAT [122] may produce different results by eliminating spurious periodicities in the ordered supercell formulation. This approach has been successful for bulk thermodynamics when employed with pseudopotential codes, but has yet to be extended to full-potential codes such as WIEN2K that are a prerequisite for the calculation of hyperfine fields.

Polarized neutron diffraction [123] studies on ϵ-Fe may solve many of the mysteries of its magnetic behavior. With the advances in pressure cell technology promised by large CVD diamonds and the massive neutron flux expected from the Spallation Neutron Source (see section 2.3), this measurement could soon be a reality.

Chapter 7

Concluding Remarks

The science and technology of high pressure have existed for a relatively short period of time. Even as techniques for pressure generation are reaching a robust maturity, the collection of compatible characterization techniques is still lacking. Synchrotron-based nuclear resonance methods have been among the most successful of these, but the limited extensibility of these approaches to non–Mössbauer nuclei presents something of a barrier to a complete understanding of lattice vibrations and magnetism in metallic systems at high pressure. Even so, the development of the topics addressed in this thesis shows that generalized conclusions regarding the solid state can be made with iron as the exemplar.

The mysteries of anomalous vibrational modes in nanocrystalline microstructures were partly elucidated by the inelastic scattering experiments described in chapter 4. Effects on the phonon density of states from mesoscopic defects were thoroughly repudiated by the NRIXS results, which also showed that the pressure response of soft forces in a nanocrystalline aggregate is identical to that in a coarse-grained material. Ultra-low-energy neutron inelastic scattering measurements showed that a portion of these low-energy modes are due to collective excitations of the microstructure.

The wildly anomalous properties which were originally ascribed to nanocrystals are gradually being replaced by a more reasonable acknowledgment of the effects of defect density. Though nanocrystalline materials have not turned out to be a technological panacea, a complete understanding of the effects of nanoscale defects

on the phonon spectrum of solids may become increasingly valuable as our devices shrink. The technology of heat dissipation in electronic devices and tribology in mechanical systems such as MEMS are poised to benefit greatly from any advances in "phonon engineering."

In chapter 6, an old hypothesis of antiferromagnetism in ϵ-Fe was investigated with the new tools of density functional theory and synchrotron Mössbauer spectrometry. Though DFT predicted a static antiferromagnetic ground state with measurable hyperfine fields for a hcp Fe-Ni alloy, SMS measurements were unable to detect any such HMF. This apparent contradiction is of the sort that moves science forward, however incrementally. Both explanations for the disparity offer clear avenues for advancing our understanding of nature. If in fact quantum spin fluctuations are responsible for the null SMS result, the benefits to the scholarship regarding the exotic superconductivity in iron may be substantial. The other option, that the current exchange-correlation functional is deficient, may on balance lead to an even greater benefit: a more accurate *ab initio* theory.

Appendix A

Wien2k Input Files for the AFM Fe-Ni Supercell

A.1 Antiferromagnetic Case

A.1.1 afmFeNi.struct

```
afmII Fe7Ni
P                             6 51 Pmma
RELA
7.452108  9.315136 16.134286 90.000000 90.000000 90.000000
ATOM  -1: X=0.25000000 Y=0.00000000 Z=0.42010845
MULT= 2          ISPLIT= 8
-1: X=0.75000000 Y=0.00000000 Z=0.57989155
Fe1        NPT=  781  R0=.000050000 RMT=   2.00000   Z:  26.00000
LOCAL ROT MATRIX:    1.0000000 0.0000000 0.0000000
0.0000000 1.0000000 0.0000000
0.0000000 0.0000000 1.0000000
ATOM  -2: X=0.25000000 Y=0.50000000 Z=0.41945274
MULT= 2          ISPLIT= 8
-2: X=0.75000000 Y=0.50000000 Z=0.58054726
Fe2        NPT=  781  R0=.000050000 RMT=   2.00000   Z:  26.00000
LOCAL ROT MATRIX:    1.0000000 0.0000000 0.0000000
0.0000000 1.0000000 0.0000000
0.0000000 0.0000000 1.0000000
```

```
ATOM  -3: X=0.25000000 Y=0.00000000 Z=0.91706247
MULT= 2          ISPLIT= 8
-3: X=0.75000000 Y=0.00000000 Z=0.08293753
Fe3        NPT=  781  R0=.000050000 RMT=   2.00000   Z:  26.00000
LOCAL ROT MATRIX:    1.0000000 0.0000000 0.0000000
0.0000000 1.0000000 0.0000000
0.0000000 0.0000000 1.0000000
ATOM  -4: X=0.25000000 Y=0.50000000 Z=0.91731742
MULT= 2          ISPLIT= 8
-4: X=0.75000000 Y=0.50000000 Z=0.08268258
Ni1        NPT=  781  R0=.000050000 RMT=   2.00000   Z:  28.00000
LOCAL ROT MATRIX:    1.0000000 0.0000000 0.0000000
0.0000000 1.0000000 0.0000000
0.0000000 0.0000000 1.0000000
ATOM  -5: X=0.25000000 Y=0.24943021 Z=0.66740832
MULT= 4          ISPLIT= 8
-5: X=0.25000000 Y=0.75056979 Z=0.66740832
-5: X=0.75000000 Y=0.24943021 Z=0.33259168
-5: X=0.75000000 Y=0.75056979 Z=0.33259168
Fe4        NPT=  781  R0=.000050000 RMT=   2.00000   Z:  26.00000
LOCAL ROT MATRIX:    0.0000000 0.0000000 1.0000000
1.0000000 0.0000000 0.0000000
0.0000000 1.0000000 0.0000000
ATOM  -6: X=0.25000000 Y=0.24801705 Z=0.16922383
MULT= 4          ISPLIT= 8
-6: X=0.25000000 Y=0.75198295 Z=0.16922383
-6: X=0.75000000 Y=0.24801705 Z=0.83077617
-6: X=0.75000000 Y=0.75198295 Z=0.83077617
Fe5        NPT=  781  R0=.000050000 RMT=   2.00000   Z:  26.00000
LOCAL ROT MATRIX:    0.0000000 0.0000000 1.0000000
1.0000000 0.0000000 0.0000000
0.0000000 1.0000000 0.0000000
8      NUMBER OF SYMMETRY OPERATIONS
1 0 0 0.0000000
0 1 0 0.0000000
```

```
0 0 1 0.0000000
1
-1 0 0 0.5000000
0-1 0 0.0000000
0 0 1 0.0000000
2
-1 0 0 0.0000000
0 1 0 0.0000000
0 0-1 0.0000000
3
1 0 0 0.5000000
0-1 0 0.0000000
0 0-1 0.0000000
4
-1 0 0 0.0000000
0-1 0 0.0000000
0 0-1 0.0000000
5
1 0 0 0.5000000
0 1 0 0.0000000
0 0-1 0.0000000
6
1 0 0 0.0000000
0-1 0 0.0000000
0 0 1 0.0000000
7
-1 0 0 0.5000000
0 1 0 0.0000000
0 0 1 0.0000000
8
```

A.1.2 afmFeNi.in1

```
WFFIL        (WFPRI, SUPWF)
  8.00       10    4 (R-MT*K-MAX; MAX L IN WF, V-NMT
```

```
 0.50    4  0      (GLOBAL E-PARAMETER WITH n OTHER CHOICES, global APW/LAPW)
1    0.60      0.000 CONT 1
1   -3.97      0.005 STOP 1
2    0.70      0.010 CONT 1
0    0.50      0.000 CONT 1
 0.50    4  0      (GLOBAL E-PARAMETER WITH n OTHER CHOICES, global APW/LAPW)
1    0.60      0.000 CONT 1
1   -3.97      0.005 STOP 1
2    0.70      0.010 CONT 1
0    0.50      0.000 CONT 1
 0.50    4  0      (GLOBAL E-PARAMETER WITH n OTHER CHOICES, global APW/LAPW)
1    0.60      0.000 CONT 1
1   -3.97      0.005 STOP 1
2    0.70      0.010 CONT 1
0    0.50      0.000 CONT 1
 0.50    4  0      (GLOBAL E-PARAMETER WITH n OTHER CHOICES, global APW/LAPW)
1    0.60      0.000 CONT 1
1   -4.96      0.005 STOP 1
2    0.70      0.010 CONT 1
0    0.50      0.000 CONT 1
 0.50    4  0      (GLOBAL E-PARAMETER WITH n OTHER CHOICES, global APW/LAPW)
1    0.60      0.000 CONT 1
1   -3.78      0.005 STOP 1
2    0.70      0.010 CONT 1
0    0.50      0.000 CONT 1
 0.50    4  0      (GLOBAL E-PARAMETER WITH n OTHER CHOICES, global APW/LAPW)
1    0.60      0.000 CONT 1
1   -3.78      0.005 STOP 1
2    0.70      0.010 CONT 1
0    0.50      0.000 CONT 1
K-VECTORS FROM UNIT:4   -7.0       1.5      emin/emax window
```

A.1.3 afmFeNi.inst

```
Fe1
Ar 3 5
3, 2,2.0  N
3, 2,2.0  N
3,-3,2.5  N
3,-3,0.0  N
4,-1,1.0  N
4,-1,0.5  N
Fe2
Ar 3 5
3, 2,2.0  N
3, 2,2.0  N
3,-3,2.5  N
3,-3,0.0  N
4,-1,1.0  N
4,-1,0.5  N
Fe3
Ar 3 5
3, 2,2.0  N
3, 2,2.0  N
3,-3,2.5  N
3,-3,0.0  N
4,-1,1.0  N
4,-1,0.5  N
Ni1
Ar 3 5
3, 2,2.0  N
3, 2,2.0  N
3,-3,3.0  N
3,-3,1.0  N
4,-1,1.0  N
4,-1,1.0  N
Fe4
```

```
   Ar 3 5
   3, 2,2.0  N
   3, 2,2.0  N
   3,-3,0.0  N
   3,-3,2.5  N
   4,-1,0.5  N
   4,-1,1.0  N
   Fe5
   Ar 3 5
   3, 2,2.0  N
   3, 2,2.0  N
   3,-3,0.0  N
   3,-3,2.5  N
   4,-1,0.5  N
   4,-1,1.0  N
   ****
   ****         END of input
```

A.2 Nonmagnetic Case

A.2.1 nmFeNi.struct

```
   nm FeNi based on 70 au3
   P   LATTICE,NONEQUIV.ATOMS:  651_Pmma
   MODE OF CALC=RELA unit=bohr
     7.452108  9.315136 16.134286 90.000000 90.000000 90.000000
   ATOM  -1: X=0.25000000 Y=0.00000000 Z=0.41666666
     MULT= 2          ISPLIT= 8
 -1: X=0.75000000 Y=0.00000000 Z=0.58333334
   Fe1        NPT=  781  R0=0.00005000 RMT=    2.0000   Z: 26.0
   LOCAL ROT MATRIX:    1.0000000 0.0000000 0.0000000
0.0000000 1.0000000 0.0000000
0.0000000 0.0000000 1.0000000
   ATOM  -2: X=0.25000000 Y=0.50000000 Z=0.41666666
```

```
     MULT= 2          ISPLIT= 8
 -2: X=0.75000000 Y=0.50000000 Z=0.58333334
   Fe2        NPT=  781  R0=0.00005000 RMT=    2.0000   Z: 26.0
   LOCAL ROT MATRIX:    1.0000000 0.0000000 0.0000000
0.0000000 1.0000000 0.0000000
0.0000000 0.0000000 1.0000000
   ATOM  -3: X=0.25000000 Y=0.00000000 Z=0.91666666
     MULT= 2          ISPLIT= 8
 -3: X=0.75000000 Y=0.00000000 Z=0.08333334
   Fe3        NPT=  781  R0=0.00005000 RMT=    2.0000   Z: 26.0
   LOCAL ROT MATRIX:    1.0000000 0.0000000 0.0000000
0.0000000 1.0000000 0.0000000
0.0000000 0.0000000 1.0000000
   ATOM  -4: X=0.25000000 Y=0.25000000 Z=0.66666667
     MULT= 4          ISPLIT= 8
 -4: X=0.75000000 Y=0.75000000 Z=0.33333333
 -4: X=0.75000000 Y=0.25000000 Z=0.33333333
 -4: X=0.25000000 Y=0.75000000 Z=0.66666667
   Fe4        NPT=  781  R0=0.00005000 RMT=    2.0000   Z: 26.0
   LOCAL ROT MATRIX:    0.0000000 0.0000000 1.0000000
1.0000000 0.0000000 0.0000000
0.0000000 1.0000000 0.0000000
   ATOM  -5: X=0.25000000 Y=0.25000000 Z=0.16666666
     MULT= 4          ISPLIT= 8
 -5: X=0.75000000 Y=0.75000000 Z=0.83333334
 -5: X=0.75000000 Y=0.25000000 Z=0.83333334
 -5: X=0.25000000 Y=0.75000000 Z=0.16666666
   Fe5        NPT=  781  R0=0.00005000 RMT=    2.0000   Z: 26.0
   LOCAL ROT MATRIX:    0.0000000 0.0000000 1.0000000
1.0000000 0.0000000 0.0000000
0.0000000 1.0000000 0.0000000
   ATOM  -6: X=0.25000000 Y=0.50000000 Z=0.91666666
     MULT= 2          ISPLIT= 8
 -6: X=0.75000000 Y=0.50000000 Z=0.08333334
   Ni1        NPT=  781  R0=0.00005000 RMT=    2.0000   Z: 28.0
```

```
   LOCAL ROT MATRIX:    1.0000000 0.0000000 0.0000000
0.0000000 1.0000000 0.0000000
0.0000000 0.0000000 1.0000000
      8      NUMBER OF SYMMETRY OPERATIONS
    1 0 0 0.0000000
    0 1 0 0.0000000
    0 0 1 0.0000000
  1
   -1 0 0 0.5000000
    0-1 0 0.0000000
    0 0 1 0.0000000
  2
   -1 0 0 0.0000000
    0 1 0 0.0000000
    0 0-1 0.0000000
  3
    1 0 0 0.5000000
    0-1 0 0.0000000
    0 0-1 0.0000000
  4
   -1 0 0 0.0000000
    0-1 0 0.0000000
    0 0-1 0.0000000
  5
    1 0 0 0.5000000
    0 1 0 0.0000000
    0 0-1 0.0000000
  6
    1 0 0 0.0000000
    0-1 0 0.0000000
    0 0 1 0.0000000
  7
   -1 0 0 0.5000000
    0 1 0 0.0000000
    0 0 1 0.0000000
```

```
8
```

A.2.2 nmFeNi.in1

```
WFFIL        (WFPRI, SUPWF)
  8.00       10    4 (R-MT*K-MAX; MAX L IN WF, V-NMT
  0.50    4  0      (GLOBAL E-PARAMETER WITH n OTHER CHOICES, global APW/LAPW)
1    0.60      0.000 CONT 1
1   -3.97      0.005 STOP 1
2    0.70      0.010 CONT 1
0    0.50      0.000 CONT 1
  0.50    4  0      (GLOBAL E-PARAMETER WITH n OTHER CHOICES, global APW/LAPW)
1    0.60      0.000 CONT 1
1   -3.97      0.005 STOP 1
2    0.70      0.010 CONT 1
0    0.50      0.000 CONT 1
  0.50    4  0      (GLOBAL E-PARAMETER WITH n OTHER CHOICES, global APW/LAPW)
1    0.60      0.000 CONT 1
1   -3.97      0.005 STOP 1
2    0.70      0.010 CONT 1
0    0.50      0.000 CONT 1
  0.50    4  0      (GLOBAL E-PARAMETER WITH n OTHER CHOICES, global APW/LAPW)
1    0.60      0.000 CONT 1
1   -3.97      0.005 STOP 1
2    0.70      0.010 CONT 1
0    0.50      0.000 CONT 1
  0.50    4  0      (GLOBAL E-PARAMETER WITH n OTHER CHOICES, global APW/LAPW)
1    0.60      0.000 CONT 1
1   -3.97      0.005 STOP 1
2    0.70      0.010 CONT 1
0    0.50      0.000 CONT 1
  0.50    4  0      (GLOBAL E-PARAMETER WITH n OTHER CHOICES, global APW/LAPW)
1    0.60      0.000 CONT 1
1   -4.96      0.005 STOP 1
2    0.70      0.010 CONT 1
```

```
 0    0.50      0.000 CONT 1
K-VECTORS FROM UNIT:4   -7.0       1.5      emin/emax window
```

A.2.3 nmFeNi.inst

```
Fe 1
Ar 3 5
3, 2,2.0  N
3, 2,2.0  N
3,-3,2.5  N
3,-3,0.0  N
4,-1,1.0  N
4,-1,0.5  N
Fe 2
Ar 3 5
3, 2,2.0  N
3, 2,2.0  N
3,-3,2.5  N
3,-3,0.0  N
4,-1,1.0  N
4,-1,0.5  N
Fe 3
Ar 3 5
3, 2,2.0  N
3, 2,2.0  N
3,-3,2.5  N
3,-3,0.0  N
4,-1,1.0  N
4,-1,0.5  N
Fe 4
Ar 3 5
3, 2,2.0  N
3, 2,2.0  N
3,-3,2.5  N
3,-3,0.0  N
```

```
4,-1,1.0  N
4,-1,0.5  N
Fe 5
Ar 3 5
3, 2,2.0  N
3, 2,2.0  N
3,-3,2.5  N
3,-3,0.0  N
4,-1,1.0  N
4,-1,0.5  N
Ni 1
Ar 3 5
3, 2,2.0  N
3, 2,2.0  N
3,-3,3.0  N
3,-3,1.0  N
4,-1,1.0  N
4,-1,1.0  N
****
****     End of Input
```

Appendix B

CONUSS Input Files for HCP Fe-Ni

B.1 Material Input File

```
*! Version 1.5
*
*************************************************************************
*
*  fit parameters
*  ==============
*
*   the first number gives the start value for each parameter
*   the second number gives the parameter variation when
*    the derivatives are calculated
*
*
*********1*********2*********3*********4*********5*********6*********7**
*
*  MB isotope and MB transition
*  ============================
*
 (1) mass number   :: 57
*
*    ground state
```

```
 (2) spin                      :: 0.5
 (3) g-factor                  :: 0.18121
 (4) qudrupole moment / barn   :: 0
*
*    excited state
 (5) spin                        ::  1.5
 (6) g-factor                    :: -0.10348
 (7) qudrupole moment / barn     ::  0.187
 (8) half life time   / ns       :: 97.81
 (9) internal conversion factor  ::  8.21
*
*    transition
 (10) energy / keV              :: 14.41303
 (11) multipolarity             :: M1
 (12) interference coefficient  :: 0
*
*********1*********2*********3*********4*********5*********6*********7**
*
*  Lattice parameters
*  ==================
*
 (13) Debye temperature of the material / K  :: 440
 (14) real temperature of the material  / K  ::  11
*
*
*  size and angles of the unit cell of the material
*   artificial unit cell, matches density of iron
*
*  length of base vectors
 (15) length of #1 / Angstroem :: 2.18
 (16)           #2 / Angstroem :: 2.18
 (17)           #3 / Angstroem :: 2.18
*
*  angles between base vectors
 (18) angle between     #2,#3  / degrees  :: 90
```

```
 (19)                   #3,#1  / degrees  :: 90
 (20)                   #1,#2  / degrees  :: 90
*
*********1*********2*********3*********4*********5*********6*********7**
*
*  defining the lattice of the MB atom
*  ===================================
*
*
 (21) name of the MB atom                  :: iron
 (22) abundance of the MB atom             :: 0.20
 (23) atomic charge number of the MB atom  :: 26
 (24) number of sites of the MB atom       ::  1
*
************************************************
*
*  defining the hyperfine interactions
*  ===================================
*
*   the following modes are supported :
*
*    'poly'           averaging over all directions
*                     and polarizations of the incident photon
*                     while keeping the angles between magnetic
*                     hyperfine field (Bhf) and electric field
*                     gradient (EFG) fixed. The texture of a
*                     sample is given in input lines 26.*.1.18
*                     for each individual site. This is a good
*                     approximation for forward scattering from
*                     textured powder samples without external
*                     fields.
*
*    'random_efg<N>'  averaging over all directions of
*                     the EFG while keeping the directions
*                     of Bhf and incident photon fixed.
```

```
*                    This is a good approximation for
*                    forward scattering of none texture
*                    powder samples with an external
*                    magnetic field applied.
*                    <N>*24 specifies the number of grid
*                    points used for averaging.
*                    Note: The procedure gives wrong results
*                    in case of an axially asymmetric EFG.
*
*    'mono', 'none'   no averaging, resort to texture=100\%
*
*    'btrelax'        the Blume-Tjon relaxation model is
*                     applied. The relaxation rates must be
*                     given in a file. The file name is given
*                     in input fields 26.*.1.16 for each indi-
*                     vidual site. Note the reduced data fields
*                     that define the relaxation subsites.
*                     No averaging, resort to texture=100\%
*
*    'btrelaxP'       the Blume-Tjon relaxation model is applied.
*                     Textured powder samples can be treated
*                     by a texture in input fields 26.*.1.18.
*                     The same rules as in the case 'poly' apply.
*
 (25) type of averaging for hyperfine int. :: poly
*
************************************************
*
*  defining MB site #1
*
 (26.1.1)  memo name for the site         :: Fe
 (26.1.2)  number of MB atoms in the site :: 1
 (26.1.3)  ionization number              :: 0
 (26.1.4)  weight of the sublattice       :: 0.92
*
```

```
 (26.1.5)  isomer shift             / mm/s       ::  0
*
 (26.1.6)  magnetic hyperfine field / T          ::  0
 (26.1.7)  magnetic polar anisotropy             ::  0
 (26.1.8)  magnetic azimuthal anisotropy         ::  0
 (26.1.9)  magn.hyp.field dir. angle theta / deg ::  0
 (26.1.10) magn.hyp.field dir. angle phi   / deg ::  0
*
 (26.1.11) quadrupole splitting     / mm/s       ::  0
 (26.1.12) asymmetry parameter                   ::  0
 (26.1.13) euler angle alpha for efg=>xtal /deg  ::  0
 (26.1.14) euler angle beta  for efg=>xtal /deg  ::  0
 (26.1.15) euler angle gamma for efg=>xtal /deg  ::  0
*
 (26.1.16) relaxation rate input file    ::
*(26.1.17) field distribution input file :: <!
*
*************************************************************************
*
*    Field distribution data input file of program package CONUSS
*
*************************************************************************
*
*  Define distribution target
*  ==========================
*
* syntax :  Target <type of hyp.int.>
*
* for <type of hyp.int.> you may choose from the
*  following list:
*                       magnetic hyperfine field
*                       isomer shift
*                       efg
*
*  Target magnetic hyperfine field
```

```
*
*
*********1*********2*********3*********4*********5*********6*********7**
*
*  Predefined distributions
*  ========================
*
* syntax :  Make <type> <no. of points> <FWHM>
*
* for <type> you may choose from the following list:
*          Gaussian
*          Lorentzian
*          Rectangle
*
* the maximum value of <no. of points> is fixed at installation
*  time, usually 300.
*
* <FWHM> is the absolute FWHM for <type of hyp.int.>=isomer shift,
*  otherwise it is relative to the value defined in the MIF.
*
*  Make Lorentzian 61 @Bdst
*
*********1*********2*********3*********4*********5*********6*********7**
* end of distribution data input file
  !
*
  (26.1.18) texture coefficient  / \%     :: 0
  (26.1.19) reserved for later versions  ::
*
* (26.1.20 etc.) positions of the MB atoms of site #1
*
  0 0 0
*
*********1*********2*********3*********4*********5*********6*********7**
*
```

```
*  defining the lattices of the non MB atoms
*  =========================================
*
 (27) number of lattices of non MB atoms :: 1
*
*************************************************
*
*  defining non MB lattice #1
*
 (28.1.1) name of the atom                  :: nickel
 (28.1.2) atomic charge number of the atom  :: 28
 (28.1.3) number of atoms in the lattice    :: 1
 (28.1.4) ionization number                 :: 0
 (28.1.5) weight of the lattice             :: 0.08
 (28.1.6) reserved for later versions ::
 (28.1.7) reserved for later versions ::
 (28.1.8) reserved for later versions ::
*
* (28.1.9 etc.) positions of the atoms of non MB lattice #1
*
 0 0 0
*
*********1*********2*********3*********4*********5*********6*********7**
*
```

B.2 in_kref

```
*! Version 1.5
*
*******************************************************************************
*
* input and output files
* ======================
```

```
*
  (1) material data input file      :: hFe_in
*
  (2) transmission data output file :: data_trns_hFe
*
*
  (3) name of the material          :: hcp Fe92Ni8
*
*********************************************************************
*
* module run mode
* ===============
*
*  you may use :  r  for  reflected channel in Bragg/Laue geometry
*                 t       transmitted  .."..
*                 f       forward scattering geometry
*
  (4) mode :: f
*
*********************************************************************
*
* netplanes and surface
* =====================
*
  (5) 1. Miller index of reflection       :: 0
  (6) 2. ...                              :: 0
  (7) 3. ...                              :: 0
*
  (8)  1. component of the surface normal  :: 0
  (9)  2. ...                               :: 0
  (10) 3. ...                               :: 1
*
*********************************************************************
*
* incident radiation
```

```
* ==================
*
* angle between projection of k_in to the
* surface and a reference vector, which is
*   - for a symmetric reflection the projection
*           of the base vector 1 to the surface
*   - for a asymmetric reflection the intersection
*           of surface and netplanes
*
  (11) azimuthal angle of k_in / deg    ::  0
*
*********************************************************************
*
* external magnetic field
* ========================
*
* angle between the projection of k_in and the
*   projection of B_ext to the surface
*
  (12) azimuthal angle of B_ext / deg.  ::  0
*
* angle between B_ext and the surface normal
*
  (13) polar angle of B_ext / deg.      :: 90
*
* magnitude of the external magnetic field
*
  (14) magnitude / Tesla  ::  0
*
*********************************************************************
*
* energy range relative to the nuclear resonance
* ==============================================
*
  (15) begin calculation at this energy / gamma  :: -200
```

```
  (16) stop  ...                                  :: +200
  (17) nr. of steps (max. 2801)                   :: 2801
*
************************************************************************
*
* thickness of the material perpendicular to the surface
* ======================================================
*
% (18) thickness unit / micron  ::  10 0.1
*
*
* thickness range, give values in units defined above
*
  (19) begin calculation at this thickness / units ::    1
  (20) stop  ...                                   ::    1
  (21) nr. of steps (max. 100)                     ::    1
*
************************************************************************
*
* control of the printout
* =======================
*
*
*     description of the internal
*      variables to be printed
*                                                      print?
S01 : Miller indices                                :: yes
S02 : direction of the incoming beam                :: yes
S03 : direction of the external magn. field         :: yes
S04 : Bragg angle                                   :: yes
S05 : energy grid                                   :: yes
S06 : base vectors of the unit cell                 :: no
S07 : normal vectors of netplanes and surface       :: yes
S08 : incident beam, k_in                           :: no
S09 : diffracted beam, k_out                        :: no
```

```
S10 :                                                :: no
S11 :                                                :: no
S12 : direction of magnetization                     :: yes
S13 : Euler angles of k_in, k_out                    :: no
S14 : main axes of EFG                               :: no
S15 : direction of the magnetic hyperfine fields     :: yes
S16 :                                                :: no
S17 :                                                :: no
S18 : structure factor of the unit cell subgroups    :: no
S19 : Debye-Waller-factor of the electron shells     :: no
S20 : electronic scattering amplitude                :: no
S21 :                                                :: no
S22 : polarizationmatrices                           :: no
S23 :                                                :: no
S24 :                                                :: no
S25 : hyperfine interaction parameters               :: yes
S26 : Hamiltonian of the ground state                :: no
S27 : Hamiltonian of the excited state               :: no
S28 : energy eigenvalues                             :: no
S29 : eigenvectors of the ground state               :: no
S30 : eigenvectors of the excited state              :: no
S31 : strength of the transitions                    :: no
S32 : Moessbauer-Lamb-factor                         :: yes
S33 : index of refraction corrections                :: yes
S34 : precoefficients of the k-eigenvalue polynom    :: no
S35 :                                                :: no
S36 :                                                :: no
S37 :                                                :: no
S38 :                                                :: no
S39 :                                                :: no
S40 : transition energies                            :: yes
S41 : thickness of the crystal                       :: yes
S42 : coefficients of the k-eigenvalue polynom       :: no
S43 : k-eigenvalues                                  :: no
S44 :                                                :: no
```

```
S45 :                                                  :: no
S46 :                                                  :: no
S47 :                                                  :: no
S48 : reflectivities rsp. transmission                 :: yes
S49 :                                                  :: no
S50 :                                                  :: no
*
* the following integer values give boundaries for the indices
*  in some array printouts
*
N01 : begin of printout, concerning S32,S33  :: 1398
N02 : end ....                               :: 1398
*
N03 : begin of printout, concerning S34      :: 1398
N04 : end ....                               :: 1398
*
N05 :: 0
N06 :: 0
*
N07 : begin of printout, concerning S42,S43  :: 1398
N08 : end ....                               :: 1398
*
N09 : begin of printout, concerning S48      :: 1
N10 : end ....                               :: 1
*
*********************************************************************
*
* end of input file
```

B.3 in_kmix

```
*! Version 1.5
*
```

```
*******************************************************************************
*
* input and output files
* ======================
*
* the reflectivity data input files used by module KMIX
* are the reflectivity data output files created
* by module KREF
*
* name of the reflectivity data input file (RIF) or
* name of the file that contains a list of RIFs
*
* in case of a RIF name options may be specified :
*   fit    =>  use the angle/thickness scale of this file
*   delete =>  delete this file after use
*
  (1) input file, options :: data_trns_hFe  use
*
*
* the intensity data output file is used as
* input file for module KFIT
*
  (2) intensity data output file :: data_ints_hFe
*
*******************************************************************************
*
* module run mode
* ===============
*
*  use as first option :
*     e  for  energy representation
*     t  for  time representation
*
*  use as second option :
*     p  for  calculation of the phase of the scattered field
```

```
*     r  for  calculation of Faraday rotation
*     default is the calculation of the scattered intensity
*
  (3) mode :: time
*
* if you chose time representation (first option 't')
* you have to define the following two parameters..
*
  (4) FFT resolution [coarse/medium/fine] :: fine
*
  (5) separation of the SR pulses / ns    :: 153
*
*******************************************************************************
*
* thickness scale
* ===============
*
*  - thickness / micron   => thickness scale  1
*  - effective thickness  => thickness scale  2
*
  (6) use thickness scale :: 1
*
*******************************************************************************
*
* polarization properties of the incoming radiation
* ================================================
*
  (7)  degree of polarization / %  :: 90
*
* the type of polarization is given by the mixing angle :
*  linear pol. sigma   =>  mix.ang.    0 deg.
*  left circular       =>  mix.ang.  +90 deg.
*  right circular      =>  mix.ang.  -90 deg.
*
  (8)  mixing angle  / deg.  :: 0
```

```
*
* linear pol. sigma is defined in module KREF :
*  - in case of Bragg/Laue reflection it means
*    that the electric field of the radiation
*    is perpendicular to the scattering plane
*  - in case of forward scattering it means
*    that the electric field of the radiation
*    is perpendicular to the plane defined by
*    incident photon and external magnetic field
*
* this may be changed by the canting angle :
*  sigma perpend. to reference plane =>  cant.ang.   0 deg.
*  sigma parallel to reference plane =>  cant.ang.  90 deg.
*
  (9)  canting angle  / deg.  :: 80
*
*******************************************************************************
*
* polarization filter function of the detector
* ============================================
*
  (10) filter efficiency / %  :: 0
*
* the type of polarization that is
* filtered is given by the mixing angle.
*
* the polarization reference plane will be canted
* by the canting angle.
*
  (11) mixing  angle  / deg.  :: 0
  (12) canting angle  / deg.  :: 0
*
*******************************************************************************
*
* end of input file
```

B.4 in_kfit

```
*! Version 1.5
*
*****************************************************************************
*
* input and output files
* ======================
*
* the intensity data input files used by KFIT
* are the intensity data output files created
* by KMIX
*
* name of the intensity data input file (IIF) or
* name of the file that contains a list of IIFs
*
  (1) input file ::  data_ints_hFe
*
*
* name of experimental data input file
*
  (2) exp. data file  ::  hFe.exp 3column
*
*
* name of output data file for graphical representation
*
  (3) output data file  ::  data_graph
*
*****************************************************************************
*
* data window
* ===========
```

```
*
* fitting or representation of theory will be
* restricted to the given range ..
*
  (4) begin thickness range  :: -999
  (5) end ..                 ::  999
*
  (6) begin energy/time  range / gamma/ns   ::    5
  (7) end ..                                ::  140
*
*********************************************************************
*
* averaging
* =========
*
* for the weight function the
*  following selections are possible..
*  g       =  gaussian
*  l       =  lorentzian
*  r       =  rectangular
*  ag <R>  =  asymmetric gaussian with <R> giving the
*              ratio of left FWHM to right FWHM
*
  (8)  weight function for the thickness grid    :: g
  (9)  weight function for the time/energy grid  :: ag 0.3
*
*********************************************************************
*
* internal fit parameters
* =======================
*
* the following parameters are internal fit parameters
* tag the parameters you want to be fitted
* by a per cent sign '%' in col. 1
*
```

```
* if you don't tag any parameter and no external
* fit parameters are defined only the theory data
* will be forwarded to the output data set
* in this case the measured data is ignored
*
% (10) background                                 ::    6
% (11) scaling factor                            :: 3000
  (12) shift of the energy/time scale / gamma/ns  ::    1
  (13) thickness distribution FWHM                ::    0
% (14) energy/time resolution FWHM    / gamma/ns  ::    1
  (15) thickness                                  ::    8
*
*****************************************************************************
*
* creating thickness curves
* =========================
*
* thickness curves can be created instead of
*  the normal energy/time representation
* this is supported only if no fit parameters are selected
*
  (16) do you want to create thickness curves [y/n] :: no
  (17) thickness curve distance /  gamma/ns         :: 10
*
*****************************************************************************
*
* end of input file
```

Bibliography

[1] K. Shimizu, D. Takao, S. Furomoto, and K. Amaya. *Physica C*, 408–410:750–753, 2004.

[2] H. Cynn, J. E. Klepeis, C. S. Yoo, and D. A. Young. *Phys. Rev. Lett.*, 88(13):135701, 2002.

[3] H. K. Mao et al. *Science*, 292:914–916, 2001.

[4] W. J. Nellis, S. T. Weir, and A. C. Mitchell. *Shock Waves*, 9(5):301–305, 1999.

[5] R. L. Mössbauer. *Z. Physik*, 151:124, 1958.

[6] G. Steinle-Neumann, L. Stixrude, and R. E. Cohen. *P. Natl. Acad. Sci. USA*, 101(1):33–36, 2004.

[7] M. B. Stearns. *Phys. Rev. B*, 4(11):4081–4091, 1971.

[8] D. A. Shirley and G. A. Westenbarger. *Phys. Rev.*, 138(1A):A170–A176, 1965.

[9] A. L. Ruoff, H. Xia, and Q. Xia. *Rev. Sci. Instrum.*, 63(4342), 1992.

[10] H. K. Mao and P. M. Bell. *Carnegie Inst. Washington Yearbook*, 74:402, 1975.

[11] L. Merrill and W. A. Bassett. *Rev. Sci. Instrum.*, 45(2):290–294, 1974.

[12] D. J. Dunstan. *Rev. Sci. Instrum.*, 60(12):3789–3795, 1989.

[13] M. J. P. Brugmans and W. L. Vos. *J. Chem. Phys.*, 103(7):2661–2669, 1995.

[14] A. Jayaraman. *Rev. Mod. Phys.*, 55(1):65, 1983.

[15] R. A. Forman, G. J. Piermarini, J. D. Barnett, and S. Block. *Science*, 176:284, 1972.

[16] J. D. Barnett, S. Block, and G. J. Piermarini. *Rev. Sci. Instrum.*, 44(1):1–9, 1973.

[17] G. J. Piermarini, S. Block, J. D. Barnett, and R. A. Forman. *J. Appl. Phys.*, 46(6):2774–2780, 1975.

[18] D. L. Decker. *J. Appl. Phys.*, 36(1):157–161, 1965.

[19] D. L. Decker. *J. Appl. Phys.*, 37(13):5012–5014, 1966.

[20] H. K. Mao, P. M. Bell, J. W. Shaner, and D. J. Steinberg. *J. Appl. Phys.*, 49(6):3276–3283, 1978.

[21] J. M. Brown. *J. Appl. Phys.*, 86(10):5801–5808, 1999.

[22] G. L. Squires. *Introduction to the Theory of Thermal Neutron Scattering*. Cambridge University Press, 1978.

[23] W. L. Mao, H. K. Mao, C-S. Yan, J. Shu, J. Hu, and R. J. Hemley. *Appl. Phys. Lett.*, 83(25):5190, 2003.

[24] J. Xu and H. K. Mao. *Science*, 290:783, 2000.

[25] C. Seyfert, R.O Simmons, H. Sinn, D. A. Arms, and E. Burkel. *J. Phys. Cond. Mat.*, 11:3501–3511, 1999.

[26] G. Shen, M. L. Rivers, Y. Wang, and S. R. Sutton. *Rev. Sci. Instrum.*, 72(2):1273, 2001.

[27] G.V. Smirnov. *Hyperfine Interact.*, 123–124:31–77, 1999.

[28] W. Sturhahn. *Hyperfine Interact.*, 125:149–172, 2000.

[29] J.W. Lin. PhD thesis, California Institute of Technology, 2004.

[30] W. Sturhahn. *J. Phys. Cond. Mat.*, 16:S497–S530, 2004.

[31] B. Fultz, H. Kuwano, and H. Ouyang. *J. Appl. Phys.*, 77(7):3458–3466, 1995.

[32] B. Fultz, J. L. Robertson, T. A. Stephens, L. J. Nagel, and S. Spooner. *J. Appl. Phys.*, 79(11):8318–8322, 1996.

[33] J. S. Reid, R. A. Brain, and C. C. Ahn. In T.E. Wade, editor, *Proceedings of the 12th International VLSI Multilevel Interconnect Conference*, page 545, 1995.

[34] S. Veprek and S. Reiprich. *Thin Solid Films*, 268(1–2):64–71, 1995.

[35] J. A. Graetz. PhD thesis, California Institute of Technology, 2003.

[36] R. Birringer, H. Gleiter, H. P. Klein, and P. Marquadt. *Phys. Lett. A*, 102A(8):365–369, 1984.

[37] B. Fultz, L. Anthony, L. J. Nagel, R. M. Nicklow, and S. Spooner. *Phys. Rev. B*, 52(5):3315–3321, 1995.

[38] E. Bonetti, L. Pasquini, E. Sampaolesi, A. Deriu, and G. Cicognani. *J. Appl. Phys.*, 88(8):4571–4575, 2000.

[39] H. Frase, B. Fultz, and J. L. Robertson. *Phys. Rev. B*, 57(2):898–905, 1998.

[40] B. Fultz, C. C. Ahn, E. E. Alp, W. Sturhahn, and T. S. Toellner. *Phys. Rev. Lett.*, 79(5):937–940, 1997.

[41] L. Pasquini, A. Barla, A. I. Chumakov, O. Leupold, R. Ruffer, A. Deriu, and E. Bonetti. *Phys. Rev. B*, 66(7):073410, 2002.

[42] J. Trampenau, K. Bauszus, W. Petry, and U. Herr. *Nanostr. Mater.*, 6(5-8):551–554, 1995.

[43] G. Von Eynatten, J. Horst, K. Dransfeld, and H. E. Bömmel. *Hyperfine Interact.*, 29:1311, 1986.

[44] A. Kara and T. S. Rahman. *Phys. Rev. Lett.*, 81(7):1453–1456, 1998.

[45] D. Y. Sun, X. G. Gong, and X. Q. Wang. *Phys. Rev. B*, 63(19):193412, 2001.

[46] U. Stuhr, H. Wipf, K. H. Andersen, and H. Hahn. *Phys. Rev. Lett.*, 81(7):1449–1452, 1998.

[47] P. M. Derlet, R. Meyer, L. J. Lewis, Stuhr U., and H. Van Swygenhoven. *Phys. Rev. Lett.*, 87(20):205501, 2001.

[48] J. Chadwick. *J. Phys. A: Math. Gen.*, 32:4087–4095, 1999.

[49] R. Orbach. *Science*, 231:814–819, 1986.

[50] A. B. Papandrew, A. F. Yue, B. Fultz, I. Halevy, W. Sturhahn, T. S. Toellner, E. E. Alp, and H. K. Mao. *Phys. Rev. B*, 69:144301, 2004.

[51] T. S. Toellner. To be published.

[52] D. D. Ragan, D. R. Clarke, and D. Schiferl. *Rev. Sci. Instrum.*, 67(2):494–496, 1996.

[53] M.Y. Hu, W. Sturhahn, T.S. Toellner, P.M. Hession, J.P. Sutter, and E.E. Alp. *Nucl. Inst. Methods Phys. Res.*, 472:551–555, 1999.

[54] J. B. Hastings, D. P. Siddons, U. van Bürck, R. Hollatz, and U. Bergmann. *Phys. Rev. Lett.*, 66(6):770–773, 1991.

[55] R. Lübbers, G. Wortmann, and H. F. Grünsteudel. *Hyperfine Interact.*, 123–124(1):529–559, 1999.

[56] L. Van Hove. *Phys. Rev.*, 89(6):1189–1193, 1953.

[57] H.-E. Schaefer, R. Würschum, R. Birringer, and H. Gleiter. *Phys. Rev. B*, 38(14):9545–9554, 1988.

[58] R. Meyer, L. J. Lewis, S. Prakash, and P. Entel. *Phys. Rev. B*, 68:104303, 2003.

[59] P. M. Derlet and H. Van Swygenhoven. *Phys. Rev. Lett.*, 92(3):035505, 2004.

[60] P. M. Derlet, S. Van Petegem, and H. Van Swygenhoven. *Phys. Rev. B*, 71:024114, 2005.

[61] A. F. Yue, A. B. Papandrew, O. Delaire, B. Fultz, Z. Chowdhuri, R. Dimeo, and D. A. Neumann. *Phys. Rev. Lett.*, 93(20):205501, 2004.

[62] H. J. Fecht. *Nanostr. Mater.*, 6:33–42, 1995.

[63] A. Meyer, R. Dimeo, P. M. Gehring, and D. A. Neumann. *Rev. Sci. Instrum.*, 74(5):2759–2777, 2003.

[64] http://www.ncnr.nist.gov/dave/.

[65] P. D. Bogdanoff, B. Fultz, and S. Rosenkranz. *Phys. Rev. B*, 60:3976, 1999.

[66] J. Weissmüller, W. Krauss, T. Haubold, R. Birringer, and H. Gleiter. *Nanostr. Mater.*, 1:439–447, 1992.

[67] J. Weissmüller, R. D. Shull, G. Rixecker, R. D. McMichael, and L. H. Bennett. *Nanostr. Mater.*, 7(1):161–178, 1996.

[68] C-S. Zhang, B. Li, and P. R. Norton. *J. Nucl. Mater.*, 223:238–244, 1995.

[69] P. Hohenberg and W. Kohn. *Phys. Rev.*, 136(3B):B864, 1964.

[70] W. Kohn and L. J. Sham. *Phys. Rev.*, 140(4A):A1133, 1965.

[71] C. S. Wang, B. M. Klein, and H. Krakauer. *Phys. Rev. Lett.*, 54:1852, 1985.

[72] J. P. Perdew, S. Burke, and M. Ernzerhof. *Phys. Rev. Lett.*, 77:3865, 1996.

[73] J. Hafner. *Acta Mater.*, 48:71–92, 2000.

[74] J. P. Poirier. *Introduction to the Physics of the Earth's Interior*. Cambridge University Press, 2nd edition, 2000.

[75] C. Pisani, editor. *Quantum-Mechanical Ab-Initio Calculations of the Properties of Crystalline Materials*. Springer-Verlag, 1996.

[76] P. Mohn. *Hyperfine Interact.*, 128:67–78, 2000.

[77] S. Cottenier. *Density Functional Theory and the Family of (L)APW-methods: A Step-by-Step Introduction*. Institut voor Kern- en Stralingsfysica, K.U. Leuven, Belgium, 2002.

[78] D. Bancroft, E. L. Peterson, and S. Minshall. *J. Appl. Phys.*, 27(3):291–299, 1956.

[79] D. N. Pipkorn, C. K. Edge, P. Debrunner, G. De Pasquali, H. G. Drickamer, and H. Fraunfelder. *Phys. Rev.*, 135(6A):A1604–A1612, 1964.

[80] G. Cort, R. D. Taylor, and J. O. Willis. *J. Appl. Phys.*, 53(3):2064–2065, 1982.

[81] S. Nasu, T. Sasaki, T. Kawakami, T. Tsutsui, and S. Endo. *J. Phys. Cond. Mat.*, 14:11167–11171, 2002.

[82] S. C. Abrahams, L. Guttman, and J. S. Kasper. *Phys. Rev.*, 127:2052, 1962.

[83] H. Ohno and M. Mekata. *J. Phys. Soc. Jpn.*, 31(1):102–108, 1971.

[84] H. Ohno. *J. Phys. Soc. Jpn.*, 31(1):92–101, 1971.

[85] D. I. C. Pearson and J. M. Williams. *J. Phys. F Met. Phys.*, 9(9):1797–1813, 1979.

[86] E. P. Wohlfarth. *Phys. Lett. A*, 75A:141, 1979.

[87] K. Shimizu, T. Kimura, S. Furomoto, K. Takeda, K. Kontani, Y. Onuki, and K. Amaya. *Nature*, 412:316–318, 2001.

[88] S. S. Saxena and P. B. Littlewood. *Nature*, 412:290, 2001.

[89] C. Pfleiderer, M. Uhlarz, S. M. Hayden, R. Vollmer, H. V. Lohneysen, N. R. Bernhoeft, and G. G. Lonzarich. *Nature*, 412(6842):58–61, 2001.

[90] S. S. Saxena, P. Agarwal, K. Ahilan, F. M. Grosche, R. K. W. Haselwimmer, M. J. Steiner, E. Pugh, I. R. Walker, S. R. Julian, P. Monthoux, G. G. Lonzarich, A. Huxley, I. Sheikin, D. Braithwaite, and J. Flouquet. *Nature*, 406(6796):587–592, 2000.

[91] G. Steinle-Neumann, R. E. Cohen, and L. Stixrude. *J. Phys. Cond. Mat.*, 16:S1109–S1119, 2004.

[92] R. E. Cohen and S. Mukherjee. *Phys. Earth Planet. In.*, 143–144:445–453, 2004.

[93] M. B. Stearns. *Phys. Rev.*, 129:1136, 1962.

[94] I. Vincze and I. A. Campbell. *J. Phys. F Met. Phys.*, 3:647–663, 1973.

[95] B. Fultz and J.W. Morris Jr. *Phys. Rev. B*, 34(7):4480–4489, 1986.

[96] P. C. Riedi. *Physics Letters A*, 33(5):273–274, 1970.

[97] I. Vincze and G. Grüner. *Phys. Rev. Lett.*, 28:178, 1972.

[98] B. Fultz. PhD thesis, University of California, Berkeley, 1982.

[99] W. A. Harrison. *Electronic Structure and the Properties of Solids*. Dover, 1989.

[100] P. Blaha, K. Schwarz, G. K. H. Madsen, D. Kvasnicka, and J. Luitz. *WIEN2k, An Augmented Plane Wave + Local Orbitals Program for Calculating Crystal Properties*, 2001.

[101] http://www.bell-labs.com/project/PORT/.

[102] Y. Ma, M. Somayazulu, G. Shen, H. K. Mao, J. Shu, and R. J. Hemley. *Phys. Earth Planet. Inter.*, 143–144:455, 2004.

[103] E. Sterer, M. P. Pasternak, and R. D. Taylor. *Rev. Sci. Instrum.*, 61(3):1117–1119, 1990.

[104] N. M. Rosengaard and B. Johansson. *Phys. Rev. B*, 55:14975, 1997.

[105] L. Stixrude, R. E. Cohen, and D. J. Singh. *Phys. Rev. B*, 50(9):6442–6445, 1994.

[106] J. F. Janak. *Phys. Rev. B*, 16:255, 1977.

[107] H. Akai and T. Kotani. *Hyperfine Interact.*, 120–121:3–11, 1999.

[108] P. Novak and F. R. Wagner. *Phys. Rev. B*, 66:184434, 2002.

[109] P. Novak, J. Kunes, W. E. Pickett, W. Ku, and F. R. Wagner. *Phys. Rev. B*, 67:140403R, 2003.

[110] I.I. Mazin, D.A. Papaconstantopoulos, and M.J. Mehl. *Phys. Rev. B*, 65:100511R, 2002.

[111] R. Moessner and J. T. Chalker. *Phys. Rev. Lett.*, 80:2929, 1998.

[112] S. R. Dunsiger, J. S. Gardner, J. A. Chakhalian, A. L. Cornelius, M. Jaime, R. F. Kiefl, R. Movshovich, W. A. MacFarlane, R. I. Miller, J. E. Sonier, and B. D. Gaulin. *Phys. Rev. Lett.*, 85:3504, 2000.

[113] S. Siegel. *Phys. Rev.*, 57:537–545, 1940.

[114] B. Fultz, T. A. Stephens, E. E. Alp, M. Y. Hu, T. S. Toellner, and W. Sturhahn. *Phys. Rev. B*, 61:14517, 2000.

[115] S. Merkel, A. F. Goncharov, H. K. Mao, P. Gillet, and R. J. Hemley. *Science*, 288:1626–1629, 2000.

[116] V. Thakor, J. Staunton, J. Poulter, S. Ostanin, B. Ginatempo, and E. Bruno. *Phys. Rev. B*, 67:180405R, 2003.

[117] J.-P. Rueff, M. Krisch, Y. Q. Cai, A. Kaprolat, M. Hanfland, M. Lorenzen, C. Masciovecchio, R. Verbeni, and F. Sette. *Phys. Rev. B*, 60:14510, 1999.

[118] J.-P. Rueff and C.-C. Kao. *Phys. Rev. Lett.*, 82:3284, 1999.

[119] J. Badro, V. V. Struzkhin, J. Shu, R. J. Hemley, and H. K. Mao. *Phys. Rev. Lett.*, 83:4101, 1999.

[120] A. Zunger, S. H. Wei, L. G. Ferreira, and J. E. Bernard. *Phys. Rev. Lett.*, 65:353, 1990.

[121] C. Jiang, C. Wolverton, J. Sofo, L.-Q. Chen, and Z.-K. Liu. *Phys. Rev. B*, 69:214202, 2004.

[122] A. Van de Walle, M. Asta, and G. Ceder. *Calphad*, 26(4):539, 2002.

[123] C. G. Shull and M. K. Wilkinson. *Phys. Rev.*, 97:304, 1955.